QUANTITATIVE MODELS OF THE MAGNETOSPHERIC MAGNETIC FIELD: METHODS AND RESULTS

A Review

NIKOLAI A. TSYGANENKO

Institute of Physics, Leningrad State University, Stary Petergof 198904, Leningrad, U.S.S.R.

(Received 20 February, 1989)

Abstract. The paper reviews various approaches to the problem of evaluation and numerical representation of the magnetic field distributions produced within the magnetosphere by the main electric current systems including internal Earth's sources, the magnetopause surface current, the tail plasma sheet, the large-scale systems of Birkeland current, the currents due to radiation belt particles, and the partial ring current circuit. Some basic physical principles as well as mathematical background for development of magnetospheric magnetic field models are discussed.

A special emphasis is placed on empirical modeling based on datasets created from large bodies of spacecraft measurements. A review of model results on the average magnetospheric configurations and their dependence on the geomagnetic disturbance level and the state of interplanetary medium is given. Possibilities and perspectives for elaborating the 'instantaneous' models capable of evaluating a current distribution of magnetic field and force line configuration based on a synoptic monitoring the intensity of the main magnetospheric electric current systems are also discussed. Some areas of practical use of magnetospheric models are reviewed in short. Magnetospheric plasma and energetic particle measurements are considered in the context of their use as an independent tool for testing and correcting the magnetic field models.

Table of Contents

Space Science Reviews **54:** 75–186, 1990.

1. Introduction

Distribution of the magnetic field in the near-Earth space as well as its temporal variations should be considered as one of the most important characteristics of our environment. Although this idea has been properly realized only during recent decades, the quantitative modeling of the geomagnetic field belongs, in fact, to probably the oldest branch of the geophysical research. The first advance in this area was made still in the last century by the pioneering investigations of Gauss (1839), who developed mathematical foundations for analytical representation of the main geomagnetic field and obtained numerical values of the coefficients using the data from the first ground-based network of observatories.

There exist a conventional classification of models into two groups which are the descriptive (or empirical) models and the physical ones (e.g., Stern, 1987b). The descriptive models are based on sufficiently large amounts of observational data and provide empirical analytic formulae, tables, and/or numerical algorithms which enable a user to compute the field components at any point within the modeling region. In the physical models the magnetic field distribution is found from the solutions of MHD or kinetic equations formulated within a framework of some theoretical hypotheses and simplifying assumptions. The experimental data are employed here to a more limited extent, mainly for imposing proper boundary and/or initial conditions. Both approaches have their own advantages and shortcomings. Empirical models by themselves cannot yield a comprehensive understanding of physical processes involved in formation or maintenance of the observed magnetic field structures. However, they are based on measurements and thus provide the best agreement with the real average configurations. Physical models are absolutely indispensable for clarifying the essence of phenomena; they relate the observed evolutions in the magnetic field structure to the plasma dynamics and sometimes can at least qualitatively predict the observed features. However, at the present time they are still far from being adequate for practical purposes.

With the beginning of space exploration it became necessary to develop the quantitative models valid up to large geocentric distances of the order of tens of Earth radii. In these remote regions a significant or even prevailing contribution to the magnetic field comes from the extraterrestrial current systems including the magnetopause currents as well as the distributed currents carried by the magnetospheric plasma particles. Modeling the magnetic field in this region runs into a number of serious problems. Since a significant part of the magnetosphere is not current-free, it is no longer possible to apply the scalar potential method in which it is enough to use the magnetic field data taken only near the boundary surfaces. Rather, the vector measurements have to be done throughout the whole modeling region, and the task becomes even more complex due to the extreme variability of the magnetospheric configuration which exhibits diurnal and

seasonal variations caused by the geodipole wobbling as well as irregular fluctuations arising from substorms and other solar-wind-related phenomena. Additional slow changes are associated with a long-term variations in the parameters of the interplanetary medium caused by the 11-year solar cycle periodicity. A large variety of different geophysical situations arising from a very complex dependence of the magnetospheric state on the external factors leads to a considerable scatter in the observed field magnitude. It means that purely empirical approach requires sufficiently large databases. Partly for that reason, major surveys in sixties were directed towards development of more or less sophisticated physical models (Akasofu and Chapman, 1961; Mead and Beard, 1964; see also a review by Roederer, 1969).

In the later period large amounts of data from a number of spacecraft magnetic field experiments were accumulated. This enabled Mead and Fairfield (1975) to develop the first empirical magnetospheric model from which the average magnetic field line configurations were obtained and the main changes in their structure accompanying the increase of the disturbance level were revealed. During the last decade more elaborate models of this kind were designed based on larger experimental datasets and a more accurate approach to the magnetic field description, with a separate representation of contributions coming from different electric current systems (Tsyganenko and Usmanov, 1982; Tsyganenko, 1987a, 1989a).

In this review an attempt to give a comparative analysis of existing methods and results of the quantitative representation of the magnetospheric magnetic field is done. It should be noted here that of a number of works devoted to this problem as yet only a few models are brought to a level of really practical ones which take into account all the main field sources, are based on sufficient amounts of data, and provide in an available format the necessary expansions, coefficients and/or numerical codes. The most papers on models consider, in fact, the effects from separate current systems. For this reason, a considerable part of the present review deals just with methods of modeling, rather than with a detailed comparison of the field line pictures given by different authors.

The presentation is organized as follows. In Section 2.1 the modeling of the internal source contribution to the magnetospheric field is considered briefly. Section 2.2 covers in more detail the existing approaches to the quantitative treatment of the magnetopause current effects. Section 2.3 is devoted to the intramagnetospheric sources including the magnetotail current sheet, Birkeland current systems, the ring current and the partial ring current. As a matter of fact, the rigorous division of the magnetospheric field sources into the different types is hardly possible. Actually they constitute a unified interconnected system. The central tail plasma sheet current closes via the return circuit lying on the magnetopause and thus superposes with Chapman–Ferraro currents, while in the near nightside region it merges continuously into the ring current. On the other hand, in many models a unified representation of different sources is employed by using for them the same mathematical expressions. This brings some additional complications in the presentation of material, so that the assumed division into topics is somewhere rather arbitrary.

Section 3 deals with the analysis of the magnetic field and electric current structures obtained in the recent versions of empirical models. In particular, Section 3.1 describes the results of calculations pertaining to the model magnetospheric configurations in dependence on the level of geomagnetic disturbance and the geodipole axis orientation, and presents a comparison of the model magnetic field distributions with those obtained from independent spacecraft measurements. In Section 3.2 some effects of the interplanetary medium discerned in empirical models as well as their interpretation in terms of the magnetohydrostatic treatment are considered. In Section 3.3 and 3.4 a discussion of diurnal and seasonal variations in the location of conjugate points and polar cusps is presented.

Measurements of the charged particle fluxes can serve as an abundant source of additional information on the structure of the magnetosphere. These data can be employed as a testing tool for controlling the adequacy of the magnetic field models: on the other hand, as shown in Section 4, there exist promising possibilities for using the measurements of energetic particle fluxes at low-altitude polar-orbiting satellites for a synoptic correction of the average field models and real-time monitoring of the current field line configuration in the near nightside magnetosphere.

The following material was selected with understanding that the problem of the magnetospheric field modeling roots not only in physics, but also has a complicated computational aspect. By this reason I did not care too much to save the page space at the expense of formulae, and the questions 'How to calculate?' were paid by no less attention than the ones 'How to explain?'. For the same reason it was considered appropriate to supply the paper by Appendix containing a short description of methods for calculating the parameters of model magnetospheres based on spacecraft datasets.

A particular emphasis, in relation to the author's own works in this area, is made on the descriptive models. The magnetohydrostatic approach is considered in a comparatively lesser detail; the corresponding studies are discussed mainly in the context of the empirical modeling results. Interested readers may refer to the recent reviews by Voigt (1986) and Schindler and Birn (1986) for more comprehensive presentation and more exhaustive references. Beside the static models, these reviews consider also non-stationary phenomena restricted to slow quasistatic processes which can be addressed in the framework of an adiabatic treatment. Faster changes of the magnetic field and plasma configurations characteristic of the substorm explosive phase constitute a next wide class of problems reviewed recently in several papers (e.g., Pellinen and Heikkila, 1984; Pudovkin and Semenov, 1985).

Outside the scope of the present work remains also a series of papers on the numerical MHD modeling of the magnetosphere (e.g., Ogino *et al.*, 1986). This approach rapidly develops now and has the most promising future perspective.

2. The Sources of the Magnetospheric Magnetic Field and Methods for Quantitative Modeling Their Contributions

The net magnetic field in the magnetosphere is a sum of two terms

$$\mathbf{B} = \mathbf{B}_I + \mathbf{B}_E , \tag{1}$$

where $\mathbf{B}_I$ and $\mathbf{B}_E$ are the fields produced by the intra- and extra-terrestrial electric current systems, respectively. The latter term $\mathbf{B}_E$ receives contributions from (i) the Chapman–Ferraro surface current flowing at the magnetopause, (ii) the magnetotail current system, (iii) the ring current, (iv) the field-aligned currents, and (v) the ionospheric currents. At the Earth's surface and at ionospheric heights the magnitude of the second term $\mathbf{B}_E$ in (1) is small in comparison with $\mathbf{B}_I$: even during a strong disturbance $\mathbf{B}_E$ does not exceed a few percent of $\mathbf{B}_I$. In quiet conditions a significant contribution to $\mathbf{B}_E$ comes in this region from ionospheric sources. At higher latitudes the field-aligned currents are also of importance due to convergence of the current streamlines towards the Earth. The net magnetic effect of the ionospheric and Birkeland current in the high-latitude regions varies usually from tens to hundreds of nanotesla and can rise above a thousand nanotesla during magnetospheric disturbances. Nevertheless, at small geocentric distances the geomagnetic force line configuration is governed by the internal field $\mathbf{B}_I$ which is tied to the rotating Earth and can be represented in the geographic or the dipole geomagnetic coordinate systems by the well-known expansions of the scalar potential in spherical harmonics.

On moving away from the Earth's surface the internal field rapidly decreases as K^{-3}, so that at $R \sim 8$–$10\ R_E$ the terms $\mathbf{B}_I$ and $\mathbf{B}_E$ become of the same order of magnitude, while at still larger distances the external field dominates. At the same time, the relative amplitude of the magnetic field fluctuations grows up considerably, since the sources of the external field $\mathbf{B}_E$ are closely related to highly variable solar wind state both by means of the 'directly-driven' mechanisms (Akasofu, 1981) and through the 'storage-release' process (e.g., Baker *et al.*, 1985). From this stems one of the main difficulties in the empirical modeling of the magnetosphere. The experimental datasets used for determination of the model parameters contain a relatively intense 'noise', which imposes severe limitations on the amount and quality of the available information. The largest amplitudes of the irregular variations related to disturbances are observed in the near low-latitude nightside magnetosphere in the vicinity of the inner tail current sheet and the outer ring current region. The magnitudes of the current density can change here by more than an order of magnitude and the corresponding excursions of the magnetic field vector may exceed a hundred nanotesla. In the magnetotail lobes the relative magnetic field changes are not so dramatic: at $X_{\mathrm{GSM}} \lesssim -10\ R_E$ the total B can rise typically twice as large as its average value, in response to enhanced solar wind pressure and/or accumulation of the tail-lobe magnetic flux due to effects of southward IMF. At the dayside the overall magnetic field distribution depends mainly on the solar wind ram pressure which defines the magnitude of the magnetopause current; in quiet conditions its contribution to $\mathbf{B}_E$ is on the order of the first tens of nanotesla. Typical variations

of the dayside magnetic field caused by fluctuations in the solar wind dynamical pressure can be as large as several tens of nanotesla and only very rarely they exceed a hundred nanotesla.

The present paper deals mainly with the models of the magnetic field from external sources. We begin, however, with a short survey of the internal field modeling and some considerations relevant to its use in the magnetospheric research

2.1. Magnetic field from internal sources

Sources of the main geomagnetic field lie inside the Earth, so that the field $\mathbf{B}_I$ is curl-free at $R > 1\ R_E$ and can thus be represented as

$$\mathbf{B} = -\nabla V. \tag{2}$$

Since the magnetic field is divergenceless, this leads to Laplace's equation for the potential V and hence to the possibility of expanding it in the spherical harmonic series

$$V(R, \theta, \lambda) = R_E \sum_{n=1}^{\infty} (R_E/R)^{n+1} \sum_{m=0}^{n} (g_n^m \cos m\lambda + h_n^m \sin m\lambda) P_n^m (\cos\theta), \tag{3}$$

where $R_E = 6371.2$ km is the average Earth's radius, spherical coordinates (R, θ, λ) usually refer to the geographical system and P_n^m are the associated Schmidt-normalized Legendre functions (e.g., Cain *et al.*, 1967). From Equations (2) and (3) the magnetic field components read

$$\begin{aligned}
B_R &= \sum_{n=1}^{N} (n+1)(R_E/R)^{n+2} \sum_{m=0}^{n} (g_n^m \cos m\lambda + h_n^m \sin m\lambda) P_n^m (\cos\theta), \\
B_\theta &= -\sum_{n=1}^{N} (R_E/R)^{n+2} \sum_{m=0}^{n} (g_n^m \cos m\lambda + h_n^m \sin m\lambda) \partial P_n^m/\partial\theta, \\
B_\lambda &= (\sin\theta)^{-1} \sum_{n=1}^{N} (R_E/R)^{n+2} \sum_{m=0}^{n} (g_n^m \sin m\lambda - h_n^m \cos m\lambda) P_n^m (\cos\theta).
\end{aligned} \tag{4}$$

The coefficients g_n^m and h_n^m for a given epoch are determined by a least-squares fitting of the model to the databases obtained from the ground, marine, air, and satellite measurements. Including the experimental material for different years makes it possible to evaluate the secular changes of coefficients. At present it is assumed (Peddie, 1982; Barraclough, 1987) that the main geomagnetic field for the interval 1945–1985 to be computed from (4) using the appropriate epoch models, with linear interpolation of the coefficients for the intervening dates. The models for the past epochs including 1980.0 constitute the Definitive Models (DGRF), while the 1985.0 coefficients together with a forecast model of the secular variation between 1985.0 and 1990.0 is defined as a Provisional Reference Model (PGRF), so that for the last period

$$\begin{aligned}
g_n^m(t) &= g_n^m(t_0) + \dot{g}_n^m (t - t_0), \\
h_n^m(t) &= h_n^m(t_0) + \dot{h}_n^m (t - t_0),
\end{aligned} \tag{5}$$

where t_0 = 1985.0. The tables of DGRF and PGRF coefficients are given by Barraclough (1987) (see also IAGA News No. 26, December 1987) for N = 10.

Due to the rapid decrease of the relative magnitude of higher-order terms in (3) and (4) with altitude, a considerable saving of computer time can be obtained by a proper choice of the maximal order of spherical harmonics N in (4) for a given radial distance R. For example, at the spherical surface with $R = 3\,R_E$ the maximal deviation of the vector $\mathbf{B}_I^{(6)}$ (computed from (4) with N = 6) from its 'precise' value $\mathbf{B}_I^{(10)}$ (i.e., obtained by using the full set of available model coefficients) does not exceed $\Delta B^{(6)} \sim 0.1$ nT. In most applications there is no reason in setting the permissible error value to be less than a few tenths (or even units) of nanotesla. Based on the maximal error values, one can estimate the necessary length N of the expansions (4) as function of the geocentric distance. Figure 1 shows the corresponding plots of N against R for four values of ΔB. If one assumes ΔB = 1 nT, then a simple estimate holds for N as

$$N = [1 + 9/R]\,, \tag{6}$$

where the square brackets denote the maximal integer of the quantity inside.

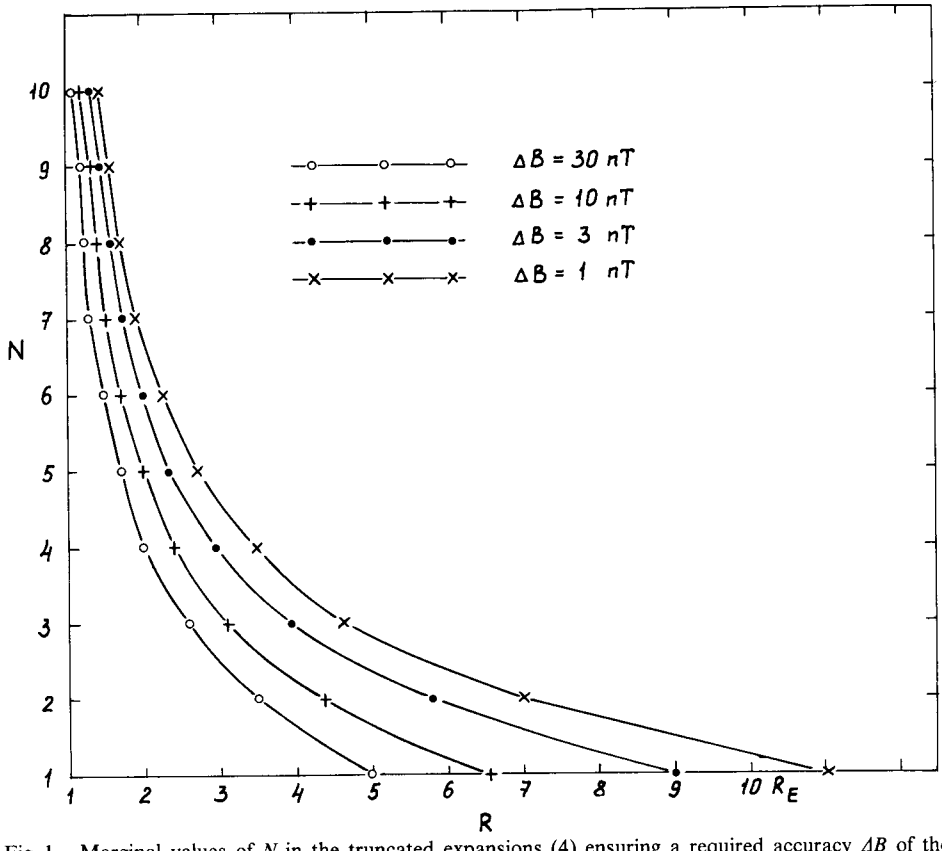

Fig. 1. Marginal values of N in the truncated expansions (4) ensuring a required accuracy ΔB of the computed internal field vector, plotted against the geocentric distance R for four values of ΔB.

In some practical problems including the field line tracing from the Earth's surface into the magnetosphere or in the opposite direction one can use the corrected geomagnetic coordinates of the ground points (Hakura, 1965; Gustafsson, 1970; Tsyganenko, 1979; Allen *et al.*, 1982) instead of the dipolar geomagnetic ones. A principal simplification introduced by this substitution consists in that a purely dipolar approximation with $N = 1$ in (4) can be employed in this case for the main geomagnetic field instead of using the full expansions with the non-dipolar terms. This question, however, should be considered in a bit more detail. The corrected geomagnetic coordinates are known to account for the influence of the higher-order terms in (4) upon the location of footpoints of the magnetic field lines coming from given points of the dipolar equatorial plane. The corresponding calculations in the above-cited works did not take into account the extraterrestrial field sources. Since the relative position of the internal and external current systems depends on universal time and season, it is clear that including the term $\mathbf{B}_E$ will result in diurnal and seasonal variations of the corrected coordinate values. It seems intuitively that the variations should be rather small because the influence of the non-dipolar harmonics is significant only at relatively low altitudes, where the internal field is much larger than the external one. It can thus be supposed that the main contribution to the expected diurnal/seasonal variations of the corrected coordinates comes from those external current systems which provide the largest disturbances within the 'sphere of influence' of the higher-order terms in $\mathbf{B}_I$. Evidently, among the main extraterrestrial magnetic field sources Birkeland current systems meet this criterion to the most extent.

A quantitative investigation of this equation was first carried out by Izhovkina (1979) who used the POGO (8/71) internal field model (Langel, 1974) together with the Olson and Pfitzer (1974) and Mead and Fairfield (1975) models for the external field. A general result was that taking into account the external sources leads to only an insignificant variation in the corrected coordinate values, so that the corresponding shifts of the field line footpoints do not exceed a few tens of kilometres. However, the external field models used in that study do not incorporate properly the contribution from the field-aligned currents. This motivated us to do a more comprehensive analysis using an explicit model for the magnetic field of Birkeland current system (Tsyganenko, 1988). An outline of the model will be given later on (Subsection 2.3.2, Figures 25–27). Net currents in the large-scale circuits I and II (Iijima and Potemra, 1976) were specified so that the transverse disturbance $\Delta B_\perp$ at ionospheric level calculated from the model in the polar cap region and at auroral latitudes (between the upward and downward current sheets) be about ~ 300 nT and ~ 600 nT, respectively. The corrected geomagnetic coordinates were computed by means of a straightforward procedure (e.g., Sergeev and Tsyganenko, 1980). Namely, a field line was traced from a given point (θ, λ) of the Earth's surface, taking into account both the higher-order terms in the internal field expansion (4) and the external field $\mathbf{B}_E$ including the contribution from Birkeland currents. The tracing was terminated either on intercepting the sphere with $R = 10\, R_E$, where the relative contribution from the higher-order harmonics is negligibly small, or on reaching the farthermost point of the field line (in case of a low-latitude footpoints).

After that the reverse tracing was done from the termination point, with the only difference in that $N = 1$ was taken now in (4), i.e., all the higher-order terms were excluded from the internal field. The geomagnetic coordinates of the 'landing point' (θ_c, λ_c) were taken, by definition, as the corrected ones for the initial point (θ, λ).

The computations showed that in all cases considered the external sources including Birkeland currents do not exert any significant influence on the values of the corrected geomagnetic coordinates. The largest changes due to 'switching on' the external current systems, as anticipated, are observed at auroral latitudes. However, even in this region the differences do not exceed $0.3° - 0.4°$ of latitude, in case of the most disturbed version of the external field model. At other latitudes typical variations of the corrected coordinates are on the order of $0.1°$ or less.

2.2. Contribition from the magnetopause currents

The magnetopause itself is a relatively thin current sheet separating the well-ordered magnetic field of terrestrial origin from the magnetosheath region containing a disturbed magnetized stream of the solar wind. The current flowing within the magnetopause layer sustains local and global balance between the net external pressure of the magnetosheath plasma and the electrodynamical stresses which can be represented equivalently in terms of the interior magnetic pressure. On the other hand, the magnetopause currents ensure the almost complete confinement of the net intramagnetospheric field within the cavity.

One of the first attempts to develop a physical concept of the fundamental mechanisms of the interaction of the solar plasma with the geomagnetic field was done by Chapman and Ferraro (1931). Long before the discovery of the solar wind they were able to envisage the main effects of the interplanetary plasma impinging on the boundary of the geomagnetic field and to estimate quantitatively the distortion of the initially dipolar vacuum configuration. Later on their approach was developed in a number of works based on a numerical treatment of the pressure balance equation (Beard and Jenkins, 1962; Midgley and Davis, 1962, 1963; Mead and Beard, 1964; Mead, 1964; Midgley, 1964; Olson, 1969; Choe *et al.*, 1973; Choe and Beard, 1974; Halderson *et al.*, 1975). Many of these works had been discussed in literature during the past decades (e.g., Akasofu and Chapman, 1972; Isaev and Pudovkin, 1972; Sergeev and Tsyganenko, 1980); for this reason only a brief outline of this first method will be given below.

One of results of those studies is the fact that the shape of the self-consistent model magnetopause does not depend significantly on the dynamical pressure of the solar wind; the only parameter incorporating this dependence in a very simple form is the characteristic scale distance from the geodipole to the subsolar point. On the other hand, a considerable body of experimental evidence on the magnetopause location has been obtained since the beginning of the space age. These studies provided a foundation for the development of an alternative approach in which the magnetospheric boundary is considered as a surface of a given shape specified by means of an appropriate function incorporating a parametric dependence on the solar wind pressure. The magnetic field from the boundary currents is computed from the condition of complete or partial shielding of the contribution of the intramagnetospheric sources outside the cavity.

Models of this kind were developed in the works by Alekseev ans Shabansky (1972), Alekseev (1978), Voigt (1972, 1981), Tsyganenko (1976, 1981, 1989c), Stern (1985), Schulz and McNab (1987). We shall consider them in more detail in Subsection 2.2.2.

Along with these approaches, there exists a third one based on a formal adjustment of appropriate fictitious magnetic field sources or fitting relatively simple analytic expressions which yield a reasonable distribution of the magnetic field within the modeling region. These are the image dipole models (Taylor and Hones, 1965; Antonova
and Shabansky, 1968; Willis and Pratt, 1972). In fact, the model of Mead and Fairfield (1975) as well as the expansions representing the boundary current contribution in the models of Tsyganenko and Usmanov (1982) and Tsyganenko (1987, 1989a) should also be referred to this type. Strictly speaking, this approach is relevant mostly to the problem of quantitative approximation of a model field and is capable of providing reasonable results only on a basis of fitting the formal parameters to the experimental data. The image source models, as a rule, yield satisfactory results only within a rather limited region. Another serious shortcoming is their inability to simulate properly the geodipole tilt effects. At the present time the models of that kind are only rarely used for practical purposes.

2.2.1. *Models with a Self-Consistent Magnetopause*

Models of this type are based on a solution of the problem of calculating the shape of the boundary between a non-magnetized stream of non-interacting particles and a confined vacuum magnetic field configuration containing a dipole source at the origin, first obtained in a direct way by Mead and Beard (1964). They supposed that at any point of the boundary (Figure 2) a local balance is maintained between the dynamical ram pressure of the stream and the magnetic pressure inside the cavity. Assuming a specular reflection of particles at the boundary

$$2\pi m v^2 \cos^2 \chi = (\mathbf{B} \cdot \mathbf{B})/8\pi , \tag{7}$$

where χ is the angle between the stream direction and the local normal $\mathbf{e}_n$. The net magnetic $\mathbf{B}$ at a point closely adjacent to the boundary on the inside can be expanded as

$$\mathbf{B} = B_d + \mathbf{B}_{CF} = \mathbf{B}_d + \mathbf{B}_p + \mathbf{B}_c , \tag{8}$$

where $\mathbf{B}_d$ is the geodipole contribution and the sum $\mathbf{B}_p + \mathbf{B}_c = \mathbf{B}_{CF}$ represents the field of the magnetopause currents. The reason for dividing $\mathbf{B}_{CF}$ into two terms is that its main part $\mathbf{B}_p$ corresponding to the contribution from the nearest adjacent area of the boundary can be easily evaluated as

$$\mathbf{B}_p = (2\pi/c)\mathbf{J} \times \mathbf{e}_n , \tag{9}$$

where $\mathbf{J}$ denotes the local surface current density. The small correction term $\mathbf{B}_c$ in (8) arises due to inhomogeneities of the current density and the surface curvature effect. Since on traversing the infinitely thin boundary the term $\mathbf{B}_p$ merely changes its sign, $\mathbf{B}_d$

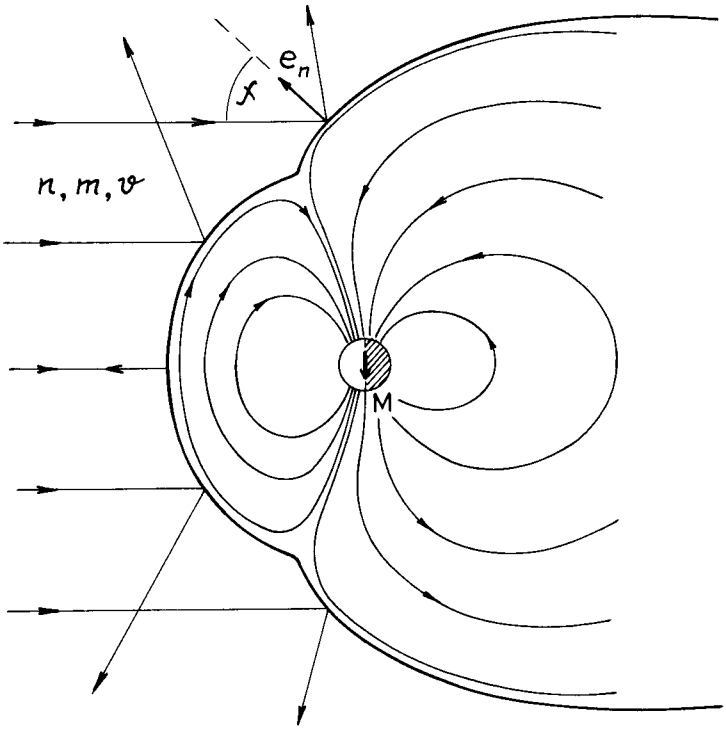

Fig. 2. Schematic illustration of the self-consistent magnetopause problem in the approach of Mead and Beard (1964).

and $\mathbf{B}_c$ remain by the same values, and the total field $\mathbf{B}$ falls to zero, we have

$$\mathbf{B}_p = \mathbf{B}_d + \mathbf{B}_c , \tag{10}$$

which being substituted in (8) yields

$$\mathbf{B} = 2(\mathbf{B}_d + \mathbf{B}_c) . \tag{11}$$

Neglecting the correction term $\mathbf{B}_c$ it possible to find from (7) and (11) a first-approximation boundary surface with the subsolar point located at distance $R_0 = (M_E^2/4\pi nmv^2)^{1/6}$ from the dipole. This enables evaluation of the term $\mathbf{B}_c$ by integrating over the newly determined surface with the current density $\mathbf{J}$ obtained from (9) and (10) and setting $\mathbf{B}_c = 0$ in the integrand as

$$\mathbf{B}_c = \frac{1}{2\pi} \int_{S-\Delta S} \frac{[\mathbf{e}_n \times (\mathbf{B}_d + \mathbf{B}_c)] \times (\mathbf{R} - \mathbf{R}')}{|\mathbf{R} - \mathbf{R}'|^3} \, dS' , \tag{12}$$

where a small area ΔS containing the singular point $\mathbf{R}' = \mathbf{R}$ is excluded from the integration surface. Using the computed $\mathbf{B}_c$ distribution, the procedure of constructing the surface and calculating $\mathbf{B}_c$ from (12) is repeated in the next approximation. The

iterations converge very rapidly and 4–5 cycles are enough for reaching the self-consistent solution.

The next problem is to develop a relatively simple analytical or numerical representation of $\mathbf{B}_{CF}$ distribution which would be accurate enough and suitable for practical purposes. Since the field $\mathbf{B}_{CF}$ is curl-free, one of possibilities is to represent it as $\mathbf{B}_{CF} = -\nabla \mathbf{U}_{CF}$, where the potential $\mathbf{U}_{CF}$ can be approximated by a finite sum containing spherical harmonic terms with positive powers of the radius R (Mead, 1964; Midgley, 1964)

$$U_{CF}(R, \theta, \varphi) = R_0^{-2} \sum_{n=1}^{N} (R/R_0)^n \sum_{m=0}^{n} G_{nm} P_n^m (\cos\theta) \cos m\varphi , \tag{13}$$

where (R, θ, φ) are the spherical solar-magnetic coordinates of the observation point and R_0 is the first approximation subsolar point distance (in the paper by Mead (1964) it was replaced by the self-consistent distance $R_b = 1.068\ R_0$). Later on this approach was extended by Olson (1969) to a more general case of a tilted geodipole.

The most advanced elaboration of this method was carried out in the works by Choe *et al.* (1973), Choe and Beard (1974), Halderson *et al.* (1975), and Beard *et al.* (1982) which are considered below in a little more detail. Choe *et al.* (1973) made a revision of the results of Mead and Beard (1964) for the case of perpendicular geodipole ($\psi = 0$) and performed the calculation of the magnetopause shape for several non-zero tilt angles as well. The revision was necessary because a significant part of the surface had been found by Mead and Beard only by means of an interpolation. Besides that, as seen from Equation (12), they circumvented the difficulty with the singular point simply by excluding its vicinity from the integration, which also could lead to a certain error. Instead of Equation (12) Choe *et al.* (1974) and Beard (1982) solved the equivalent one

$$\mathbf{B}_{CF} = \frac{1}{4\pi} \int_S \frac{[\mathbf{e}_n \times (\mathbf{B}_d + \mathbf{B}_{CF})] \times (\mathbf{R} - \mathbf{R}')}{|\mathbf{R} - \mathbf{R}'|^3} \, dS' , \tag{14}$$

where the integration is performed over the whole surface; to avoid the troubles with the singularity, an analytic representation of the integrand in a form of an expansion in powers of $(\mathbf{R} - \mathbf{R}')$ was applied.

The obtained distributions of the boundary field inside the cavity were used for determination of the coefficients of the spherical harmonic expansions (13) which were represented as cubic polynomials of the geodipole tilt angle

$$G_{nm}(\psi) = \sum_{i=0}^{3} a_i \psi^i .$$

Figure 3 shows a configuration of the magnetic field lines in the noon–midnight meridian plane plotted for a corrected version of this model described by Halderson *et al.* (1975). The picture corresponds to a nearly maximal value of the geodipole tilt angle $\psi = 30°$. The spherical harmonic expansions (13) provide a satisfactory representation of the boundary field in the near magnetosphere. In particular, even for large ψ

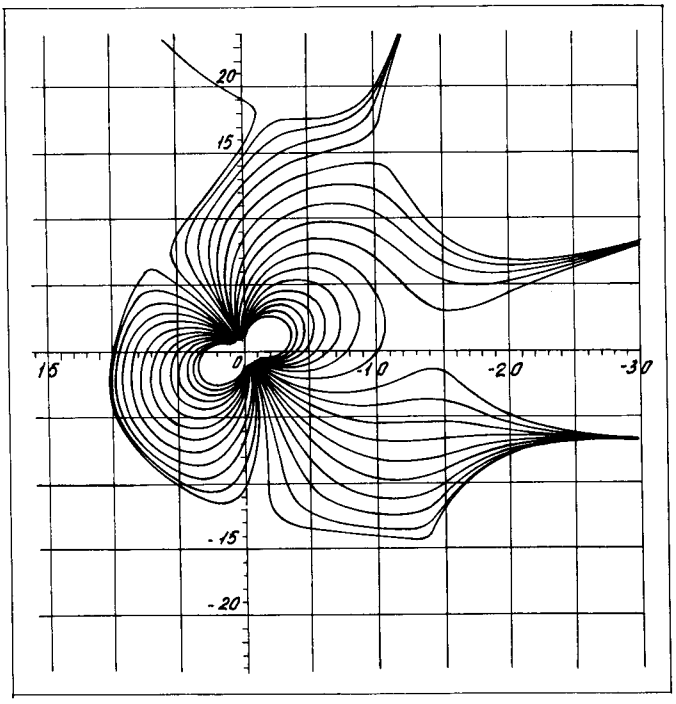

Fig. 3. Magnetic field configuration in the noon–mignight meridian plotted by using the model of Halderson *et al.* (1975) for tilted geodipole. The observed convergence of the field lines into bundles beyond $\sim 15\, R_E$ is a model artefact related to rapid divergence of the spherical harmonic expansion (13) at $R > R_0$.

the field lines threading the polar cusp regions show a rather good fit to the shape of the model magnetopause. However, at larger distances ($R > R_0$) the expansions diverge and, as seen in Figure 3, the field lines exhibit an unrealistic behaviour, so that a different representation is necessary in that region.

Beard *et al.* (1982) recalculated the coefficients of Halderson *et al.* (1975) using an improved treatment of the singular point in the Biot–Savart integral (14). Two alternative methods for representation of the field $\mathbf{B}_{CF}$ in the tail region ($R > R_0$) were also proposed in that work. The first one is based on expanding the potential U_{CF} in a series of cylindrical harmonics

$$U_{CF} = \sum_{m,i} A_{m,i} J_m(K_i \rho) \sin m\alpha\, e^{K_i z}, \tag{15}$$

where the variable z corresponds to the x_{GSM} coordinate, ρ is the distance from the Sun–Earth axis, and α is the angle measured from the equatorial plane. From (15) the magnetic field components follow as

$$B_{CF,\rho} = -\sum_{m,i} K_i \left[\frac{m}{K_i \rho} J_m(K_i \rho) - J_{m+1}(K_i \rho) \right] A_{m,i} \sin m\alpha\, e^{K_i z},$$

$$B_{CF,\alpha} = -\sum_{m,i} J_m(K_i\rho)A_{m,i}\cos m\alpha\, e^{K_i\rho}, \quad \times \frac{m}{\rho} \tag{16}$$

$$B_{CF,z} = -\sum_{m,i} K_i J_m(K_i\rho)A_{m,i}\sin m\alpha\, e^{K_i z}.$$

Although the real magnetosphere expands in the tailward direction, using of the cylindrical harmonics in the expansions (15)–(16) is justified by that they yield a divergenceless field with a proper distribution along the tail. Eight coefficients $A_{m,i}$ (for $m = 1, 3$ and $1 \le i \le 4$) and the factors K_i in the Bessel function arguments were least-squares fitted to obtain the best agreement of the model field (16) in the tail region with that derived by means of a direct integration over the self-consistent magnetopause.

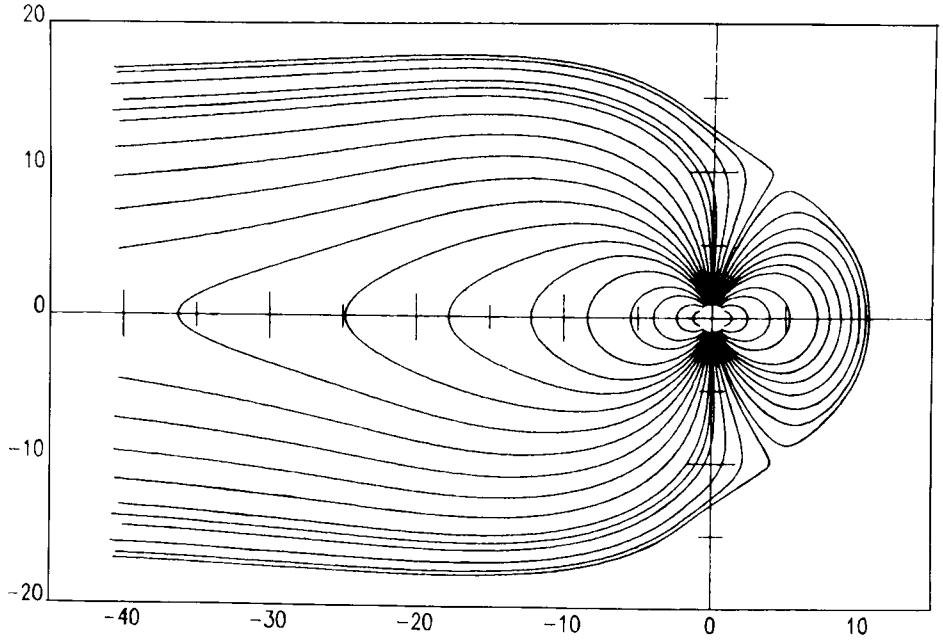

Fig. 4. Magnetic field configuration in the noon–midnight meridian corresponding to the cylindrical harmonic expansions (16) for the boundary field in the tail in conjunction with a spherical harmonic representation at the dayside. The tail source contribution is given by the model of Beard (1979) (Beard *et al.*, 1982).

Figure 4 shows the noon–midnight meridional field line plot in the model by Beard *et al.* (1982), where the field $\mathbf{B}_{CF}$ in the tail is provided by the expansions (16) in conjunction with the spherical harmonic representation (13) for the near-magnetospheric region and the Beard's (1979) model for the contribution from the tail current system (see Subsection 2.3.1). Expansions (13) and (15) replace each other on traversing the plane $x_{GSM} = -1.5\,R_E$. The corresponding jumps in the field components are insignificant in comparison with the total field magnitude, so that the kinks on the field lines are scarcely discernible on the plots. An alternative expression for the tailward part of the

$\mathbf{B}_{CF}$ was also tried in that work, which did not require evaluating the Bessel functions and provided a good fitting to the boundary field.

This model, however, is seriously handicapped by being restricted to the case of zero geodipole tilt. Another disadvantage stems from the separate representation of the field in the two regions. Anticipating the material of Subsection 2.3.1, it should be noted that such an approach is adopted in several works (e.g., Alekseev *et al.*, 1975; Voigt, 1981; Schulz and McNab, 1987) in attempt to avoid the troublesome problems arising due to a drastic difference in the magnetic field structures of the dayside and nightside magnetosphere. However, it by no means can be considered as a satisfactory way out, since the boundary between the domaine of a quasi-dipolar and tail-like field is highly variable, conventional, and vague. In any case, it cannot be approximated by a planar surface because the near-Earth tail current sheet may well extend into the evening and morning sectors. This region is of key importance in the aspect of the substorm physics, and therefore it is desirable to have a unified model representation of the magnetic field in the whole near magnetosphere.

As a closing remark, it should be reminded that so far we have dealed with the boundary current shielding the geodipole only. Of the other large-scale magnetic field sources only the ring current can be relatively easily incorporated into the framework of the present approach, since it is the only extraterrestrial current system wholly closed inside the magnetosphere. Taking into account that its characteristic radius is significantly less than the subsolar point distance, it can be assumed that the necessary changes in the expansions for $\mathbf{B}_{CF}$ can be reduced to a scaling transformation equivalent to an increase of the geodipole magnetic moment M_E by a value M_{RC} pertaining to the ring current. The corresponding scaling distance R_0 in (13) should be multiplied by a factor $\gamma = (1 + M_{RC}/M_E)^{1/3}$. In this approximation it is also rather easy to take into account slow variations of the solar wind pressure which are not accompanied by an additional injection of particles into the ring current. Indeed, as shown by Stern (1985), during such an adiabatic compression or expansion of the magnetosphere the magnetic moment of the ring current and hence the factor γ remain constant.

A self-consistent treatment of shielding the tail current sheet as well as Birkeland currents poses a much more complex problem. The main difficulties stem here from the absence of a more or less clear physical concept for formation of these current systems and their dependence on the solar wind state. We shall discuss this question in more detail in Subsection 2.2.2.

2.2.2. *Models with a Predetermined Magnetopause*

A general approach in this case is as follows. The shape of the boundary surface S and the distribution of the field from the intramagnetospheric sources $\mathbf{B}_{IM}$ are considered as given functions of the coordinates which may also contain several parameters including the geodipole tilt angle. Suppose also that at any point near the boundary the condition $\nabla \times \mathbf{B}_{IM} = 0$ is satisfied. It means that the intramagnetospheric currents do not approach the magnetopause, being completely closed inside the magnetosphere. In

such a case the system of shielding boundary currents is also fully closed at the surface and hence the corresponding magnetic field $\mathbf{B}_{CF}$ is irrotational and can thus be represented inside the cavity as

$$\mathbf{B}_{CF} = -\nabla U_{CF},$$

where the scalar potential U_{CF} satisfies Laplace's equation

$$\Delta U_{CF} = 0. \tag{17}$$

The normal component of the total field should be continuous at the boundary S and, because of the complete shielding condition, it must be zero everywhere on S

$$(\mathbf{B}_{IM} + \mathbf{B}_{CF})_n \mid_S = 0 \tag{18}$$

and, hence, we obtain Neumann's boundary condition for the potential

$$\left.\frac{\partial U_{CF}}{\partial n}\right|_S = B_{IM_n}. \tag{19}$$

The problem (17)–(19) is linear and can thus be solved separately for every source contributing to the field $\mathbf{B}_{IM}$, with the subsequent summation of results. In particular, this suggests the simplest way of obtaining the solution for the tilted dipole (Alekseev and Shabansky, 1972). Since the tilted dipole can be represented as the superposition of a parallel and a perpendicular ones

$$\mathbf{M} = M \sin\psi \mathbf{e}_x + M \cos\psi \mathbf{e}_z = \mathbf{M}_{\parallel} + \mathbf{M}_{\perp}, \tag{20}$$

the solution can be obtained as a linear combination of potentials corresponding to cases $\psi = \pi/2$ and $\psi = 0$ with the weights equal to $\sin\psi$ and $\cos\psi$, respectively, so that

$$U_{CF} = U_{CF_{\parallel}} \sin\psi + U_{CF_{\perp}} \cos\psi. \tag{21}$$

Further details depend on a concrete choice of the boundary shape. In one of the first papers devoted to this approach Alekseev and Shabansky (1972) proposed to describe the magnetopause by a paraboloid of revolution having its focus just halfway between the geodipole and the subsolar point. Later on this model was modified by the inclusion of the tail current sheet (Alekseev *et al.*, 1975) and recently Stern (1985) proposed a more convenient method for representation of the geodipole and the ring current shielding field by means of the parabolic harmonics. These results are considered below in more detail.

2.2.2.1. *Paraboloid Model.* The paraboloid coordinates (λ, μ, φ) can be related to the Cartesian solar-magnetospheric ones (x, y, z) as follows

$$\lambda^2 = r + x - x_0; \qquad \mu^2 = r - x + x_0; \qquad \tan\varphi = z/y, \tag{22}$$

where $r = [(x - x_0)^2 + y^2 + z^2]^{1/2}$, the parameter x_0 defining the location of the paraboloid focus on the x-axis. The durfaces λ = const. yield a family of paraboloids which

are convex towards the Sun, so that one of them with $\lambda = \lambda_0$ can be taken as a model magnetopause. The second family of the coordinate surfaces μ = const. is orthogonal to the first one. These are convex in the tailward direction and larger values of μ correspond to larger geocentric distances down the tail, as shown in Figure 5. The azimuthal angle φ is measured from the positive y direction around the x-axis.

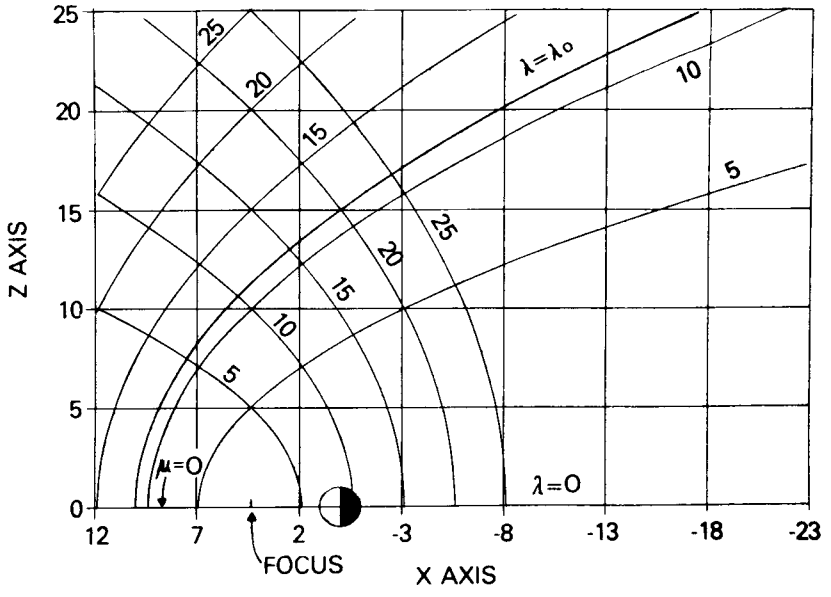

Fig. 5. Paraboloid coordinates (λ, μ) in the $x - z$ plane. Contours of constant λ^2 and μ^2 are drawn at intervals of five units (Stern, 1985).

The finite solutions of Laplace's Equation (17) inside the paraboloid $\lambda = \lambda_0$ can be obtained by separating the variables in a form of the general expansion

$$U_{CF} = \sum_{m=0}^{\infty} \begin{Bmatrix} \sin m\varphi \\ \cos m\varphi \end{Bmatrix} \int_0^{\infty} J_m(K\mu) a_m(K) I_m(K\lambda)\, \mathrm{d}K\,, \tag{23}$$

where the functions $a_m(K)$ can be found from the boundary conditions (19) using an inverse integral transform. It is just the approach that was adopted by Alekseev and Shabansky (1972). Stern (1985) suggested an effective method for reducing the integrals in (23) to finite sums. The basic idea is to impose an additional boundary condition

$$\left.\frac{\partial U_{CF}}{\partial \lambda}\right|_{\mu = A} = 0$$

in the far tail region. As a result, the initially continuous spectrum of eigenvalues K is transformed into a discrete one and we obtain a sum corresponding to a set of roots of the Bessel functions.

For the cases of parallel and perpendicular dipole the expansions have the form

$$U_{CF_{\parallel}} = \sum_{n=1}^{\infty} a_{0n} J_0(K_{0n}\mu) I_0(K_{0n}\lambda), \tag{24}$$

$$U_{CF_{\perp}} = \sum_{n=1}^{\infty} a_{1n} J_1(K_{1n}\mu) I_1(K_{1n}\lambda) \sin\varphi, \tag{25}$$

where K_{0n} and K_{1n} satisfy the equations $J_0(KA) = 0$ and $J_1(KA) = 0$, respectively. Figure 6 shows a magnetic field line plot for the case of an almost parallel ($\psi = 80°$) dipole orientation. The tailward extension of the region of validity of the model is defined by the value of A and by the number of terms in the sums (24)–(25).

Of essential importance for practical purposes is a possibility to make a simple recalculation of the field $\mathbf{B}_{CF}$ for different values of the dynamical pressure of the solar wind. In the paraboloid model the boundary is fully defined by the parameters λ_0 and x_0. Given new values of λ_0 and x_0, the whole procedure of computing the set of

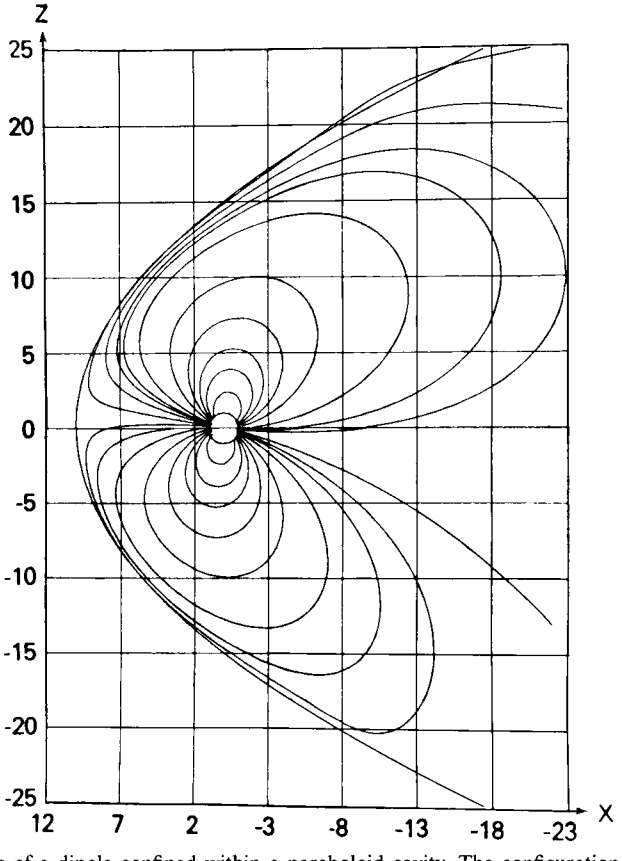

Fig. 6. Field lines of a dipole confined within a paraboloid cavity. The configuration corresponds to a hypothetical structure of the Uranian magnetospheres, which had been expected before 1986 (Stern, 1985).

coefficients should be applied once again. However, this can be avoided by imposing the condition of a self-similar contraction or expansion of the paraboloid cavity with respect to the geodipole location, in line with the results of self-consistent calculations (Subsection 2.2.1). In such a case the changes of the paraboloid dimensions are controlled by the single similarity factor $K = (p_d/p'_d)^{1/6}$, where p_d and p'_d are the 'old' and the 'new' values of the solar wind ram pressure. Then the 'new' expansion for the boundary field potential can be easily obtained from the 'old' one as (Stern, 1985)

$$U'_{CF\parallel,\perp}(\lambda, \mu, \varphi) = K^{-2} U_{CF\parallel,\perp}(\lambda K^{-1/2}, \mu K^{-1/2}, \varphi) . \tag{26}$$

In addition to these results, we note that an alternative approach to the paraboloid shielding problem was proposed by Pudovkin *et al.* (1971). In that work a potential of the total field was sought inside the cavity, $U = U_{CF} + U_d$, so that $\mathbf{B}_d + \mathbf{B}_{CF} = -\nabla U$, in contrast with (17)–(19). The boundary conditions become much simpler in this case, namely $\partial U/\partial n|_S = 0$, but Laplace's Equation (17) is replaced by Poisson's one

$$\Delta U = -4\pi\rho_m ,$$

with a delta-like right-hand side ρ_m corresponding to the dipole source in the origin. The problem was solved by an integral transform method yielding a parabolic harmonic series which resemble (24)–(25).

As already noted in Subsection 2.2.1, the problem of shielding the other magnetospheric sources can be solved in a more or less simple way only for the ring current. As a crude approximation, it is enough to make a proper modification of the Earth's magnetic moment as $M_E \to M'_E = M_E + M_{RC}$ with a subsequent recalculating of the scale distance R_0. A more sophisticated analysis is also possible on the basis of existing analytic representations of the ring current field. One of such simple models described by Tsyganenko and Usmanov (1982) (Subsection 2.3.3) was used by Stern (1985) for incorporating the ring current effects in the paraboloid model. However, the corresponding expressions (68)–(69) include a characteristic scale radius ρ_0 and thus the model ring current magnetic field, in contrast with the dipolar one, is not self-similar. For this reason the coefficients in the expansion for the boundary field potential should be computed for several values of ρ_0, in order to be able to take into account variations of the solar wind pressure as well as changes of the ring current dimension by means of a scaling procedure.

An empirical account of the tail plasma sheet current in the framework of a model with a predetermined magnetopause meets with a difficulty stemming from that this current system is not entirely confined inside the magnetosphere, but closes via the magnetopause surface and thus the shielding current must include the closure circuit in a self-consistent manner. First attempts to solve this problem were based on a separate treatment of the contribution coming from the intramagnetospheric portion of the whole tail current system approximated by a planar current sheet with a finite width in the dawn-dusk direction (Alekseev and Shabansky, 1972; Voigt, 1972). The corresponding expressions were incorporated in the term $\mathbf{B}_{IM}$ in (18) and then a boundary value problem for the shielding field potential was solved. However, this approach appeared

to be a misleading one, since the shielding surface current does not satisfy the continuity condition, i.e., $\nabla \cdot \mathbf{J}_{CF} \neq 0$ at the site of the magnetopause contact with the edges of the equatorial current sheet. As a result, we have $\nabla \times \mathbf{B}_{CF} \neq 0$ and, hence, the representation $\mathbf{B}_{CF} = -\nabla U_{CF}$ cannot be applied.

Later on Alekseev *et al.* (1975) proposed the following correct solution to the problem of a self-consistent tail current system in the paraboloid model. The interior of the paraboloid cavity $\lambda = \lambda_0$ is divided by a surface $\mu = \mu_0$ into two domains I and II, as shown in Figure 7 by a double shading. The domain II corresponds to the magnetotail

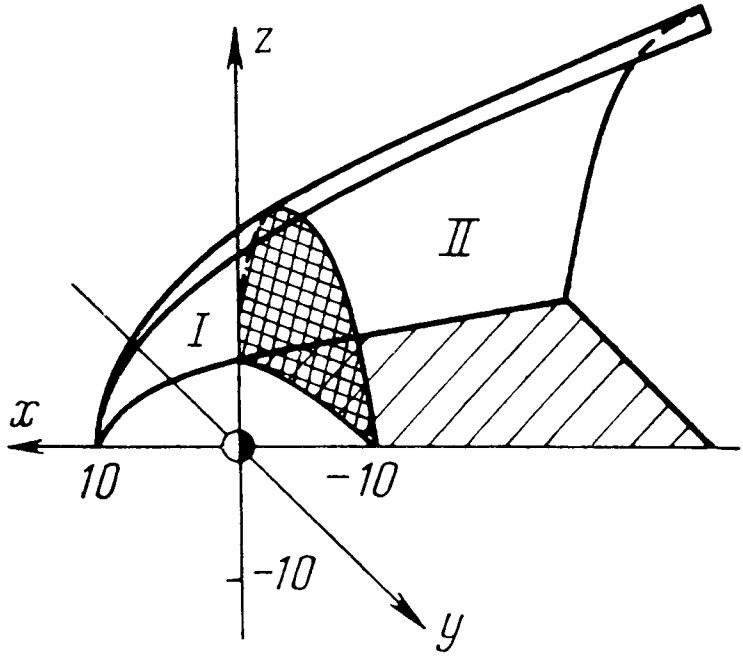

Fig. 7. Illustrating geometry of the paraboloid model with a self-shielded closed current sheet, the latter being shown by a single hatching. The region I (near magnetosphere) is separated from the tail region II by the surface $\mu = \mu_0$ shown by a double hatching (Alekseev *et al.*, 1975).

and is divided into two halves by an infinitively thin equatorial current sheet (single shading in Figure 7). On traversing the sheet the tangential field component reverses abruptly, while the near magnetospheric region I is current-free. The total magnetic field produced by the current sheet together with the closure system distributed throughout the paraboloid surface is curl-free and can be sought as $\mathbf{B} = -\nabla U$ inside the cavity. The solutions of Laplace's equation for the potential are derived separately in the regions I and II in the form of Bessel function series satisfying the boundary condition $B_n = 0$ at the magnetopause, while at the fictitious surface $\mu = \mu_0$ it is required that $B_n|_{\mu=\mu_0} = B_T \operatorname{sign}(z)$. This condition specifies the magnitude of the tail lobe magnetic field by means of the parameter B_T, whereas its jump across the equatorial plane defines

the distribution of the current in the tail sheet chosen in that work to be proportional to $|x|^{-1/2}$. At this stage, however, there still remains a discontinuity in the tangential field component at the surface $\mu = \mu_0$; it can be removed by adding to the solution an expansion which does not change the electric current distribution in the equatorial sheet. The final expansions for the potential are as follows:

$$U_{\mathrm{I}} = \frac{4}{\pi} B_T \mu_0 \sum_{l=1} \sum_{m=0} \frac{(-1)^m \sin(n\varphi)}{n} A_{lm} J_n(k_{nl}\lambda) I_n(k_{nl}\mu) \tag{27}$$

in the domain I, and

$$U_{\mathrm{II}} = B_T \mu_0 [\operatorname{sign}(\pi - \varphi) \ln \mu] + \\ + \frac{4}{\pi} \sum_{l=1} \sum_{m=0} \frac{(-1)^m \sin(n\varphi)}{n} B_{lm} J_n(k_{nl}\lambda) K_n(k_{nl}\mu) \tag{28}$$

in the domain II ($n = 2m + 1$).

Magnetic field lines computed from (27)–(28) are wholly confined inside the paraboloid and exhibit kinks on crossing the current sheet. The current streamlines in the central sheet are almost coincident with the parabolic-shaped contours $\mu = \text{const.}$ and the closure current is distributed over the whole magnetopause including its dayside part.

In his later work Alekseev (1978) modified the model by including the effects of the geodipole tilting. In respect to the dipole shielding field it was achieved by taking a superposition (21) of the potentials $U_{CF_\perp}$ and $U_{CF_\parallel}$, while the tail current response was simulated by shifting the whole sheet perpendicularly to the equatorial plane. Figure 8 displays the magnetic field configuration obtained in the paraboloid model by Alekseev (1978), the arrows indicating the average field directions measured onboard the HEOS-1 and -2 spacecraft near the midnight meridian plane (Hedgecock and Thomas, 1975). In the lower part of the figure a model magnetic field line plot obtained from the same HEOS dataset by Hedgecock and Thomas (1979) is shown.

An undoubtful advantage of this model is a conceptually rigorous approach to the problem of derivation of a completely self-shielded tail-current system, while its most serious shortcomings are related mainly to the adopted central current sheet representation. In fact, it has only two free parameters (B_T and μ_0) and is incapable of incorporating very important effects including finite thickness of the sheet and its warping due to the geodipole tilt, which will be discussed in Subsection 2.3.1.

2.2.2.2. *Ellipsoid Model.* The paraboloid model magnetopause shows satisfactory agreement with the observed boundary only within a comparatively limited range of geocentric distances with $x_{\mathrm{GSM}} \gtrsim -20\ R_E$. At larger tailward distances it expands too rapidly, so that some other approximations are necessary in that region. Stern (1985) suggested a method which provides a modification of the coefficients of the paraboloid model expansions (24)–(25) having generalized them to non-parabolic boundaries. The method is based on an iterative calculation of the coefficients under assumption that

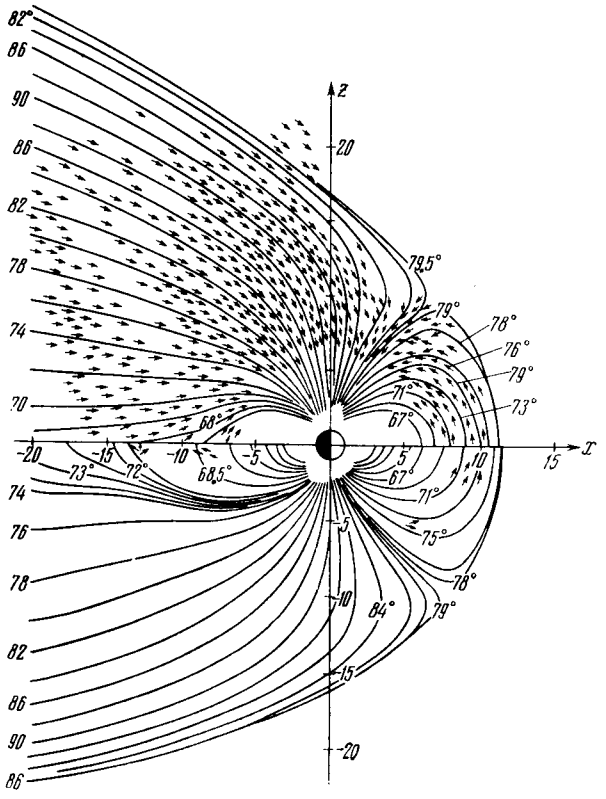

Fig. 8. Magnetic field configuration in the paraboloid model (the upper half of the plot) in comparison with that in the empirical model of Hedgecock and Thomas (1979) (below). The field lines are labeled by values of footpoint latitude, and the arrows indicate the magnetic field directions observed by the HEOS spacecraft near the noon–midnight meridian plane (Alekseev, 1978).

the equation yielding the actual shape of the boundary can be represented in the form

$$\lambda = \lambda_0 + \Delta\lambda(\mu, \varphi)\,,$$

where the correction term $\Delta\lambda(\mu, \varphi)$ is relatively small, so that a linear perturbation technique could be applied. However, both the purely paraboloid model and its extension to non-parabolic boundaries require the evaluation of the ordinary (J_0, J_1) and modified (I_0, I_1) Bessel functions, which is not always convenient in practical calculations.

There exist one more analytical representation for the magnetospheric boundary leading to very simple expansions for the shielding field potentials, namely, the ellipsoid model (Tsyganenko, 1989c). In the front magnetospheric region $x_{GSM} \gtrsim -30\,R_E$ an oblong ellipsoid of revolution provides excellent approximation to the observed magnetopause. At larger distances the ellipsoid surface tapers down and closes. However, contributions from both the geodipole and the boundary sources do not exceed a few tenths of nanotesla in this region, which is at least by an order of magnitude less than that from the tail current sheet. Therefore, the ellipsoid model for the dipole

shielding field can actually be used up to its rear boundary which may be placed at distances of the order of lunar orbit radius or even farther.

The ellipsoidal coordinates for representing the magnetospheric domain can be defined as follows (Korn and Korn, 1961)

$$\begin{aligned} \sigma &= (2a^2)^{-1/2}(s^2 + \sqrt{s^4 - 4a^2x'^2})^{1/2}, \\ \tau &= (2a^2)^{-1/2}(s^2 - \sqrt{s^4 - 4a^2x'^2})^{1/2}\,\mathrm{sign}(x'), \\ \varphi &= \tan^{-1}(z/y), \end{aligned} \tag{29}$$

where

$$x' = x - x_o + a, \qquad s^2 = a^2 + x'^2 + y^2 + z^2.$$

Here a is the half-distance between the focuses of the ellipsoid, as shown in Figure 9. In the same picture several contours of constant σ and τ are shown. The interior of the ellipsoidal cavity corresponds to the intervals $1 \leq \sigma \leq \sigma_0$, $|\tau| \leq 1$, $0 \leq \varphi \leq 2\pi$. The magnetopause location is defined completely by specifying the values of the parameters x_0, a, and σ_0. The subsolar point distance and the radius of the dawn-dusk crosssections

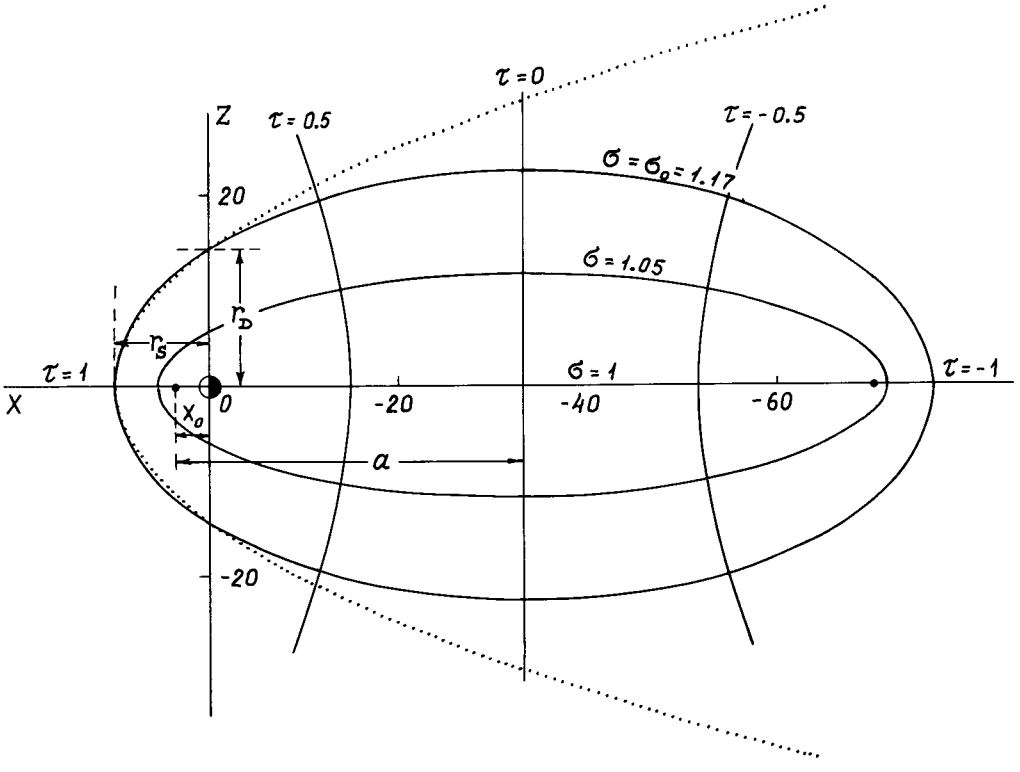

Fig. 9. Ellipsoid coordinates in the $x - z$ plane. The ellipsoid with $\sigma = \sigma_0 = 1.17$ represents the magnetopause having $R_s = 10\,R_E$ and $R_D = 14.37\,RE_E$. A paraboloid with the same parameters R_s and R_D is shown by the dotted line.

are, respectively,

$$R_s = x_0 + a(\sigma_0 - 1), \qquad R_D = [R_s(1 - \sigma_0^{-2})(2a\sigma_0 - R_s)]^{1/2}.$$

The inverse transformation from the ellipsoidal coordinates to Cartesian ones reads as follows

$$\begin{aligned} x &= x_0 - a(1 - \sigma\tau), \\ y &= a[(\sigma^2 - 1)(1 - \tau^2)]^{1/2} \cos\varphi, \\ z &= a[(\sigma^2 - 1)(1 - \tau^2)]^{1/2} \sin\varphi. \end{aligned} \tag{30}$$

A search for appropriate values of the ellipsoid parameters gave: $x_0 = 3.71\ R_E$, $a = 37\ R_E$, and $\sigma_0 = 1.17$, which yield a good agreement with the average observed magnetopause shape (Fairfield, 1971) up to tailward distances $x \sim -30\ R_E$. These values give $R_s = 10\ R_E$ and $R_D \approx 14.37\ R_E$. The maximal radius of the cavity (minor semi-axis) equals $R_M = a(\sigma_c^2 - 1)^{1/2} \approx 22.47$ at $x = x_0 - a \approx -33.3\ R_E$. The position of the boundary corresponding to these values is shown in Figure 9 by the heavy solid line.

A general solution to the boundary value problem leads in this case to the following expansion for the potential U_{CF}

$$U_{CF} = \sum_{n=1}^{\infty} \sum_{m=0}^{n} P_n^m(\sigma) P_n^m(\tau)(a_{nm} \cos m\varphi + b_{nm} \sin m\varphi), \tag{31}$$

where P_n^m are the associated Legendre functions of the first kind. Due to axial symmetry of the shielding potential $U_{CF_\parallel}$ for the parallel dipole and a sinusoidal dependence on φ in the boundary condition for $U_{CF_\perp}$, the general expansion (31) can be reduced to more simple ones

$$\begin{aligned} U_{CF_\parallel} &= \sum_{n=1}^{\infty} a_{0n} P_n(\sigma) P_n(\tau), \\ U_{CF_\perp} &= \sin\varphi \sum_{n=1}^{\infty} a_{1n} P_n^1(\sigma) P_n^1(\tau). \end{aligned} \tag{32}$$

The coefficients here can be easily determined from the boundary conditions by means of an inverse integral transform.

It can be shown that the corresponding expansions for the magnetic field components truncated to the leading N terms can be reduced to polynomials of variables $t = \sigma\tau = (x'/a)^2$ and $v = \sigma^2 + \tau^2 = (x'^2 + y^2 + z^2 + a^2)/a^2$, that is to polynomials of Cartesian coordinates. Their degree depends on the assumed length N of the truncated expansions (32). Calculations show that for $N = 10$ the model yields good results up to tailward distances 40–50 R_E; explicit form of the polynomials as well as the tables of their coefficients are given by Tsyganenko (1989c). Figure 10 shows the field line plots obtained in the ellipsoid model for $N = 10$.

As in the case of the paraboloid model, it is no trouble to recalculate the magnetic field components in case of self-similar changes of the ellipsoid dimensions by a single

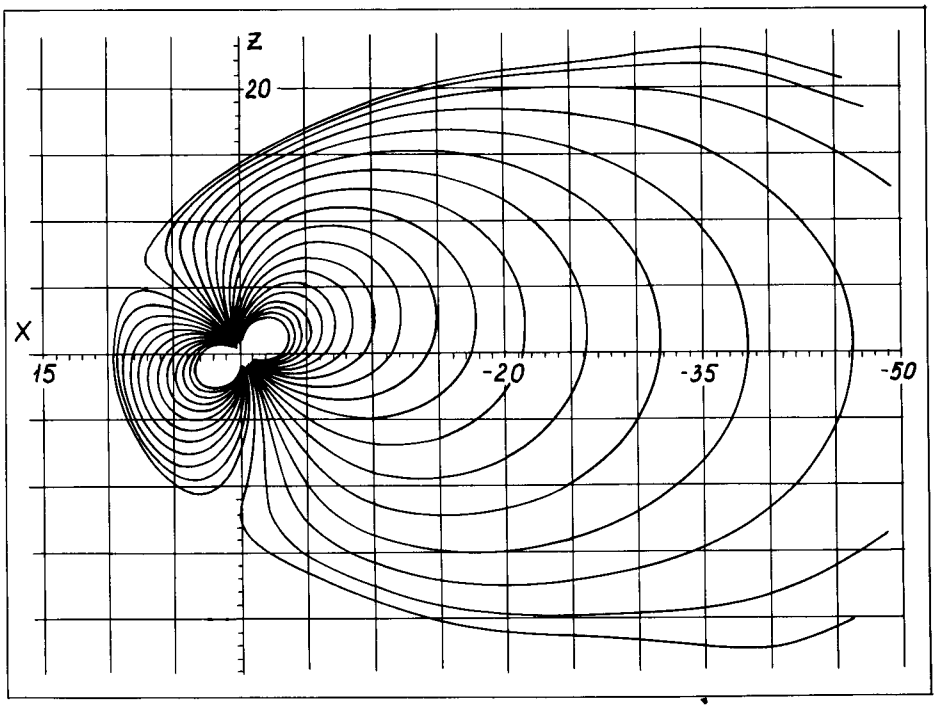

Fig. 10. Field lines of a dipole confined within the ellipsoidal cavity shown in Figure 9, calculated by using the expansions (32) with $N = 10$ (Tsyganenko, 1989c).

factor K. All the coefficients acquire the factor K^{-2} and, therefore, the magnetic field scales by K^{-3} at any point with fixed values of the ellipsoidal coordinates (σ, τ, φ). Thus, to obtain new values of B_x, B_y, B_z at a fixed point (x, y, z) it is necessary to calculate new values of the parameters $a' = aK$ and $x' = x_0K$ corresponding to the new magnetopause location. After that we find new values of the variables t and v and, having evaluated the polynomials for the field components, multiply the result by the factor K^{-3}.

The ellipsoid model allows a simple comparison with the paraboloid one, which can be done very easily by taking

$$\sigma_0 = (1 - R_D^2/2aR_s)^{-1/2} \quad \text{and} \quad x_0 = R_s - R_D^2/4R_s$$

with a sufficiently large value of a. In this case the front region of the ellipsoidal surface ($|x| \ll a$) is asymptotically close to a paraboloid having the same values of R_s and R_D (shown by the dotted line in Figure 9). A test calculation has shown that the difference in the magnetic field components between these two models is small, so that both of them can be applied in principle, although the ellipsoid one is more simple from the computational point of view.

2.2.2.3. *A Composite Magnetopause Model of Voigt.* Voigt (1972) suggested a model, in which the magnetopause is simulated by a composite surface consisting of a semi-infinite cylinder capped by a hemisphere at the dayside part, as sketched in Figure 11. The geodipole is shifted towards the Sun with respect to the centre of the sphere, in order to keep a proper relationship between the geocentric distance R_s to the subsolar point and the tail radius R_T.

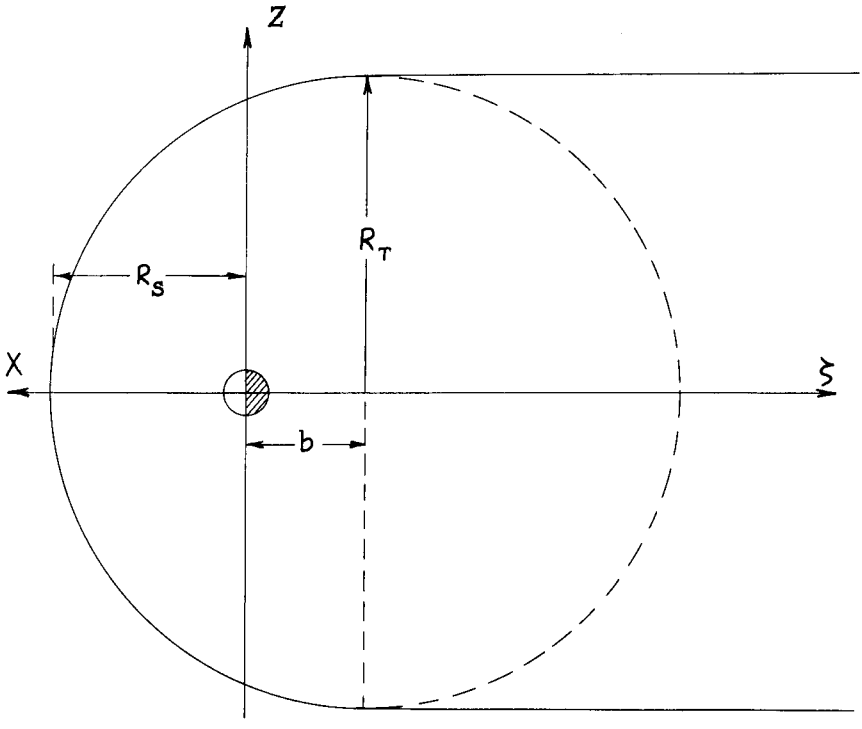

Fig. 11. Magnetopause shape assumed in the model of Voigt (1972, 1981).

A general approach to the problem is the same as for the above described models. However, some mathematical complications arise due to the composite shape of the surface. In the near magnetosphere ($x \geq -b$) the scalar potential U_{CF} is expanded in a spherical harmonic series

$$U_{CF} = \sum_{n=1} \frac{1}{n} Y_n(\theta, \varphi) \frac{R^n}{R_T^{n-1}}, \tag{33}$$

where

$$Y_n(\theta, \varphi) = a_n^0 P_n(\cos\theta) + \sum_{m=1}^{n} (a_n^m \cos m\varphi + b_n^m \sin m\varphi) P_n^m(\cos\theta).$$

The coefficients a_n^m and b_n^m are found from the distribution of the normal component of the field $\mathbf{B}_M$ throughout the whole sphere including the front magnetopause surface and its complementary half inside the cavity shown in Figure 11 by the broken line. In the tail region $x \leq -b$ Laplace's equation in the cylindrical coordinates (ρ, φ, ζ) is solved, where $\zeta = -x - b$. Note that the total potential $U = U_d + U_{CF}$ is to be found here, rather than the shielding one only. This makes possible to represent the solution as a discrete series in cylindrical harmonics which correspond to a set of eigenvalues ξ_i satisfying the equation $J_1'(\xi) = 0$. The expansion reads as follows

$$U_1(\rho, \varphi, \zeta) = -M_E \cos\varphi \frac{2}{R_T^2} \sum_{i=1}^{\infty} a_i J_1(\xi_i \rho / R_T) \exp(-\xi_i \zeta / R_T) \tag{34}$$

and satisfies the shielding boundary condition at the cylindrical surface

$$B_n = \left.\frac{\partial U_1}{\partial \rho}\right|_{\rho = R_T} = 0$$

as well as the requirement of continuity of the total potential on the plane $x = -b$

$$U_1(\rho, \varphi, 0) = (U_d + U_{CF})|_{x = -b}. \tag{35}$$

The condition (35) uniquely defines the coefficients of the expansion (34). However, there remains a discontinuity in the normal derivative of the potential at this planar surface. This difficulty was overcome by means of an iterative fitting the coefficients of the expansions (33) and (34), in which successive corrections of the boundary conditions at the planar 'partition' and the internal hemisphere were done.

Later on Voigt (1981) proposed a generalized version of the model, in which the effect of partial penetration of the interplanetary magnetic field into the magnetosphere was incorporated (account of the tail-current system and the ring current in the model will be discussed in Subsection 2.3.1). The main idea of this approach is to formally postulate the existence of a small transverse component of the magnetic field at the magnetopause, putting aside all the questions concerning the physics of the reconnection. Solution of the boundary problem in this formulation can be easily obtained from that derived earlier for the case of an ideally shielded magnetosphere, provided the normal component at the magnetopause is assumed to be proportional to the contribution from all the internal sources, the interconnection coefficient C_I being taken to be constant throughout the whole surface. The boundary condition (18) is replaced thus by a more general relation

$$(\mathbf{B}_{IM} + \mathbf{B}_{CF})_n|_S = C_I \mathbf{B}_{IM_n}|_S.$$

Defining the boundary field to be found as $\mathbf{B}_{CF} = -\nabla U_{CF}^*$ and using the assumed constancy of the factor C_I, we express the potential U_{CF}^* in terms of that corresponding to the case of a complete shielding which is given by the expansions (33)–(34), so that

$$U_{CF}^* = (1 - C_I) U_{CF}.$$

Introducing a similar constant C_E, which defines a fraction of the IMF penetrating into the magnetosphere from the interplanetary space, we have finally the total field inside

$$\mathbf{B}_{\text{int}} = \mathbf{B}_{IM} - (1 - C_I)\nabla U_{CF} + C_E \mathbf{B}_{EM} \tag{36}$$

and in the outer space

$$\mathbf{B}_{\text{ext}} = \mathbf{B}_{EM} - (1 - C_E)\nabla U_{CF}^{(E)} + C_I \mathbf{B}_{IM}\,, \tag{37}$$

where $U_{CF}^{(E)}$ is the potential of the magnetopause current system, which provides an ideal shielding of the interplanetary field $\mathbf{B}_{EM}$, fully preventing it from penetrating into the magnetosphere. In the case of a uniform $\mathbf{B}_{EM}$ addressed in the Voigt (1981) work the corresponding potential is easily obtained in a compact form.

Figure 12 shows an example of the magnetospheric configuration obtained by Voigt (1981) for an oblique orientation of the IMF, where the interconnection constants were taken as $C_I = C_E = 0.1$.

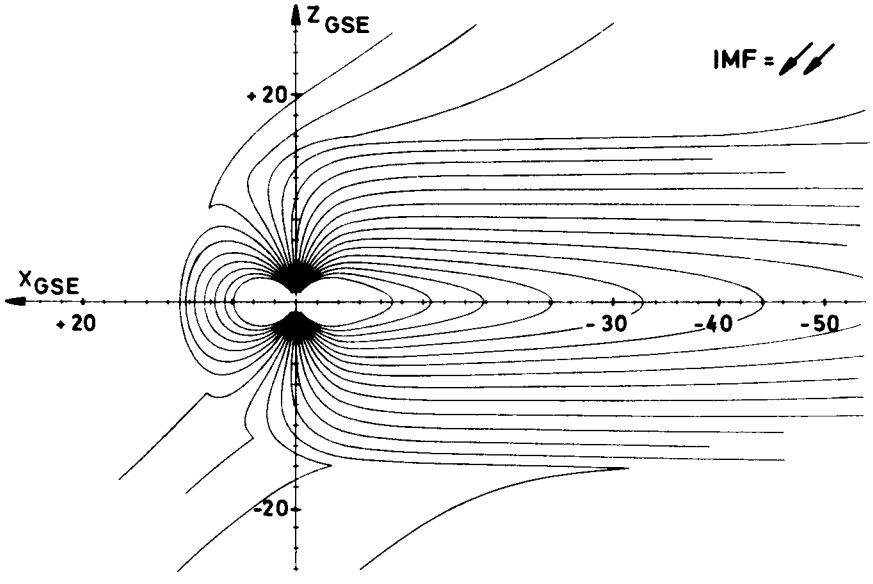

Fig. 12. Model magnetic field configurations in the noon–midnight meridian for an oblique orientation of the interplanetary magnetic field (Voigt, 1981).

2.2.2.4. *Numerical Methods for Boundaries of More General Shape.* The above described works exhaust all existing models with a predetermined magnetopause in which, owing to a special choice of the boundary shape, analytic representation of the potential U_{CF} is possible. In case of more complex boundaries, which do not allow to introduce a convenient coordinate system for separating variables in Laplace's equation, numerical methods have to be applied. Mead and Beard (1964) were first to be faced with this problem; as already outlined in Subsection 2.2.1, the essence of their method consists

in dividing the shielding field near the boundary into a leading term $\mathbf{B}_p$ and a small correction one $\mathbf{B}_c$, which allows to apply a successive iteration technique.

This approach with some modifications was used by Tsyganenko (1976, 1981) in calculations of a shielding current system at the magnetopause defined by an analytical function $R = R(\theta, \varphi, \psi)$ of spherical coordinates containing a parametric dependence on the geodipole tilt angle. A concrete form of this function was specified by fitting various model boundaries to the average magnetopause shape (Fairfield, 1971) as well as comparing it with the self-consistent surfaces obtained by Choe *et al.* (1973). Instead of Equation (12) an equivalent one was solved for the surface current density $\mathbf{J}(\mathbf{R})$

$$\mathbf{J}(\mathbf{R}) = (c/2\pi)\left[\mathbf{B}_{IM} + \frac{1}{c}\int\limits_{S-\Delta S} \frac{\mathbf{J}(\mathbf{R}')\times(\mathbf{R}-\mathbf{R}')}{|\mathbf{R}-\mathbf{R}'|^3}\,ds'\right]\times \mathbf{e}_n\,, \tag{38}$$

where, in contrast with the Mead–Beard problem, the magnetic field of magnetosphoric sources $\mathbf{B}_{IM}$ contains not only the geodipole contribution $\mathbf{B}_d$, but also that from the intramagnetospheric part of the tail-current system. The magnetopause current $\mathbf{J}(\mathbf{R})$ obtained from (38) by means of an iterative procedure contains also the return current system which closes the central current sheet via the magnetospheric boundary. This result was evidenced a posteriori by a direct inspection of the obtained surface current distributions and can be easily understood from simple considerations, although its rigorous proof was not found. As a matter of fact, it can be verified for a simplest case of a semi-infinite linear wire current adjoining perpendicularly a planar boundary. A precise solution to this problem is given already by the first approximation which neglects the integral term in (38). Bearing in mind the linearity of the predetermined boundary problem, it is possible to generalize this result to the case of the current sheet with an arbitrary distribution of the current density. The main advantage of this method consists in its applicability to boundaries of arbitrary shape. However, since it provides the electric current distribution in a numerical form, subsequent search for a sufficiently simple analytic approximation for the corresponding magnetic field is necessary.

Schulz and McNab (1987) proposed one more method capable of modeling the boundary field without explicit treatment of the Biot–Savart integrals and valid for surfaces of rather general shape. The modeling region in their approach, just as in the models of Voigt (1972, 1981), Alekseev *et al.* (1975), and Beard *et al.* (1982), is divided into the near magnetospheric region S and the tail T, as shown in Figure 13. The field in the region S is assumed to be curl-free and can thus be represented by a scalar potential expansion similar to (13), together with a dipole term. In the tail region T the solution is constructed geometrically, starting from the requirement of continuity of the normal component B_n at the boundary Σ between the regions S and T and postulating the shape of the field lines so that they do not cross the neutral sheet and the magnetopause M'. The coefficients of the potential expansion for the region S were treated as free parameters of the model and their numerical values were found by

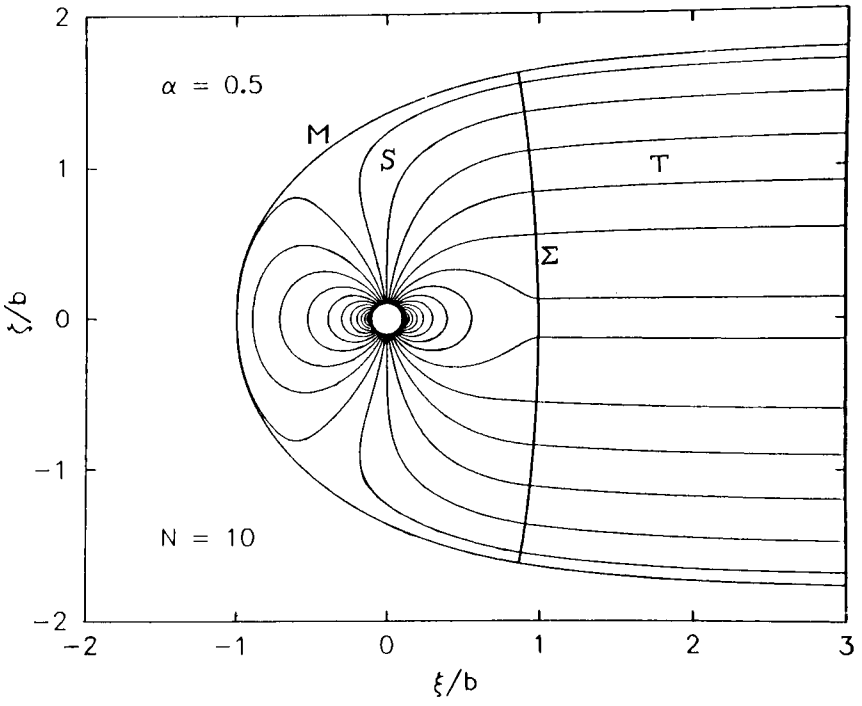

Fig. 13. Magnetic field configuration in the noon–midnight meridian obtained from the variational principle using the functional (39) with $\alpha = 0.5$ (Schulz and McNab, 1987).

minimizing the variational quantity

$$\sigma = \alpha \int_M (\mathbf{n} \cdot \mathbf{B})^2 \, dS + (1 - \alpha) \int_\Sigma (\mathbf{n} \cdot \mathbf{B})^2 \, dS \,. \tag{39}$$

The first term in (39) is the integral of the squared normal component of **B** over the near part M of the model magnetopause multiplied by a weight factor α ($0 \leq \alpha \leq 1$). The second one contains the integral of the squared tangential field component over the 'partition' Σ. Thus, instead of the strict requirement of perfect shielding of the magnetospheric field sources, a compromise one is imposed in a form of the variational principle. On the other hand, the above-mentioned difficulty with explicitly specifying the tail-current sheet contribution is circumvented by introducing the condition of minimal (in the sense of the mean squares) tangential field component at the surface Σ. Owing to this requirement, an almost continuous transition from the quasi-dipolar configuration to the tail-like one is obtained in the model, as shown in Figure 13.

The basic principle for constructing the tail magnetic configuration in this model has much in common with the stretching method designed by Voigt (1981) and Stern (1987). Anticipating its outline given in the next section, it is worth noting here that the magnetotail structure obtained by the stretching method is fully determined by the field distribution in the near magnetosphere, while in the present approach an interaction

between the two domains is implied. Indeed, due to the presence of the second term in (39) the near-magnetospheric field in the region S is also subjected to a modification, in order to respond to a 'capture' of a portion of the magnetic flux into the tail lobes. It should be noted also that an uncontrolled variation of $\mathbf{B}_n$ over the partition surface Σ leads to an enormous latitudinal spreading of the current density in the magnetotail, in contrast to the observed comparatively thin current sheet with sharp boundaries.

2.3. Modeling the Contribution from the Intramagnetospheric Currents

The above described representations of the boundary magnetic field are based on a conceptually clear physical model, which makes it possible to reduce to a minimum the number of empirically specified quantities. At least for the near magnetosphere, the effect of the Chapman–Ferraro currents can be evaluated more or less uniquely, once the solar wind momentum flux is given.

The situation is much more difficult in respect of the other extraterrestrial current systems because their existence is related to the penetration of the solar wind particles and fields into the magnetosphere. In comparison with the fundamental effect of the dipolar field confinement, these processes constitute a much more complex and intricate combination of phenomena including the IMF-related events and substorms. It should thus be realized that the development of a unified quantitative physical model based on given input data on the solar wind state is quite a formidable problem which is unlikely to be solved in the nearest future. A number of questions remains unanswered at present on the level of a qualitative understanding of basic mechanisms for formation of the tail plasma sheet, the field-aligned currents, and partly the ring current. For these reasons, empirical or semi-empirical approaches to modeling these current systems are mainly adopted in practical magnetispheric studies.

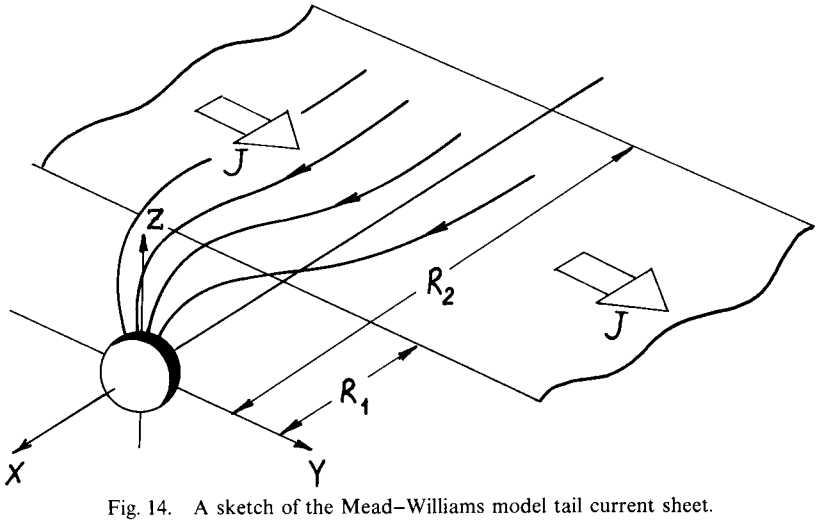

Fig. 14. A sketch of the Mead–Williams model tail current sheet.

2.3.1. *Magnetotail Current Sheet*

One of the first models for the magnetotail current system was proposed by Williams and Mead (1965), who simulated the stretched magnetic configuration at the nightside by placing an infinitely thin current sheet in the equatorial plane. As shown in Figure 14, the current sheet extends to infinity in the dawn-dusk direction, but has a finite width along the tail with its near and other edges being located at distances R_1 and R_2 from the geodipole, respectively. The current intensity J is assumed to be independent of x, in which case the magnetic field components in the GSM coordinates are

$$B_x = (B_T/\pi)\left[\tan^{-1}\frac{x+R_2}{z} - \tan^{-1}\frac{x+R_1}{z}\right],$$

$$B_y = 0\,, \tag{40}$$

$$B_z = (B_T/2\pi)\ln\frac{(x+R_2)^2+z^2}{(x+R_1)^2+z^2}\,,$$

where the parameter $B_T = 2\pi J/c$ defines the tail field magnitude. The tail field representation given by (40) was superposed on the model by Mead (1964) for the boundary field and provided a good basis for interpretation of data on the local time distribution of trapped fluxes. Roederer (1969) gave an instructive example of using this model as a tool for a quantitative synoptic patrol of the magnetospheric asymmetry based on data from the geosynchronous magnetic field measurements. However, the model is rather crude, contains unrealistic singularities and kinks of the magnetic field lines in the tail equatorial plane, and hence can be used only within a limited near-Earth region.

In later works many attempts were made to develop an improved representation of the tail magnetic field. Willis and Pratt (1972), Sugiura and Poros (1973), Olson and Pfitzer (1974), and Tsyganenko (1975) incorporated finite thickness of the current sheet and variation of the current density along the tail; they also took into account a finite dimension of the tail current in the dawn-dusk direction by having replaced infinitely long 'wires' with closed loops. A significant advance was made by Olson and Pfitzer (1977) and Tsyganenko (1976, 1981), who included in their models a tilt-dependent deformation of the tail current sheet. Figure 15 shows the ensemble of current loops designed by Olson and Pfitzer (1977) for numerical calculations of the model magnetic field. The current streamlines in this plot are symmetrical with respect to the equatorial plane and correspond to zero dipole tilt. In case of a non-zero ψ the ring current loops near the Earth rotate together with the dipolar equatorial plane, while at larger distances the tilt effects are simulated by a displacement of the tail current in the z-direction. A direct integration over the electric current systems similar to that shown in Figure 15 yielded magnetic field distributions which were then used for fitting coefficients of model expansions (Olson and Pfitzer, 1977) or were incorporated in numerical interpolation codes (Tsyganenko, 1976, 1981).

A more detailed description of these models and their comparative analysis can be found in the review papers by Walker (1976, 1979). It should be stressed here, as a

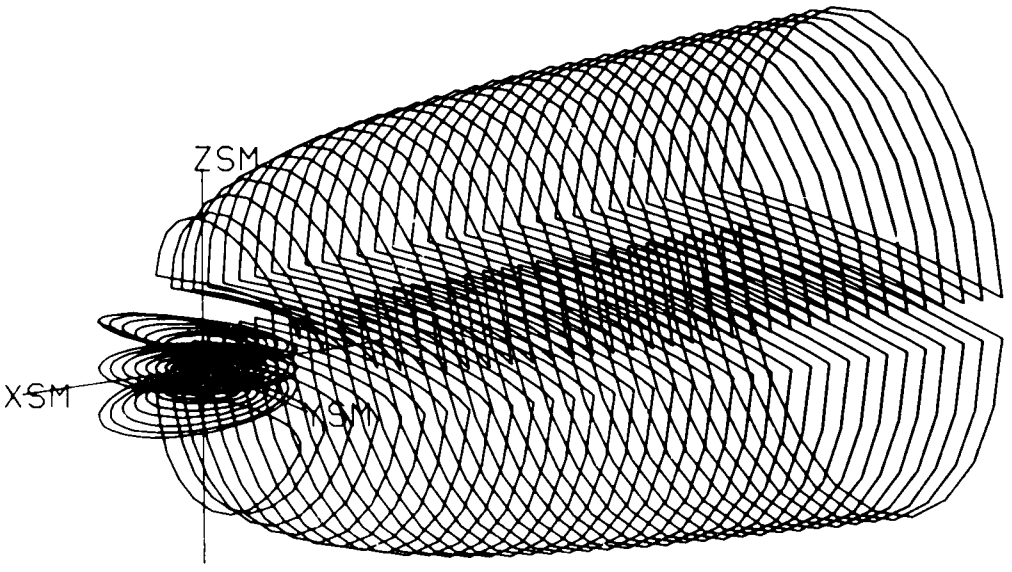

Fig. 15. 'Wire' model simulating the magnetotail and the ring current systems designed by Olson and Pfitzer (after Walker, 1979).

general remark to all the earlier studies based on integration over a prescribed current distributions (the so-called 'wire models'), that the possibilities of this approach are rather limited because it provides a solution of the direct problem. Since in spacecraft experiments we measure the magnetic fields, rather than electric currents, a solution of the inverse problem (that is a determination of the current system parameters on the basis of magnetic field data) is actually of greatest interest.

Characteristic features inherent to the inverse problem approach determine the main requirements imposed on mathematical representation of the model magnetic field. First of them is a sufficient flexibility of the model defined by the number of independent free parameters which can be least squares fitted to the experimental data. The point here is that, as a rule, we have little *a priori* knowledge on the configuration of currents and, hence, an over-simplification of the mathematical model can lead to a considerable loss of information potentially present in the experimental datasets. On the other hand, a comparatively high level of random noise in the datasets imposes an upper limit on the reasonable number of the degrees of freedom, beyond which we are faced with difficulties typical to ill-posed inverse problems. At last, it is also important that with relatively large amounts of data and limited computer resources a necessary condition for an inverse problem to be practically feasible is that the model be represented by comparatively simple analytical expressions. In reality the current systems are spread-out in space and the streamlines are curved and, hence, a direct evaluation of the Biot–Savart integral cannot be performed analytically with the result in a form of relatively compact formulas. This brings forth an additional task to develop methods for representation of magnetic fields corresponding to distributed current systems of

required geometry. (It is very much to the point noting here that David Stern did have good reasons to begin his review (1987b) by stating that 'Magnetospheric modeling is the art...'). Some of existing approaches to this problem will be discussed below.

Perhaps the most simple model was proposed by Mead and Fairfield (1975), who suggested to describe the contribution from all the extraterrestrial sources including the distributed currents in the magnetospheric plasma and the magnetopause current by a single set of analytical expressions containing the quadratic polynomials of solar-magnetic coordinates and a linear dependence on the geodipole tilt angle

$$\begin{aligned} B_x &= a_1 z + a_2 xz + \psi(a_3 + a_4 x + a_5 x^2 + a_6 y^2 + a_7 z^2)\,, \\ B_y &= b_1 yz + \psi(b_2 y + b_3 xy)\,, \\ B_z &= c_1 + c_2 x + c_3 x^2 + c_4 y^2 + c_5 z^2 + \psi(c_6 z + c_7 xz)\,. \end{aligned} \tag{41}$$

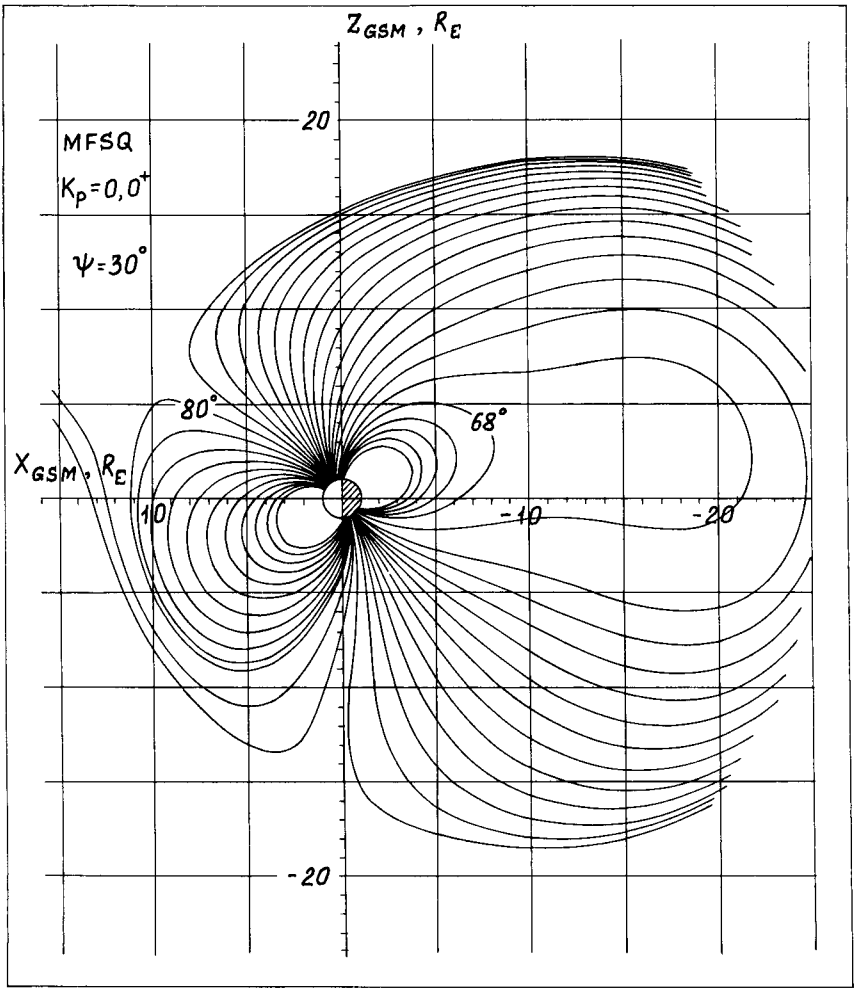

Due to the condition $\nabla \cdot \mathbf{B} = 0$, three additional constraints are imposed on the coefficients

$$a_2 + b_1 + 2c_5 = 0\,; \qquad a_4 + b_2 + c_6 = 0\,; \qquad 2a_5 + b_3 + c_7 = 0\,. \tag{42}$$

Thus, the model contains 14 free parameters, whose values were computed by a least squares fitting of (41) to the experimental data obtained from the IMP spacecraft measurements and sorted out into four subsets in accordance with the K_p-index values. Figures 16(a) and 16(b) show the magnetic field line plots corresponding to two extremal cases with respect to the disturbance level.

Putting aside a detailed discussion of the model field configurations and referring the

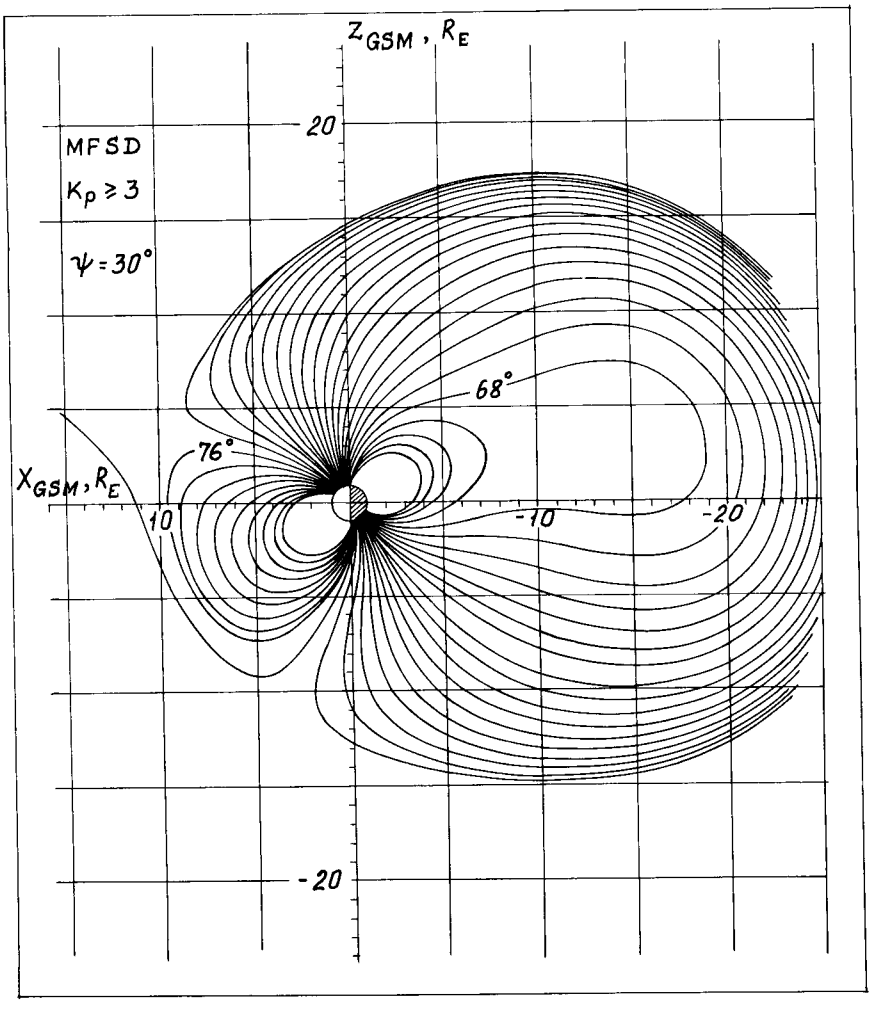

◀▲ Fig. 16a–b. Magnetic field configurations in the noon–midnight meridian plotted by using the model of Mead and Fairfield (1975) for nearly the largest value of the geodipole tilt $\psi = 30°$. (a) Superquiet model for $K_0 = 0, 0^+$. (b) Superdisturbed model for $K_p \geq 3$.

reader to the original papers (Fairfield and Mead, 1975; see also a review by Walker, 1976), we note that the representation (41) does not reproduce the sheet-like structure of the tail current. The volume current density obtained by taking the curl of the model field grows linearly with the distance from z-axis and does not incorporate any dependence on z (for $\psi = 0$). The corresponding current streamlines are ellipses encircling the Earth in westward direction. The model is very simple and reflects only the most general features of the real magnetosphere, due to a purely formal approach to the choice of the modeling functions.

Another example of models of this kind is the one proposed by Kosik (1984), in which the field distribution is represented by the sum of toroidal and poloidal terms

$$\mathbf{B} = \nabla \times (F_1 \mathbf{R}) + \nabla \times \nabla \times (F_2 \mathbf{R}), \tag{43}$$

where the scalar functions F_1 and F_2 are expanded in spherical harmonic series

$$\begin{aligned} F_1 &= \sum_{l,m} T_l(R) P_l^m(\cos\theta)(a_{lm}\cos m\varphi + b_{lm}\sin m\varphi), \\ F_2 &= \sum_{l,m} S_l(R) P_l^m(\cos\theta)(c_{lm}\cos m\varphi + d_{lm}\sin m\varphi). \end{aligned} \tag{44}$$

The model is able to represent a wide variety of magnetic field distributions by means of a proper choice of the radial functions T_1 and S_1 and the coefficients $a_{lm} - d_{lm}$ in (44). Kosik (1984) gave two examples of specific magnetic field models: an axisymmetric one simulating the effect of a ring current and a more sophisticated model taking into account the noon–midnight asymmetry. The functions T_1 and S_1 were chosen as combinations of exponential and power terms and the coefficients were fitted so that to obtain a close resemblance of the model distribution of the scalar quantity $\Delta B = |\mathbf{B}_d + \mathbf{B}| - |\mathbf{B}_d|$ with that deduced in the experimental study by Sugiura and Poros (1973) and with the model results by Olson and Pfitzer (1974).

The representation (43) was discussed in a review paper by Stern (1976), who showed in particular that the simplest polynomial approximation (41) of the Mead–Fairfield model can be easily obtained from the sum of poloidal and toroidal fields by a proper choice of the scalar functions. A very serious drawback of the method stems from the formal approach to postulating the functional forms (44) whose terms have no clear physical interpretation. In particular, the operation of double differentiation in (43) leads to very complex and uncontrolled relationships between the details of behaviour of the function F_2 and the resultant current density distribution obtained by applying one more differential operation to the field (43). The situation becomes even more complicated in taking into account the effects of the geodipole tilt, because formal modifications inserted in the model functions, again, have no conceptually clear interpretation in terms of the current streamline geometry.

Beard (1979) developed a model of the tail-current system, which is accurate enough in simulating its main geometrical features. The basic method is as follows. First, a numerical integration was performed over a 'wire' model of the planar current sheet closed via a semi-circular loop lying on a cylindrical magnetopause surface (Siscoe,

1966). As a result of the integration, a distribution of A_y and A_z components of the vector potential was found in several tail cross sections, on having assumed initially the current sheet to be infinitely thin, with a power dependence of the current density upon the tailward distance x, namely, $J \sim x^{-0.3}$ (Behannon, 1968, 1970). The results were used for constructing a polynomial representation for A_y and A_z versus y and z, with a subsequent determination of the best fit factor $f(x)$ approximating the variation of the potential along the x-axis. Some modification of the z-dependence was also incorporated, to take into account the finite thickness of the current sheet. The resultant magnetic field components calculated as $\nabla \times \mathbf{A}$ were shown to have the required distribution in three dimensions and were expressed by means of sufficiently simple analytic formulae. The model is capable of varying the total intensity of the field as well as its tailward gradient, current sheet thickness, and its inner edge location. An approximate account of the dipole tilt effects is possible also by introducing a displacement of the whole system in the z-direction, like in some other models (e.g., Alekseev and Shabansky, 1972; Tsyganenko and Usmanov, 1982; Tsyganenko, 1987).

The largest deviations of this model from the real average field should be expected near the inner edge of the current sheet. A typically observed feature in this region is a gradual transition from the dawn-dusk plasma sheet current to the ring current distribution which also tends to concentrate near the equatorial plane into a disc-like structure (Sugiura, 1972). This fact is manifested in a comparatively large values of B_y measured outside the plasma sheet in dawn and dusk sectors (Speiser and Ness, 1967; Fairfield *et al.*, 1987). However, the central current sheet in the Beard's model contains initially the y-component of the current only, and the subsequent modifications of the vector potential do not change the situation, since they do not violate the assumption $A_x = 0$ and, hence, $j_x = 0$, as before.

Tsyganenko and Usmanov (1982) developed a simple model of the current sheet of finite thickness, having started from a simplest representation for an infinitely long spread-out current element. This allowed to circumvent the difficulty with singularities inherent to infinitely thin wires. More explicitly, instead of the double integration over a two-dimensional continuum of wires providing each a contribution

$$\mathrm{d}\mathbf{B} = \frac{2\,\mathrm{d}J}{c\rho}\,\mathbf{e}_\varphi,$$

the ordinary integration over a one-dimensional distribution of a spread-out current elements yielding each

$$\mathrm{d}\mathbf{B} = \frac{2\,\mathrm{d}J\rho}{c(\rho^2 + D^2)}\,\mathbf{e}_\varphi$$

was performed, as shown in Figure 17. The magnetic field from the separate element grows linearly with the distance from its axis for $\rho \ll D$ and decreases as $\sim\rho^{-1}$ in the limit $\rho \gg D$, which corresponds to approximately constant volume current density near the centre of the filament and to an almost vacuum field at large distances. The main

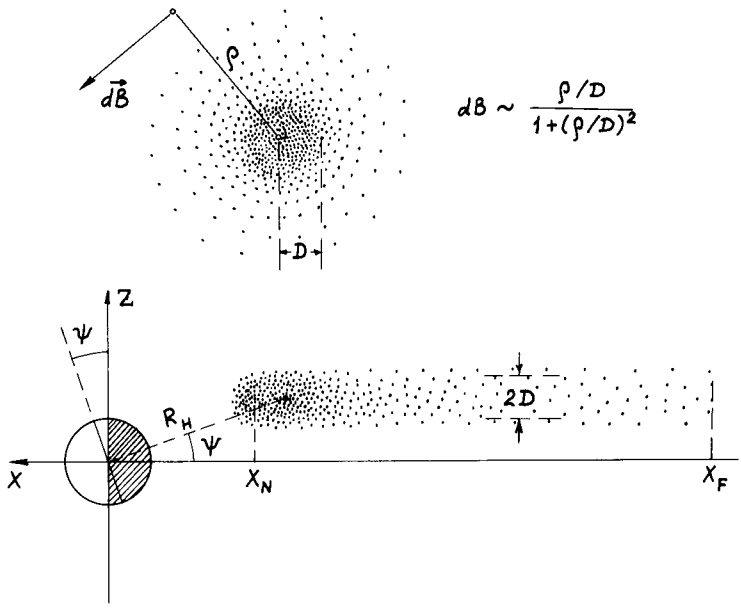

Fig. 17. A schematic view of a spread-out model current filament and a 'diffuse' current sheet with a spatially-varying current density, proposed by Tsyganenko and Usmanov (1982).

part of the current is contained within $\rho \lesssim D$, while at $\rho > D$ the current density rapidly goes to zero. To obtain the current sheet, it is enough to construct a continuous distribution of such spreadout current elements along the X-axis, as shown in Figure 17. Specifying the current distribution along the tail axis by means of the function

$$J(x) = (c/2\pi)B_T(x)\,,$$

we obtain the components of the field produced by the sheet as

$$B_x(x, z) = \frac{z}{\pi}\int_{x_F}^{x_N} B_T(x')\,\frac{\mathrm{d}x'}{(x' - x)^2 + z^2 + D^2}\,,$$

$$B_z(x, z) = \frac{1}{\pi}\int_{x_F}^{x_N} B_T(x')\,\frac{(x' - x)\,\mathrm{d}x'}{(x - x')^2 + z^2 + D^2}\,, \tag{45}$$

where the limits x_N and x_F define the locations of its inner and outer edges, respectively. A choice of the function $B_T(x)$ is defined by the extension of the modeling region. Tsyganenko and Usmanov (1982) employed spacecraft data obtained within a relatively limited range of distance $R \lesssim 20\ R_E$. For this reason, the function B_T in that model was approximated by the linear dependence

$$B_T(x) = B_N + \Delta B(x - x_N)/S\,. \tag{46}$$

Later on a more extended dataset was generated containing also the measurements taken in the distant tail region $-70\,R_E \lesssim x_{GSM} \lesssim -15\,R_E$. Since the magnetic field gradient in the near tail is much larger than at lunar distances, the linear approximation (46) is too crude for modeling the entire cislunar tail current distribution. From these considerations, in the later version of the model (Tsyganenko, 1987) a more flexible representation for $B_T(x)$ was chosen as

$$B_T(x) = B_0 + B_1/(x - x_1) + B_2/(x - x_2)^2\,, \tag{47}$$

which includes three linear and two nonlinear parameters.

The major convenience of this approach consists in that integrating the distributions (46)–(47) in (45) yields relatively simple and flexible analytic expressions which do not contain any singularities or discontinuities and include a parametric dependence on several quantities having a clear physical meaning.

These models, however, have a fundamental drawback which stems from the absence of the B_y-component and corresponds, in fact, to the rectilinear geometry of the initial current elements. In the near tail region this evokes the same difficulties as those inherent to the Beard's model. In an attempt to account for a limited dawn-dusk extension of the magnetosphere and a curvilinear shape of the current streamlines in the near tail, Tsyganenko and Usmanov (1982) and Tsyganenko (1987) multiplied both components (45) of the magnetic field by an even function $f(y)$ which falls off to zero for $y \to \pm\infty$ with a scale length $\Delta y \sim 15\,R_E$. This modification does not violate the $\nabla \cdot \mathbf{B} = 0$ condition and changes the current flow line geometry in such a way that it acquires a resemblance with the observed one. However, the condition $B_y = 0$ remains unchanged, which does not allow to extend the sheet-like structure in the dawn and dusk sectors.

Apart from this deficiency, there exist one more difficulty related to the deformation of the current sheet due to the tilting of the geodipole axis. Statistical studies of the average shape and position of the tail neutral sheet (Russell and Brody, 1967; Fairfield, 1980; Gosling *et al.*, 1986; Dandouras, 1988) as well as theoretical considerations (Voigt, 1984) inferred the existence of a two-dimensional warping of the sheet roughly proportional to the dipole tilt angle ψ. Near the midnight meridian plane the warping results in a gradual departure of the neutral sheet from the dipole equatorial plane towards that parallel to the solar wind stream. This is accompanied by a bending of the sheet in the YZ projection in such a way that, for $\psi > 0$, it is raised above the GSM equatorial plane near the midnight meridian, but descends below this plane near the tail flanks, the displacements being the reverse for $\psi < 0$. In a recent work of Dandouras (1988) this effect has been studied extensively in the region $-20\,R_E \lesssim x_{GSM} \lesssim -7\,R_E$ using the ISEE-1 spacecraft data. The detailed investigation has shown that, in fact, the warped neutral sheet crosses the GSM equatorial plane in a close proximity to the magnetopause.

In the above discussed models only a gross simulation of the tilt-related effects was done by assuming a purely translational shift of the whole planar current sheet in the z_{GSM} direction by $\Delta z = R_H \sin\psi$, with the parameter R_H defining the 'hinging distance'. Apparently, the largest discrepancies due to inaccuracy of this assumption should be

expected to arise in the pre-dawn and post-dusk sectors near the flanks of the tail. As a consequence, a significant overestimate of the sheet thickness as well as an underestimate of the current magnitude can be present in these models.

In view of these considerations, it was decided to abandon the representation (45)–(47) in favour of a quite different approach based on a modification of appropriate vector potential. As a starting point for this work (Tsyganenko, 1989a), a simple model of an infinitely thin equatorial current disc giving a proper radial distribution of $\mathbf{B}_z$ was developed. Due to axial symmetry, we introduce a cylindrical coordinate system (ρ, φ, z) co-axial with the dipole and assume the vector potential to have only one component $\mathbf{A} = \{0, A, 0\}$. The absence of currents in the whole space outside the equatorial plane leads to equation $\nabla \times \nabla \times \mathbf{A} = 0$ whose solution is obtained by separating the variables as

$$A(\rho, z) = \int_0^\infty C(K)\, e^{-K|z|}\, J_1(K\rho) K^{1/2}\, \mathrm{d}K\,. \tag{48}$$

The boundary condition can be defined by specifying the radial distribution of $B_z = B_z(\rho)$ in the equatorial plane. Inverting the corresponding integral by means of Bessel transform, one obtains the weight function

$$KC(K) = \int_0^\infty \rho^{1/2} B_z(\rho)\, (K\rho)^{1/2} J_0(K\rho)\, \mathrm{d}\rho\,. \tag{49}$$

The simplest explicit solution can be derived by choosing the distribution $B_z(\rho)$ as

$$B_z(\rho) \sim (a^2 + \rho^2)^{-1/2}\,.$$

Being inserted in (49), this yields the function $C(K)$ which, on substitution in (48), determines the explicit solution for the vector potential in the whole space as

$$A^{(1)}(\rho, z) \sim \rho^{-1}\{[(a + |z|)^2 + \rho^2]^{1/2} - (a + |z|)\}\,. \tag{50}$$

Taking derivatives of (50) with respect to the parameter a, one obtains a set of independent solutions corresponding to a progressively larger rates of decrease of B_z and the current density by $\rho \to \infty$. For our purpose it is enough to take the first and the second derivatives, which yield

$$A^{(2)}(\rho, z) = \frac{\partial A^{(1)}}{\partial a} \sim \rho^{-1}\left\{1 - \frac{a + |z|}{[(a + |z|)^2 + \rho^2]^{1/2}}\right\} \tag{51}$$

and

$$A^{(3)}(\rho, z) = \frac{\partial A^{(2)}}{\partial a} \sim \rho[(a + |z|)^2 + \rho^2]^{-3/2}\,. \tag{52}$$

The next step is to modify the obtained vector potentials. As can be easily verified, replacing $|z|$ by $(z^2 + D^2)^{1/2}$ in (50)–(52) converts the infinitely thin current discs into

spread-out ones with a characteristic half-thickness scale D which can be assumed to vary in two dimensions throughout the equatorial plane. Replacing then z by $z' = z - z_s(x, y, \psi)$, we incorporate the effects of warping the current sheet. Its shape is defined by the function z_s which contains the dipole tilt angle as a parameter. At last, to take into account the day–night asymmetry of the tail current and its finite dimension in the dawn-dusk direction, an appropriate truncation factor $W(x, y)$ can be introduced.

These modifications, however, are based on formal considerations, rather than on the direct problem solution derived from an explicitly specified current system of given geometry. Hence, a verification of the obtained current distribution by computing $j = (c/4\pi)\nabla \times \nabla \times \mathbf{A}$ is necessary. Figure 18 shows a view of the current streamline

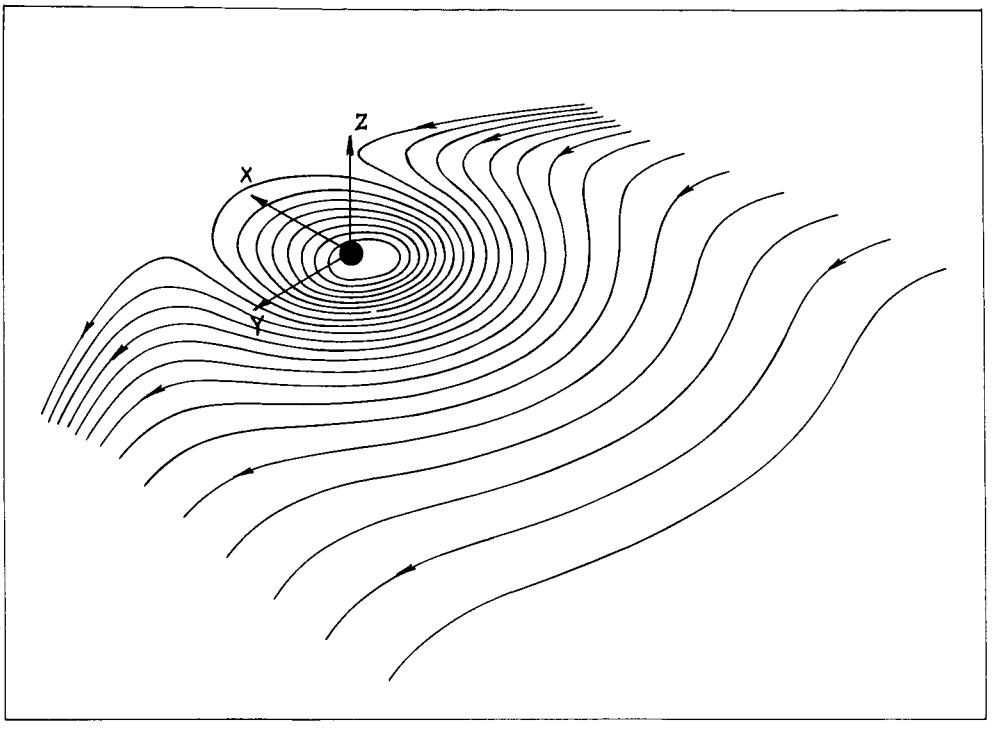

Fig. 18. Three-dimensional view of the current flow line pattern in the equatorial plane plotted by using the model of Tsyganenko (1989a) for $\psi = 0$.

geometry obtained in the equatorial plane for $\psi = 0$. A clearly seen continuous transition from the tail-current sheet to the ring current is a consequence of the adopted mathematical model, in which both sources are represented by the sum of modified vector potentials (50)–(52) having a similar structure. Figure 19 (Tsyganenko, 1989a) displays a family of the contours of constant j_y in the noon–midnight meridian plane of the model magnetosphere with the geodipole tilt angle close to its maximal value. The plot clearly demonstrates the expected warping of the tail current sheet near

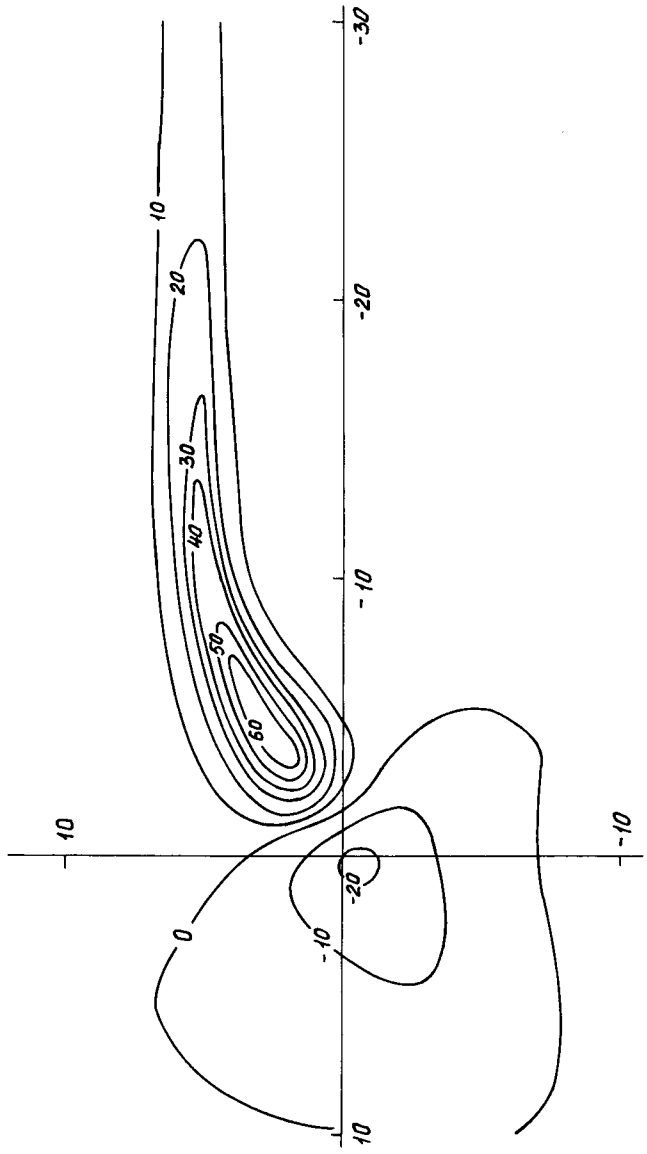

Fig. 19. A family of contours j_y = constant in the noon–midnight meridian plane obtained for the geodipole tilt angle $\psi \approx 35°$ using the model of Tsyganenko (1989a) for $K_p = 4^-, 4, 4^+$. The isolines are labeled in units 10^{-10} A m^{-2}. Note the warping of the current sheet and a significant day–night asymmetry.

$x_{GSM} \sim -10\,R_E$. Figure 20 shows a family of the current streamlines crossing the midnight meridian plane at $x_{GSM} = -15\,R_E$, in projection onto a plane perpendicular to the x-axis. The pattern corresponds to nearly the same value of $\psi = 35°$; the neutral sheet configuration according to Dandouras' (1988) results is shown by crosses for comparison. A good correspondence of the model with the observed geometrical properties of the neutral sheet is evident from these plots.

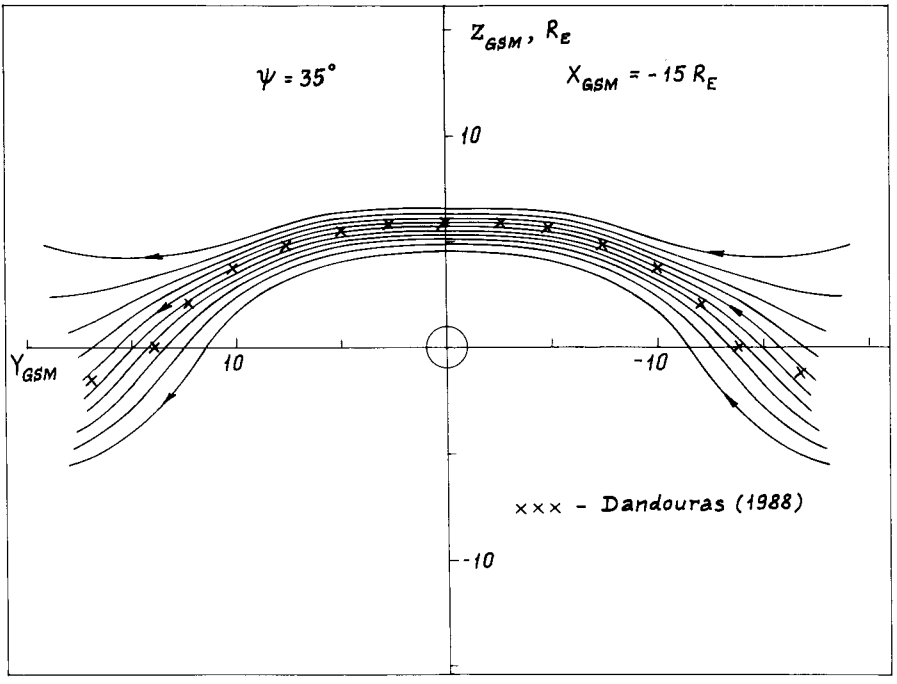

Fig. 20. Current streamlines crossing the midnight meridian at $X_{GSM} = -15\,R_E$ shown in the $Y - Z$ projection. The plot demonstrates the effect of the current sheet flexing due to the geodipole tilt in the model of Tsyganenko (1989a). The upper and lower streamlines indicate roughly the half of the maximum current density. The crosses mark the average observed neutral sheet position as deduced by Dandouras (1988) from the ISEE-1 spacecraft data.

If the tailward extension of the modeling region exceeds 10–15 R_E, an account of the closure currents flowing at the high-latitude magnetopause is necessary, because otherwise it is impossible to obtain correct distribution of both B_x and B_z components along the tail.

A completely different approach to modeling the stretched magnetic fields typical for the tail region was suggested by Voigt (1981). Instead of specifying more or less sophisticated current distributions in an explicit form, a formal transformation of the initial vacuum magnetic field components leading to tail-like configurations was proposed in that work. A solution for the dipolar field confined within a composite cavity shown in Figure 11 was chosen as the initial field configuration subjected to the stretching.

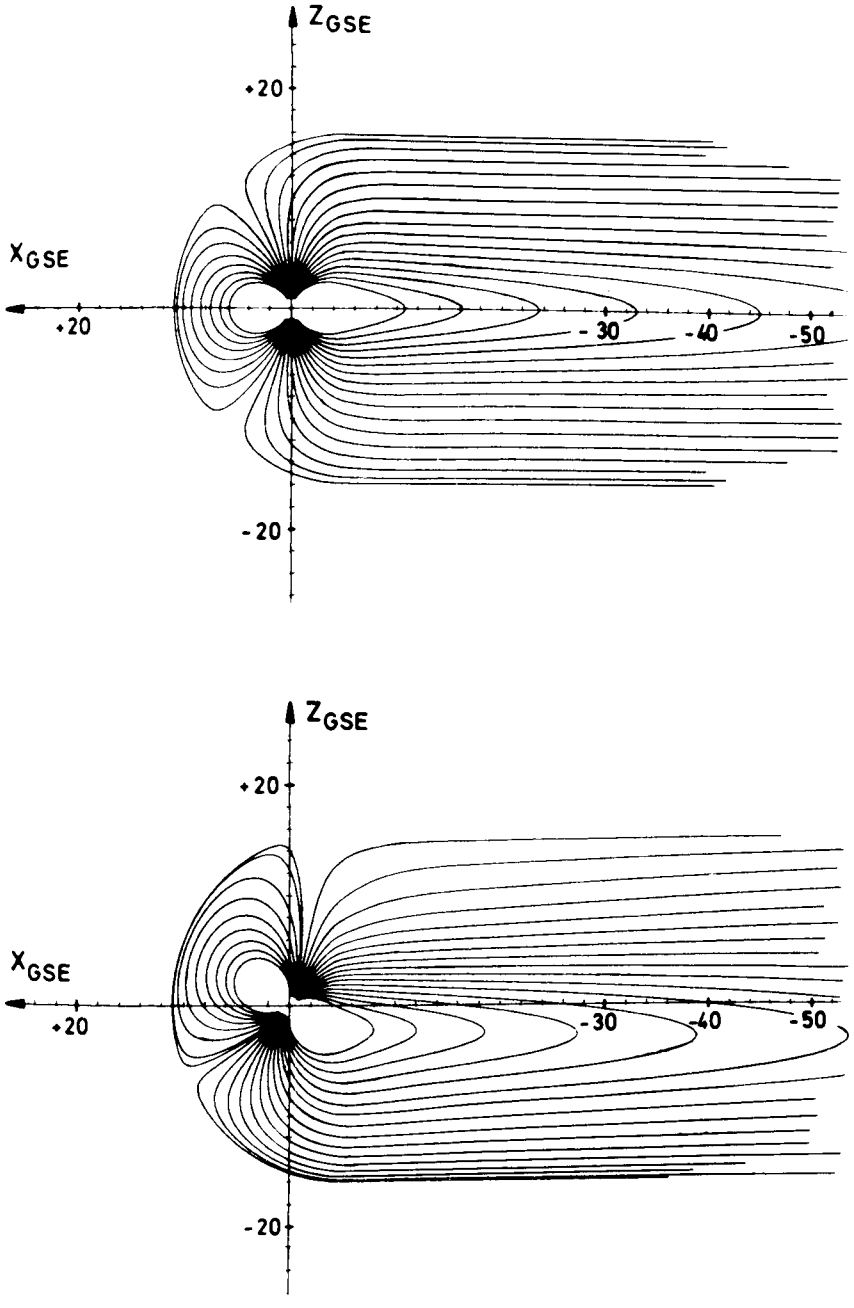

Fig. 21. Field line configuration in the model of Voigt (1981). The tail magnetic structure is obtained by means of a stretch transformation (53) applied to the vacuum field confined within the cylindrical tail boundary. The dipole tilt effects ($\psi = -35°$) are shown in the bottom plot (see also Figure 22).

Denote the total field (the dipolar one plus the boundary current contribution) in the tail region as $\mathbf{B}_v(x, y, z) = \nabla U$. The proposed transformation consists in replacing it by a 'stretched' one, $\mathbf{B}'$, with components

$$\begin{aligned} B'_x(x, y, z) &= B_{vx}(\lambda(x - x_0) + x_0, y, z), \\ B'_y(x, y, z) &= \lambda B_{vy}(\lambda(x - x_0) + x_0, y, z), \\ B'_z(x, y, z) &= \lambda B_{vz}(\lambda(x - x_0) + x_0, y, z), \end{aligned} \tag{53}$$

where λ is the transformation parameter taking the values in the interval $0 \leq \lambda \leq 1$. The upper limit $\lambda = 1$ corresponds to the identity transformation, while $\lambda = 0$ provides the maximal stretching with vanishing transverse components of $\mathbf{B}'$ and $\partial B'_x/\partial x = 0$. One can easily verify that the transformation (53) does not violate the $\nabla \cdot \mathbf{B} = 0$ condition. It is essential to note that, due to the matching conditions imposed at the plane $x = x_0$, the vacuum field $\mathbf{B}_v$ and, hence, the stretched field in the tail are related to the dayside magnetic field distribution defined by the magnetopause position which, in turn, depends upon the solar wind pressure and the geodipole tilt angle. As can be seen from Figure 21, the model provides a good agreement of the field line structure with the observed one, at least visually. At the first glance, this is a formal consequence of the adopted method of the tail field reversal region is controlled by the distribution of B_{vx} near the plane $x = x_0$ which, in its turn, is defined mainly by the geodipole tilt. However, the most notable feature of the Voigt's (1981) model concerns the transverse structure of the magnetotail field. Figure 22 displays the current streamlines computed in the tail cross-section at $x_{GSM} = -35\ R_E$ for $\psi = 0$ and $\psi = 35°$. It can be seen that the current sheet thickness is minimal near the midnight meridian. The most interesting effect here is the flexing of the current sheet for $\psi \neq 0$. The obtained configuration is in excellent accord with the above discussed experimental and model results (see Figure 20).

In his later paper Voigt (1984) gave an interpretation of these results on the basis of magnetohydrostatic approach. Namely, a class of magnetic field models for the tail region has been considered, which allows to represent the components in the following separable form

$$\begin{aligned} B_\rho &= (\alpha/\alpha_0)\Omega'(\rho)\cos\varphi\, f_2(z), \\ B_\varphi &= -(\alpha/\alpha_0)\Omega(\rho)/\rho \sin\varphi\, f_2(z), \\ B_z &= \Omega(\rho)\cos\varphi\, f'_2(z), \end{aligned} \tag{54}$$

where, in accordance with the assumed cylindrical magnetopause shape, the z-axis is directed antisunward ($\mathbf{e}_z = -\mathbf{e}_{XGSM}$). Representation (54) has the property that for $\alpha = \alpha_0$ the field becomes curl-free; besides that, for any α we have $(\nabla \times \mathbf{B}) \cdot \mathbf{B} = 0$, that is no field-aligned currents are present in the model. Substitution of (54) in the equation $\nabla \cdot \mathbf{B} = 0$ leads to an eigenvalue problem whose solution can be written down as an expansion in eigenfunctions containing the exponential factors

$$f_2(z) = \exp(-\xi_i \sqrt{\alpha/\alpha_0}\, z), \tag{55}$$

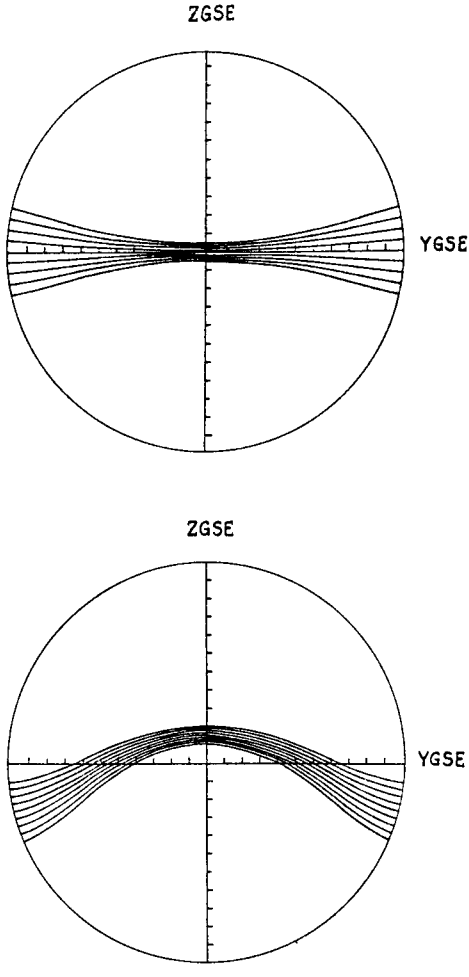

Fig. 22. Current streamlines at $X_{GSM} = -35\,R_E$ shown in the $Y-Z$ projection for $\psi = 0$ (*top*) and $\psi = 35°$ (*bottom*) in the model of Voigt (1981). Like in Figure 19, the upper and lower streamlines indicate the half of the maximal current density.

with ξ_i satisfying the equation $J_1'(\xi_i) = 0$. The constant α can be chosen arbitrarily in the range $0 \leq \alpha \leq \alpha_0$, so that in case $\alpha = 0$ the field lines are aligned parallel to the z-axis $\partial B_z/\partial z = 0$, while by $\alpha = \alpha_0$ the vacuum field is obtained, with a maximal rate of tailward decrease. From a formal point of view, this corresponds exactly to the stretching transformation (53) which, however, is now easily tractable in terms of magnetohydrostatic theory. This can be ascertained by a proper choice of the isotropic pressure distribution satisfying the stress balance equation at least in the direction transverse to the tail axis.

As indicated by Voigt's results, the model (54) is compatible in this sense with a simple pressure functions parameterized by the same constant α and eigenvalues ξ_i. It can be, therefore, concluded that the observed transverse warping of the tail-current empirically simulated in the model by Tsyganenko (1989a), as shown in Figure 10, and inherent to the Voigt's (1981) model as an implication of the stretching method (Figure 22) reflects a tendency of the real plasma sheet to remain in the state of magnetohydrostatic equilibrium with the lobe magnetic field.

On the other hand, the simplifying assumptions incorporated in the model of Voigt (1981, 1984) for the sake of mathematical tractability define also its main shortcomings. Thus, the tail magnetic field model implies zero component of the electric current density along the x_{GSM} axis. As already noted, this leads to inadequacies in modeling the near tail magnetic field structure. It should also be emphasized that the transformation (53) cannot model properly thin current sheets and does not contain an independent parameter for the sheet thickness. It is clear that a characteristic scale thickness of the current distribution corresponding to the stretched field is defined by the variation of the B_x-component in the z_{GSM} direction at the 'seam' plane $x = x_0$. Assuming the field to be approximately dipolar in this region, it is easy to assess that the variation scale is of the order of x_0, that is several Earth radii. At the same time, even statistically averaged observed values of the current sheet thickness in this region can be quite small (Hedgecock and Thomas, 1975; McComas *et al.*, 1986) and reach even smaller values of several tenths of R_E during disturbed periods (Lin and Barfield, 1984; Kaufmann, 1987). Besides that, the observed outer boundary of the plasma sheet is, as a rule, well pronounced and contains typically a layer of intense field-aligned currents (Ohtani *et al.*, 1988). A quantitative simulation of all these features in a single model can be performed as yet in the framework of empirical approach only.

The above discussed question on consistency of the model magnetic field configurations with the particle pressure distribution in the plasma sheet was studied in detail by several authors (Fuchs and Voigt, 1979; Voigt and Wolf, 1985; Hilmer and Voigt, 1987; Birn *et al.*, 1977; Birn, 1987). All these works are based on assumption of isotropic particle distribution, which allows to consider the pressure to be constant along the field lines. This largely simplifies mathematical treatment of quasi-static configurations, since in three-dimensional case the isotropic pressure can be considered as a function of two Euler potentials, $p = p(\alpha, \beta)$ with $\mathbf{B} = \nabla\alpha \times \nabla\beta$, while in two-dimensional models the equilibrium problem can be addressed in the framework of the Grad–Shafranov theory. In Section 3.2 this approach will be considered in relation to the question of interplanetary magnetic field effects in the observed and model magnetospheric structures. The reader is referred also to reviews by Voigt (1986), Schindler (1974, 1979), and Schindler and Birn (1986), for a more comprehensive treatment of the magnetohydrostatic models.

The formal method of stretch transformation introduced by Voigt (1981) for simulating the tail field was significantly generalized and developed by Stern (1987a). The main principle of the method is to find a transformation of an initial magnetic configuration, which provides a required final one and does not violate the $\nabla \cdot \mathbf{B} = 0$ condition. One of the simplest examples is the following one-dimensional Cartesian stretch. In this case

Cartesian components of the initial $\mathbf{B} = \mathbf{B}(x, y, z)$ are replaced by

$$B'_x = B_x(f(x), y, z) \equiv B^*_x(x, y, z),$$
$$B'_y = f'(x)B_y(f(x), y, z) \equiv f'(x)B^*_y(x, y, z), \tag{56}$$
$$B'_z = f'(x)B_z(f(x), y, z) \equiv f'(x)B^*_z(x, y, z).$$

The transformed field $\mathbf{B}'$ is also divergence free. By taking $f(x) = x$ we obtain the identity transformation, while $f(x) = \text{const.}$ yields $B'_y = B'_z = 0$ and $\partial B'_x/\partial x = 0$, i.e., maximal stretching leading to a two-dimensional final configuration. To model the observed nightside magnetospheric structure, we have to define $f(x)$ as a smooth function with a following asymptotic behaviour: $f(x) \simeq x$ for $x \gg x_0$ and $f(x) \sim x_0$ for $x \ll x_0$, where the coordinate x_0 marks the transition from the quasi-dipolar to the tail-like geometry. Figure 23 shows the dipole field confined within the ellipsoidal cavity and modified in the nightside sector in accordance with the transformation (56). The stretch function $f(x)$ in this example is similar to that used by Stern (1987a) for the paraboloid model (see Table 1 and Figure 3 in the paper by Stern). Its plot is shown in the bottom of Figure 23. The modification (53) of the vacuum field proposed by Voigt (1981) is actually a limiting case of (56) corresponding to an abrupt transition at $x = x_0$ from $f_1(x) = x$ to $f_2(x) = \lambda(x - x_0) + x_0$, as shown by the broken line. According to (56), the transversal field components acquire a small factor $f'(x)$ in the stretching region, which is clearly seen in Figure 23. The nightside field lines at $x \lesssim -5$ assume a rectilinear shape being parallel to the x-axis and the ellipsoidal magnetopause turns into a cylinder. A more realistic tail geometry with a gradual flaring of the magnetopause and diverging field lines can be obtained using a more general stretch applied to the ellipsoidal coordinate τ. Stern (1987a, b) gave a comprehensive description of the mathematical formalism necessary for extending the stretch transformation method to more general cases. In particular, the transformation in cylindrical and spherical coordinates were considered, which allow both radial and angular stretch. The first one corresponds to a poloidal deformation pertaining to the Earth's ring current or to the Jovian current disc, while the second one opens a possibility of empirical modeling solar magnetic configurations associated with the warped heliospheric current sheet or the 'spiked helmet' structures.

A further generalization of the method can be obtained by introducing a dependence of the stretch function on all the spatial coordinates. Thus, the function $f(x)$ in (56) can be replaced by $f(x, y, z)$. Then, using the same notations

$$\mathbf{B} = \mathbf{e}_x(B^*_x - f'_y B^*_y - f'_z B^*_z) + \mathbf{e}_y f'_x B^*_y + \mathbf{e}_z f'_x B^*_z .$$

Moreover, a simultaneous stretch in all three coordinates can be done in principle. The corresponding transformation is derived in a more cumbersome way and can be found in the original work (Stern, 1987a).

In view of a wide variety of possible initial configurations together with a number of relatively simple stretch transformations which can be superposed and combined in various sequence, this method should be considered as a very effective and promising

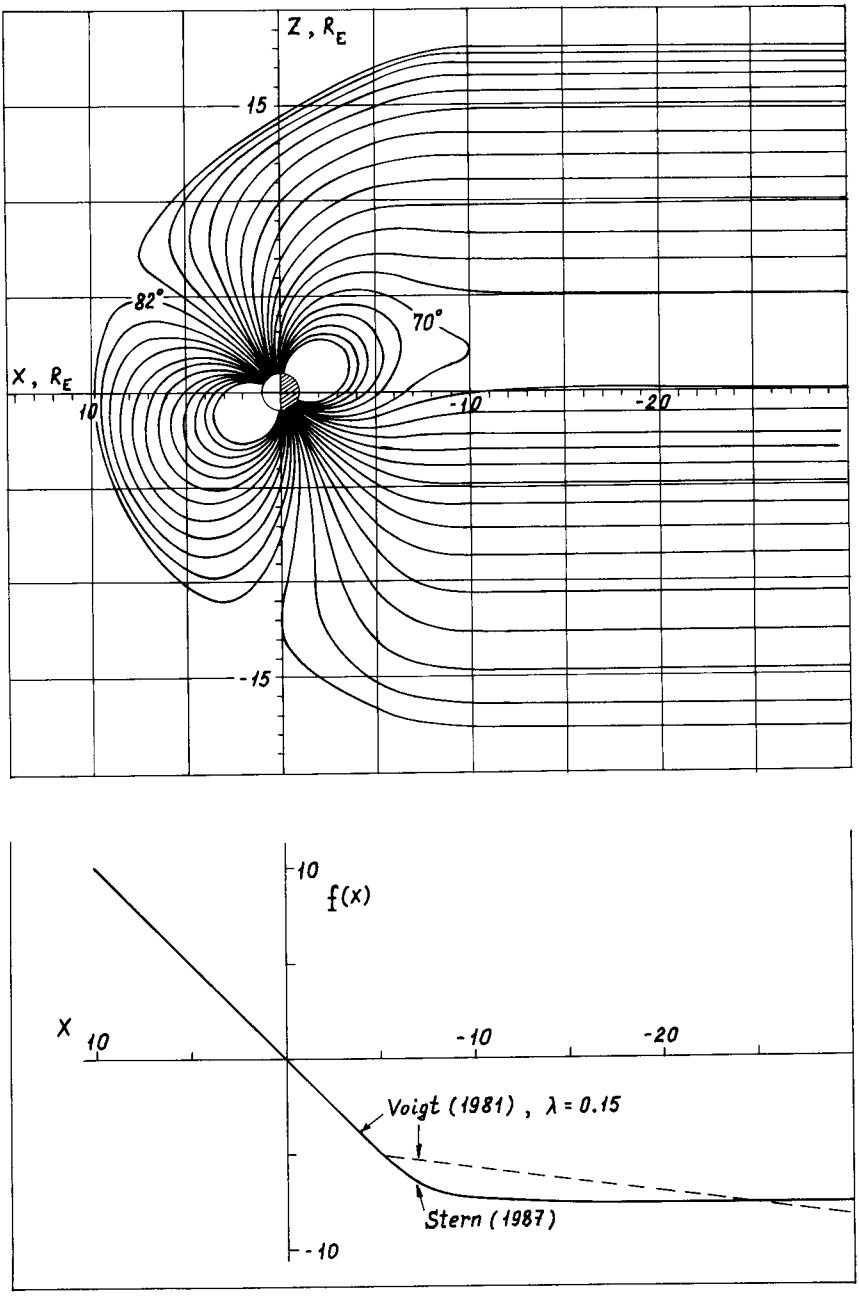

Fig. 23. Magnetic field lines in the ellipsoid model (Figure 10) subjected to the stretch transformation with the function $f(x)$ taken from the work of Stern (1987). The stretch function is plotted in the bottom on the same scale along the X-axis, the broken line corresponding to the Voigt's transformation (53).

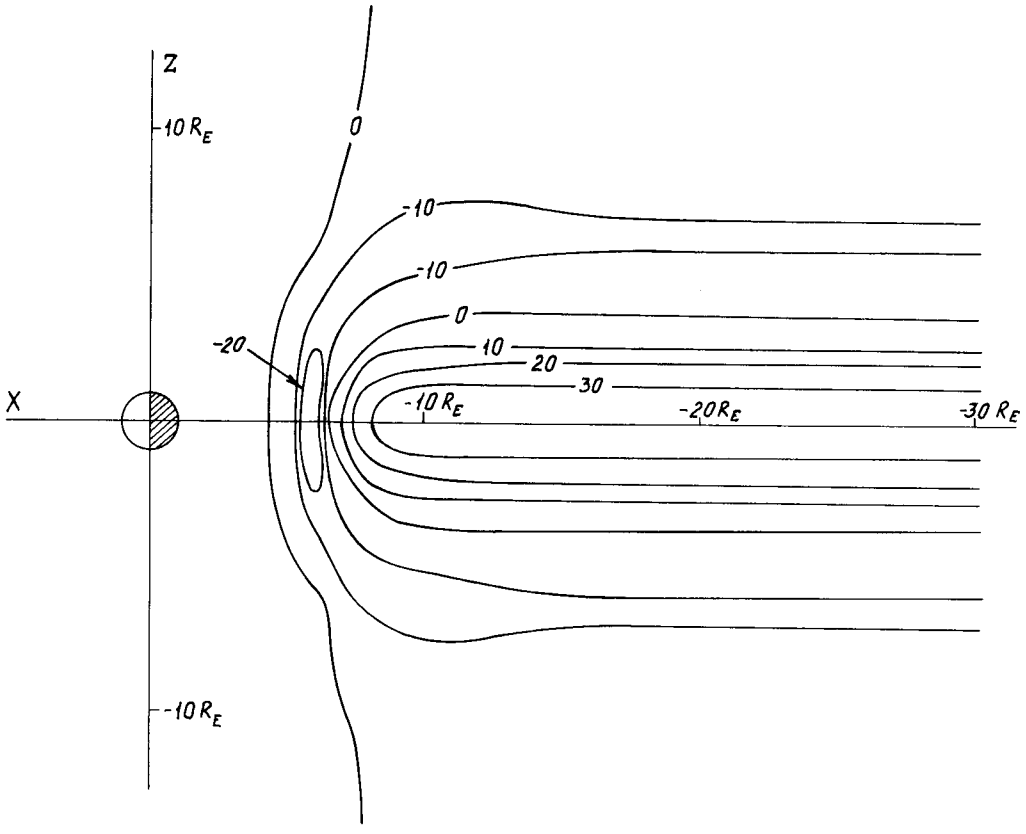

Fig. 24. A family of contours j_y = constant in the noon–midnight meridian plane corresponding to the stretched ellipsoid model field with the untilted dipole. The isolines are labeled in units 10^{-10} A m^{-2}.

tool for empirical modeling of magnetic fields in space. The only difficulty consists in a lack of control over the structure of currents associated with the deformed magnetic field, which was noted above in connection with Voigt's model. Figure 24 displays the distribution of the dawn-dusk component of the current density in the midnight meridian plane, corresponding to the stretched quasi-dipolar configuration shown in Figure 23. In spite of the fact that there is a visual correspondence between the model picture of the magnetic field lines and that implied by observations, the model currents in Figure 24 are seen to be distributed over the whole magnetotail domain. The region with positive values of j_y is approximately 8 R_E thick. Outside this layer the current is directed oppositely, i.e., from dusk to dawn, and its density decreases rather slowly away from the equatorial plane. A computation of the model current streamline geometry shows that a relatively intense current sheet does not extend in the dawn-dusk direction farther than 5–7 R_E from the $y = 0$ plane, due to its rapid closure via the lobe regions. A portion of the westward current near the inner edge of the central sheet closes through a narrow eastward current band located at $x \sim -6\ R_E$ and playing the role of a shielding source

which cancels the contribution from the tail current in the front magnetospheric region $x > -5\,R_E$ with vacuum magnetic field. Thus, the obtained structure of the model tail current differs significantly from the generally accepted one.

2.3.2. *Large-Scale Field-Aligned Current Systems*

For more than two decades after the experimental discovery of the field-aligned currents (Zmuda *et al.*, 1966; Zmuda and Armstrong, 1974; Iijima and Potemra, 1976), they remain to be the object of primary interest in the magnetospheric physics, owing to their outstanding role in the processes of the energy transfer from the solar wind to the ionosphere. A lack of understanding still exists as to what physical mechanisms are responsible for generation of the field-aligned currents (see the reviews by Roederer, 1977; Sato and Iijima, 1979; Troshichev, 1982; and Stern, 1983). Here again, we meet with both urgent and difficult task of an adequate account of these sources in quantitative magnetospheric models.

The importance of the latter problem stems from the estimate of the total electric current flowing in the main magnetospheric circuits. Indeed, the total Chapman–Ferraro current flowing at the dayside magnetopause between the polar cusps is of the order of $\sim 5 \times 10^6$ A. Nearly the same value can be obtained for the net tail current within the near-Earth region $-20 \lesssim x_{GSM} \lesssim -5\,R_E$. As for Birkeland current, according to evaluation by Bythrow and Potemra (1983) its total magnitude can also be typically a few million ampères. For extremal conditions this estimate may well be extrapolated to $\sim 10^7$ A. Therefore, a considerable influence of Birkeland currents upon the overall magnetospheric structure must be expected.

One of the main difficulties in quantitative modeling the magnetic field from Birkeland current systems lies in characteristic features of their geometry and in the absence of a definite scale length. In the remote magnetospheric regions adjacent to the boundary layer Birkeland currents should be distributed over a vast volume with a spatial scale size of tens of R_E, while at ionospheric heights their latitudinal and longitudinal transverse dimensions do not exceed a few hundreds and thousands of kilometres, respectively.

Besides that, there exist uncertainties in defining the configuration of model field-aligned currents at large geocentric distances, since no definite physical model for their sources is available as yet. However, owing to the expansion of the magnetic field line tubes with distance, the relative magnitude of the contribution from Birkeland currents falls off, while their spatial variation becomes large enough. Therefore, it can be expected that in the outer magnetosphere it is possible to simulate the magnetic effects by including relatively simple terms in the expressions for the total field components. Thus, Tsyganenko and Usmanov (1984) have shown that the averaged effects of Birkeland currents are discernible even in a rather simple empirical model.

In that work a local modeling of the dayside magnetic field was done based on the polynomial representation of the field from all the external sources. The corresponding expressions were similar to those used by Mead and Fairfield (1975), except that we added the cubic terms and used $\sin\psi$ instead of ψ. The coefficients were least squares

fitted to the IMP and HEOS spacecraft data taken within the dayside sector of solar magnetic longitudes $|\lambda_{SM}| \leq 60°$. Several sets of coefficients were found corresponding to a sequence of intervals of K_p- and AE-indices as well as for two opposite polarities of B_z- and B_y-components of the IMF.

A study of the obtained model magnetic structure showed that, in agreement with other works (Mead and Fairfield, 1975; Tsyganenko and Usmanov, 1982; Tsyganenko, 1987, 1989a), the increase of the activity is associated with the equatorward shift of the polar cusps and the Earthward displacement of the subsolar magnetopause. We also studied a configuration of the electric current system responsible for the re-distribution of the magnetic field. The components of $\nabla \times \mathbf{B}$ and the corresponding current streamlines were computed from the model field distribution. It was found that the dayside current forms a large-scale vortical structure, in which the lines descend from the high-latitude magnetopause towards the Earth in the dawn sector, cross the midday meridian plane and ascend again towards the distant polar cusp region. Such a pattern can be interpreted as the high-latitude circuit of the large-scale system I of Birkeland currents, though strongly distorted and smoothed out due to spatial and temporal averaging inevitable in the model representation.

Tsyganenko and Usmanov (1984) also pointed out an interesting effect pertaining to the structure of the polar cusps in dependence on the geomagnetic disturbance indices. It was found that the increase of the disturbance level is associated with a progressively larger degree of longitudinal stretching of *ad hoc* defined contours delineating the polar cusp boundary in the ionosphere. The boundaries were obtained by mapping along the model field lines the constant total B contours encircling the neutral points from the magnetopause vicinity up to the ionospheric height. In a sense, they can be interpreted as the isolines of precipitating flux of the polar cusp particles. This finding is in agreement with the observed expansion of the dayside polar cusps in the zonal direction deduced from auroral data (Zaitseva and Pudovkin, 1976).

The same inferences can be drawn from the results of Pudovkin *et al.* (1986), who studied some geometrical effects inherent to the field line mapping in the vicinity of the polar cusp using an idealized planar model of the dayside magnetopause. A non-zero normal component of the IMF penetrating across the boundary as well as a twisting action of the field-aligned currents were taken into account. The main joint effect of these two factors was shown to result in a strong distortion of a rectangular grid mapped from the magnetopause to the ionosphere along the near-cusp field lines.

Tsyganenko (1988) developed a model representing the magnetic field of the field-aligned current system in the quasi-dipolar region and capable of simulating its real sheet-like structure. A direct approach, that is an integration over the prescribed current distribution, is quite useless in this case, since the volume integrals over curved current flow lines cannot be reduced to manageable quadratures. That difficulty was sidestepped in the work by a special choice of the vector potential. Basic considerations follow from the general representation (43) for the magnetic field vector as the sum of toroidal and poloidal components (see also Backus, 1986). The toroidal term can be

rewritten as

$$\mathbf{B}_t = \nabla \times \mathbf{A}_t = \nabla \times (\mathbf{R}F_1) = \nabla F_1 \times \mathbf{R}\,.$$

The corresponding toroidal magnetic field lines are thus orthogonal to $\mathbf{R}$ at any point and, hence, lie on spherical surfaces R = const. The field produced by Birkeland currents has similar structure at relatively small distances and the disturbance vectors are approximately perpendicular to the dipolar field lines. Therefore, it is natural to represent the corresponding vector potential in a similar form. The only difference is that instead of $\mathbf{R}$ we have to substitute the dipole magnetic field vector $\mathbf{B}_d$, so that

$$\mathbf{A} = \mathbf{B}_d \cdot F(\mathbf{R})\,. \tag{57}$$

Since $\nabla \times \mathbf{B}_d = 0$ the magnetic field from Birkeland currents defined by (57) can also be represented as $\mathbf{B} = \nabla F \times \mathbf{B}_d$. Explicit relations for the components of the potential (57) in spherical solar-magnetic coordinate system (R, θ, λ) read as follows

$$A_R = 2\cos\theta f(\mathbf{R})\,, \qquad A_\theta = \sin\theta f(\mathbf{R})\,, \qquad A_\lambda = 0\,, \tag{58}$$

where $f(\mathbf{R})$ corresponds to the products of $F(\mathbf{R})$ with a common factor from the two components of $\mathbf{B}_d$. The function $f(\mathbf{R})$ is sought then in the form

$$f(\mathbf{R}) = CR^{-\gamma}\sin\lambda\cos\theta\beta(L) \tag{59}$$

where C is a constant defining the net current in the circuit and the factor $\sin\lambda$ provides the simplest longitudinal dependence of the field-aligned current magnitude, with the maxima of $|j_\parallel|$ being located at dawn and dusk meridians. The factor $\cos\theta$ is introduced in (59) from symmetry considerations, in order for A_R and A_θ to be even and odd functions of latitude, respectively. The last factor $\beta(L)$ defines the latitudinal structure of the field-aligned current and is chosen as a function of the L-parameter, since Birkeland current density must have a sharp maximum throughout the whole field line corresponding to the shell with $L = L_0$. The function $\beta(L)$ and the exponent γ are specified from the following considerations. The high-latitude portion of the shell $L = L_0$ near the Earth can be approximately considered as a cylindrical surface crossing the ionosphere along the circular boundary of the polar cap of radius $\rho_0 = R_E \sin\theta_0 = R_E/L_0^{1/2}$. Then it is easy to find the vector potential corresponding to a given sinusoidal distribution of Birkeland current density at the cylindrical surface, assuming the latter to be infinitely extended in both directions along the z-axis. This assumption can be motivated by equivalence of the contribution from the lower part of the cylinder (i.e., lying under the ionosphere) to that from the ionospheric closure current in case of a uniform conductivity of the planar model ionosphere. Magnetic field of this current system is uniform and directed along the Sun–Earth line above the polar cap, while outside the cylinder the field has a configuration corresponding to a two-dimensional dipole. Hence, the vector potential can be represented in the cylindrical coordinates (ρ, λ, z) as $\mathbf{A} = (0, 0, A_z)$ where

$$A_z = \begin{cases} B_0\rho\sin\lambda\,, & \rho \le \rho_0\,, \\ B_0\rho_0^2\rho^{-1}\sin\lambda\,, & \rho \ge \rho_0\,. \end{cases} \tag{60}$$

The factor B_0 defines the magnitude of the disturbance in the polar cap, so that $B_0 > 0$ yields a sunward field vector, which corresponds to downward current in the dawn sector and upward one in the dusk. Since at high latitudes $A_z \approx A_R$, substituting $\rho = R \sin\theta = R^{3/2}L^{-1/2}$ in (60) gives

$$A_R \sim \begin{cases} L_0 L^{-1/2}, & L \geq L_0, \\ L^{1/2}, & L \leq L_0. \end{cases} \tag{61}$$

Thus, to obtain a 'curtain-like' structure of $j_\parallel$ with maximum at $L = L_0$, it is necessary to specify the function $\beta(L)$ in (59) in accordance with (61). A simple analytical approximation for $\beta(L)$ with the required properties reads

$$\beta(L) = L^{1/2}\alpha(L) + L_0 L^{-1/2}[1 - \alpha(L)], \tag{62}$$

where

$$\alpha(L) = \frac{1}{2}\left\{1 - \frac{L - L_0}{[(L - L_0)^2 + \Delta L^2]^{1/2}}\right\}. \tag{63}$$

In contrast with the potential (61), the function (62) has finite derivatives at $L = L_0$, the parameter ΔL defining a characteristic thickness of the field-aligned current sheet. The exponent γ in (59) can be evaluated from the following. In case of a strictly radial geometry of the field-aligned currents the amplitude of the transversal disturbance ΔB would be proportional to R^{-1}, which corresponds to $\gamma = 0$. In reality, the currents flow along nearly dipolar field lines and hence ΔB should decrease more rapidly with distance, so $\gamma > 0$. In the final version of the model value $\gamma = 0.3$ was assumed, based on an *a posteriori* inspection of numerical results.

Magnetic field and current distributions obtained from the vector potential (58) yield reasonable results in the high-latitude region. However, at low latitudes this representation meets with some problems related to the geometry of the closing currents, which concentrate near the origin in the model instead of being distributed somewhere in the distant magnetosphere as required by physical considerations. For that reason, the vector potential was modified by adding a correction term providing an improvement of the current streamline configuration.

Figure 25 shows a three-dimensional view of the model current streamlines corresponding to the northern half of the large-scale system I of Birkeland currents. The joint contribution from the I and II systems can be described by a superposition of two model distributions with properly defined values of the parameters C, L_0, and ΔL, which is illustrated in Figure 26. The plot displays the dawn-dusk profile of the transverse magnetic disturbance from the model system of Birkeland currents and the corresponding distribution of the radial component of the current density. The plots are computed for the geocentric distance $R = 1.1\ R_E$ corresponding to the heights of the TRIAD and MAGSAT spacecraft orbit. As is readily apparent from the Figure, the profile of ΔB_λ shows a resemblance with plots given in experimental studies (e.g., Zanetti *et al.*, 1983).

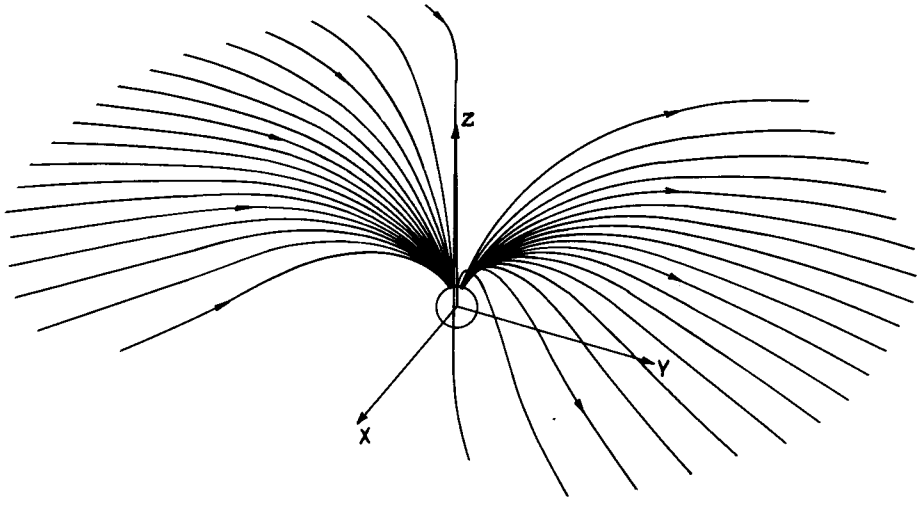

Fig. 25. A perspective view of the current streamlines in the model of the large-scale Birkeland current system (Tsyganenko, 1988). Only those streamlines corresponding to the northern half of the system I are shown.

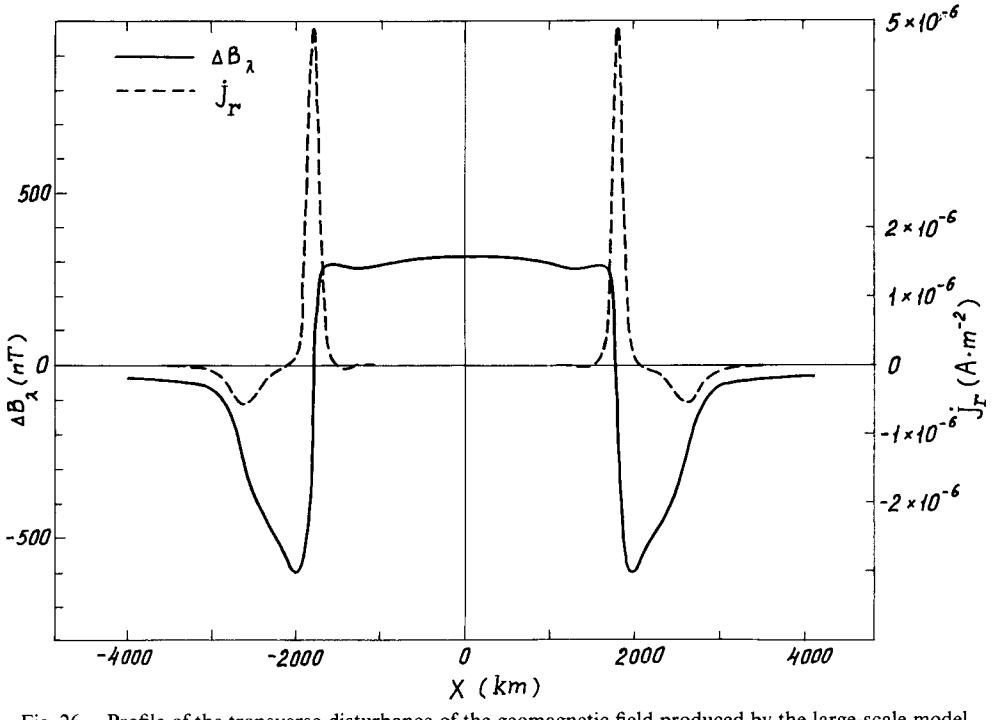

Fig. 26. Profile of the transverse disturbance of the geomagnetic field produced by the large-scale model Birkeland current system at height $H = 0.1\,R_E$ versus distance X from the pole measured along the dawn-dusk meridian. The broken line displays the corresponding distribution of the radial component of the current density.

In Figure 27 the corresponding configuration of the electric current streamlines in the dawn meridian plane is shown. The upper (downward) and the lower (upward) bundles of lines correspond to the systems I and II, respectively. This figure reveals one of drawnbacks of the model. As can be seen, a portion of the polarward current does not follow the dipolar magnetic field lines, but deviates towards the larger L values. It should

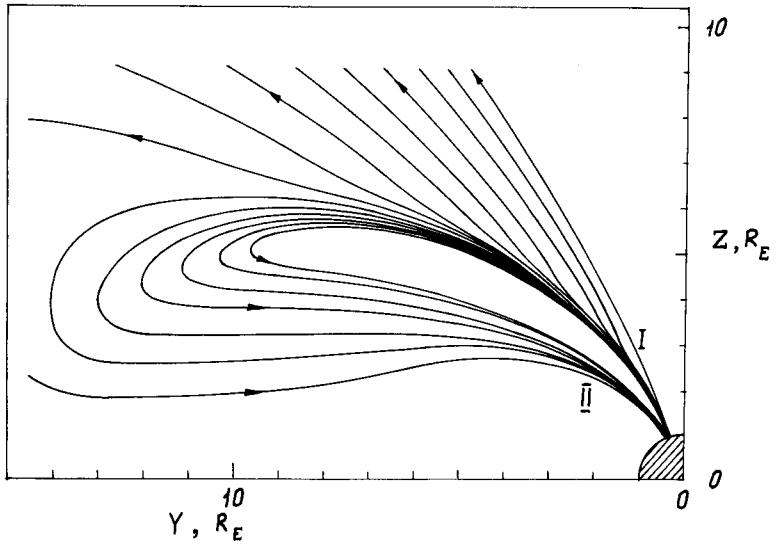

Fig. 27. Configuration of the model Birkeland current streamlines in the first quadrant of the dawn-dusk meridian plane (Tsyganenko, 1988). Beyond $R \sim 10\ R_E$ the streamlines of the high-latitude system I turn back and approach the Earth as the system II streamline bundle; this is merely a model artefact (see text).

also be noted that the system II bundle does not close through the equatorial magnetosphere, but turns towards higher latitudes at $R \sim 10$–$15\ R_E$ and then returns back to the Earth merged into the system I bundle.

Being designed in one of the first attempts to represent the magnetic field of Birkeland current systems, the outlined model is rather crude. Nonetheless, in the quasi-dipolar region $R \lesssim 5-7\ R_E$ it provides a sufficiently good results and can be used for a quantitative evaluation of the influence exerted by Birkeland currents upon the magnetospheric structure and field line mapping.

2.3.3. *Ring Current and Partial Ring Current Systems*

The first studies of the ring current magnetospheric effects date to early sixties, when after the discovery of the radiation belts a question on their role in geomagnetic disturbances was raised (Akasofu and Chapman, 1961). Those estimates were based on assuming an equatorial profile of the energy density of trapped particles $\varepsilon(r_e)$, specifying their pitch-angle distribution function, and adopting a dipolar background magnetic field configuration. This allowed to compute a local electric current density

as a function of coordinates, using the well-known relation given by the adiabatic theory (Parker, 1957)

$$\mathbf{j} = \frac{c}{B^2}\,\mathbf{B} \times \left\{\nabla p_\perp + \frac{p_\parallel - p_\perp}{B^2}\,(\mathbf{B}, \nabla)\mathbf{B}\right\}. \tag{64}$$

Integration over the current distribution yields the magnetic field of the model ring current in the linear approximation. Being added to the undisturbed background field, it provides the basis for the next iterations leading eventually to a self-consistent solution.

Later on a significant development of those calculations was done in a number of works using new data on energy spectra and spatial distribution of the trapped particles (e.g., Hoffman and Bracken, 1965, 1967; Schield, 1969). Hoffman and Cahill (1968) made an attempt to solve an inverse problem of refining the energy density profiles based on spacecraft magnetic measurements. Kendall *et al.* (1966) proposed a significantly improved method for calculating the magnetic field of the ring current and its model representation. Namely, instead of a cumbersome procedure of a direct Biot–Savart integration aimed at derivation of B_R- and B_θ-components, they introduced a flux function $\psi(R, \theta) = A_\varphi(R, \theta)R \sin\theta$, where A_φ is the azimuthal component of the vector potential. In any axisymmetrical magnetic field configuration the function ψ conservs its values along a field line. Representing ψ as an expansion in the associate Legendre functions

$$\psi(R, \theta) = \sum_{n=1}^{\infty} A_n(R) P_n^1(\cos\theta) \sin\theta \tag{65}$$

allows to reduce the task to a simple one-dimensional boundary problem for a few first functions $A_n(R)$. This approach was used by Sozou and Windle (1969a, b, 1970), who carried out a detailed study of nonlinear effects and their dependence on the total energy of the ring current particles. Figure 28 displays the pattern of contours of constant electric current density in the self-consistent model radiation belt with a total energy of particles $W = 4.4 \times 10^{22}$ ergs corresponding to the magnetic field depression in the centre of the ring current belt $\Delta B \approx -110$ nT. The upper half of the plot shows the result obtained in the linear approximation and the lower part gives the self-consistent distribution. The inner eastward current as well as more intense outer westward one are clearly seen.

The most comprehensive study in this aspect was done by Sckopke (1972), who presented an extensive analysis of such questions as the role of the pitch-angle anisotropy, the influence of non-dipolar terms in the background magnetic field model, and the difference between the linear and the self-consistent solutions. In particular, a modification of the well-known Dessler-Parker-Sckopke relation has been obtained which takes into account the homogeneous part of the external shielding field $B_{CF}^{(0)}$:

$$\mathbf{M}_E \cdot \mathbf{B}_{RC}(0) \approx 2W_{\text{kin}} + W_{\text{mag}}^* + 2\mathbf{M}_{RC}\mathbf{B}_{CF}^{(0)}, \tag{66}$$

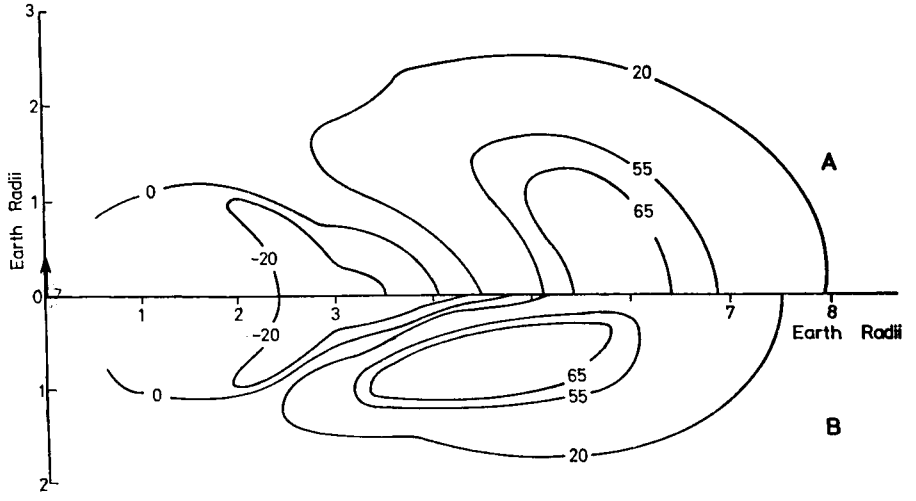

Fig. 28. Contours of constant azimuthal electric current density in the model ring current (Sozou and Windle, 1969b). The upper half (A) of the plot displays a linear approximation result and the lower one (B) corresponds to a self-consistent solution. The isolines are labeled in units 2.8×10^{-10} A m^{-2}.

where $\mathbf{M}_E$ and $\mathbf{M}_{RC}$ are the magnetic moments of the Earth and the ring current, $\mathbf{B}_{RC}(0)$ is the magnetic field produced by the ring current at the origin, W_{kin} and W^*_{mag} are, respectively, the kinetic energy of the trapped particles and the magnetic energy of the ring current field contained within a spherical model magnetopause corresponding to the homogeneous shielding field $\mathbf{B}^{(0)}_{CF}$. Equation (66) shows that, apart from the direct contribution of the magnetopause currents to the observed Dst value, there exist an indirect effect related to the ring current. Assessing $M_{RC}/M_E \sim 0.2$ we find the last term in (66) to give a positive (northward) contribution to $B_{RC}(0)$ of about $0.4B^{(0)}_{CF}$, which amounts to a significant value of ~ 8 nT for $B^{(0)}_{CF} = 20$ nT.

Sckopke (1972) established also that practically in all cases the linear approximation solutions do not differ significantly from the self-consistent ones. An important detail has been also pointed out in this aspect concerning Equation (66). Namely, the self-consistent values of $B_{RC}(0)$ were found to be always a little smaller than the linearly computed ones, in apparent contradiction to a widely accepted view based on a superficial account of the term W^*_{mag} in (66). Actually, in going from linear to self-consistent solution the appearance of the positive term W^*_{mag} in the right-hand side of (66) is accompanied by a significant decrease in W_{kin} due to a corresponding re-structuring of the magnetic field leading thus to a negative net change of $B_{RC}(0)$.

Effects of the plasma pressure anisotropy were taken into account in many models of the ring current. However, all of them assume only very special kind of the distribution function incorporating the pitch-angle dependence in the factor $(\sin\theta)^{\alpha+1}$ (Parker, 1957), which allows to calculate in a simple way the pressures and the current density along the field line tube. Moreover, in all the models a single value of α was ascribed to the whole ring current. Sckopke (1972) made an extensive quantitative study of

dependence of the model ring current parameters on α. A general conclusion is that the integral quantities W_{kin}, $R_{RC}(0)$, M_{RC}, and $W_{mag}/2W_{kin}$ show a distinct decrease with growing α, which has an obvious explanation based on the fact that larger values of α correspond to a more rapid decrease of plasma density away from the equatorial plane and hence to smaller total amounts of trapped particles with lesser magnetic effect.

The ring current models of this kind were used by Voigt (1981), who incorporated them into his magnetospheric magnetic field model with independent physical parameters. Radial profiles of the equatorial energy density were fitted to those obtained by Frank (1967) from the measurements of the outer radiation belt protons. Figure 29

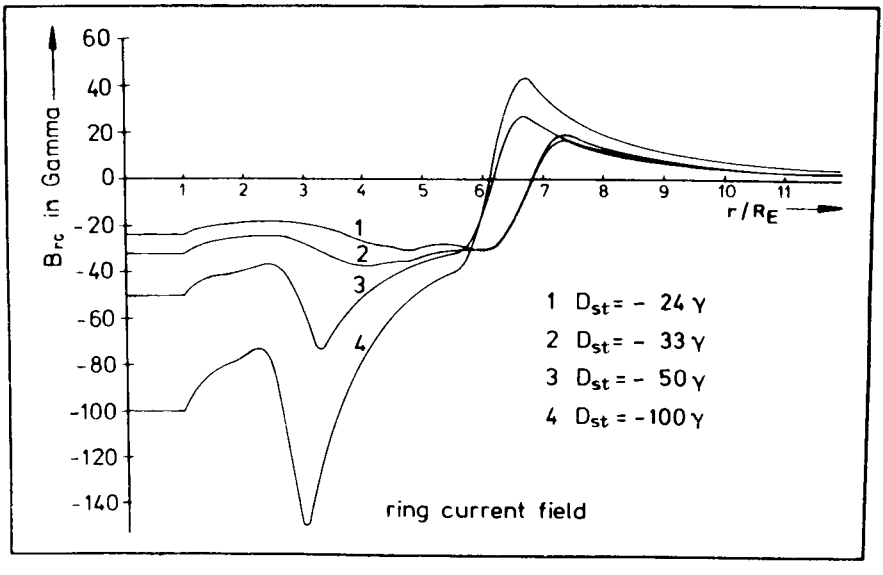

Fig. 29. Profiles of the transverse component of the model ring current field in the equatorial plane plotted versus radial distance, for four values of the ring current intensity (Voigt, 1981).

shows the plots of radial distribution of the model ring current magnetic field $B_{RC}(R)$ in the equatorial plane for four values of $B_{RC}(0)$. Larger ring current intensities are manifested in a more depressed field within distances $R \leq 6\,R_E$, the most dramatic changes being observed at $R \sim 3$–$4\,R_E$ between the zones of the outer westward and the inner eastward current. This is accompanied by an earthward shift of the depression peak. At larger distances the disturbance becomes positive and then decreases as R^{-3} in the current-free region.

A further analysis of those models is hindered by that neither Voigt (1981) nor Sckopke (1972) published numerical values of their ring current parameters and the corresponding model expansions. One of a few exceptions in this sense is given by the paper of Kendall *et al.* (1966) (see also a book by Akasofu and Chapman, 1972), who provided the tables of functions $A_n(R)$ and their derivatives entering the expansions

similar to (65). An alternative description of the ring current field was given by Schield (1969), who tabulated directly the B_R- and B_θ-components.

However, all these results were obtained many years ago from the then sparse data on particles and correspond mainly to quiet conditions. A rapid advance of experimental technique has led recently to a radical revision of earlier concepts of the ring current composition and sources as well as to a significant refinement of data on energetic spectra, pitch-angle and spatial distributions (see a review by Williams, 1987, and references therein). However, in spite of a remarkable number of papers on radiation belts, they are related mainly to dynamics of energetic particle injection, drift, and losses. Calculations of the electric current distribution were done lately only in a few works, which concentrated primarily on analyzing separate events (e.g., Lui *et al.*, 1987). This reflects to a large degree a significantly more complex structure of the observed ring current in comparison with the idealized axially symmetric models. In fact, existing experimental data speak in favour of a continuous merging of the tail current sheet with the ring current at the nightside (e.g., Speiser and Ness, 1967; Fairfield *et al.*, 1987). Sugiura (1972) and Sugiura and Poros (1973) based on measurements of the scalar quantity $\Delta B = |\mathbf{B}_I + \mathbf{B}_E| - |\mathbf{B}_I|$ called in question the results of theoretical modeling the ring current similar to those shown in Figure 28 and proposed instead a concept of a single westward equatorial current sheet at the nightside, which approaches the Earth up to very close distances.

In this context it is worth showing in Figure 30 the results of Lui *et al.* (1987) obtained from the AMPTE/CCE spacecraft measurements. The four panels display the radial profiles of the electric current density calculated from (64), where the net pressures $p_\parallel$ and $p_\perp$ were derived from the ion flux measurements in the range of energies from 25 keV to 1 MeV and the dipolar magnetic field was assumed. Solid curves correspond to different stages of a storm, while a broken line yields a pre-storm current density profile. As can be seen from the curves, the transition between the eastward and westward current occurred in all cases at $R \sim 3$–$4\ R_E$. It should be emphasized that all the current distributions were obtained for the early evening MLT hours and can thus be substantially different from those pertaining to the midnight sector.

The above approach implies an *a priori* predetermined background magnetic field model as well as a given distribution of the plasma energy density and, hence, is of little value in empirical modeling based on magnetic measurements. The latter requires a compromise between a relative simplicity and flexibility of mathematical representation. One of such simple models was suggested by Tsyganenko and Usmanov (1982). The model is axially symmetric and can be represented in the solar magnetic cylindrical coordinates (ρ, φ, z) by a vector potential $\mathbf{A} = (0, A_\varphi, 0)$, where

$$A_\varphi = C\rho(\rho^2 + z^2 + 4\rho_0^2)^{-3/2}. \tag{67}$$

The only difference of (67) from a purely dipolar vector potential is the additional term $4\rho_0^2$ which eliminates the singularity at the origin. At large distances the potential (67) yields a nearly current-free dipolar field, while at $R = (\rho^2 + z^2)^{1/2} \lesssim 2\rho_0$ it provides a ring-like continuous current distribution with a characteristic radius of the order of ρ_0.

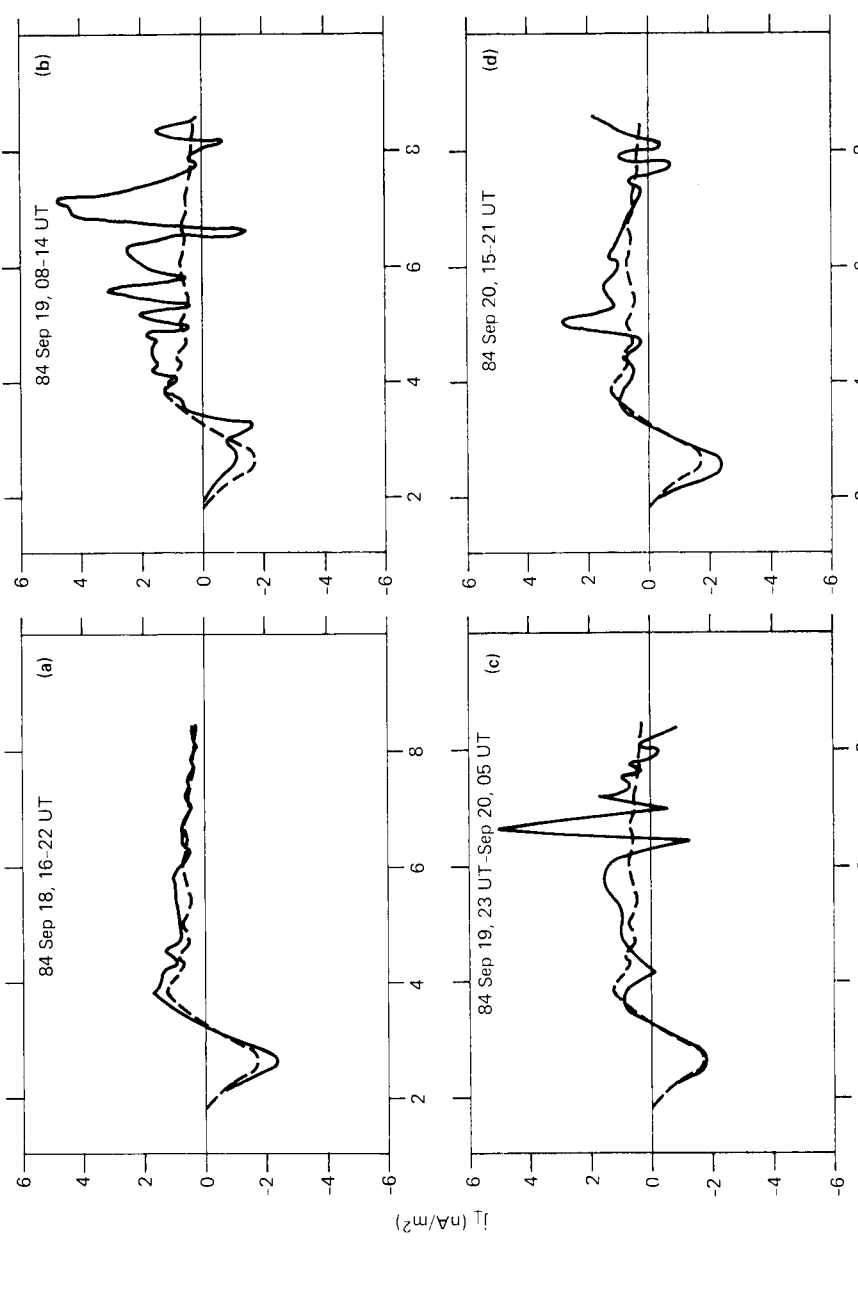

Fig. 30. Radial profiles of the ring current density in the duskside equatorial magnetosphere calculated from (64) by using the AMPTE/CCE particle measurements and assuming the background magnetic field to be purely dipolar. Solid lines in the four panels are obtained for a storm period of September 18–20, 1984 and correspond to (a) the initial phase, (b) the main phase peak, and (c–d) the storm recovery. Broken lines display the pre-storm profile (Lui *et al.*, 1987).

From (67) the field components can be obtained as

$$B_\rho = B_0 \frac{12\rho' z'}{(\rho'^2 + z'^2 + 4)^{5/2}} \tag{68}$$

and

$$B_z = 4B_0 \frac{2z'^2 - \rho'^2 + 8}{(\rho'^2 + z'^2 + 4)^{5/2}}, \tag{69}$$

where B_0 corresponds to the magnitude of the field depression at the origin and the coordinates ρ and z are expressed in dimensionless units so that $\rho' = \rho/\rho_0$ and $z' = z/\rho_0$. Figure 31 shows the meridional cut of the model ring current as a family of contours

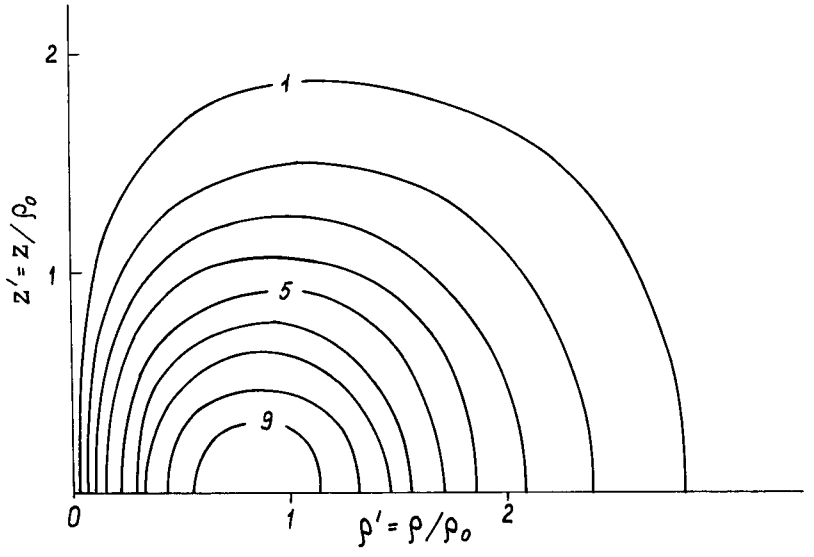

Fig. 31. Contours of constant current density in the meridional cross-section (upper half only) of the model ring current. The isolines are labeled in arbitrary units (Tsyganenko and Usmanov, 1982).

of constant j labeled in arbitrary units. The maximal current density is located at $\rho = 0.8\rho_0$, whereas the magnitude of the field depression increases monotonically towards the Earth. The model is very simple and allows to describe the gross observed features of the ring current by a proper fitting of only two parameters, ρ_0 and B_0. As shown by Stern (1985), this representation is convenient for taking into account the ring current effects in modeling the field from the magnetopause currents (see Subsection 2.2.2.1).

One of basic shortcomings of that model consists in its inability to vary the scale thickness of the current distribution in the north–south direction as well as its complete axial symmetry. In reality, there exists a pronounced day–night asymmetry of the ring

current, so that the nightside current intensities dominate by a factor of 2 or 3 (Iijima *et al.*, 1989). During strongly disturbed periods this asymmetry seems to become even larger. Roelof (1987) presented a convincing evidence of extremely strong asymmetry of the storm-time ring current, based on the newly developed technique of energetic-neutral-atom (ENA) imaging the radiation belt ion population. Measurements of ENA fluxes made from the ISEE-1 spacecraft during a storm with $Dst = -240$ nT indicated a drastic midnight–noon asymmetry in differential trapped ion intensity, with a corresponding ratio amounting to 20:1 in the region $3 \leq L \leq 5$.

The next important feature that also exhibits a distinct dependence on the geomagnetic activity is the dawn-dusk asymmetry of the magnetosphere. This effect was found still long ago in the ground based magnetometer data (e.g., Kamide and Fukushima, 1971) as well as from the spacecraft measurements (Langel and Sweeney, 1971) and should be considered now as a firmly established fact that also needs to be adequately simulated in future models.

Usmanov and Tsyganenko (1984) made a quantitative study of the dawn-dusk asymmetry of the magnetosphere on the basis of the merged IMP-HEOS-ATS spacecraft dataset and a model of the partial ring current. The work was primarily aimed at a derivation of the gross large-scale magnetic effects of this current system at moderate

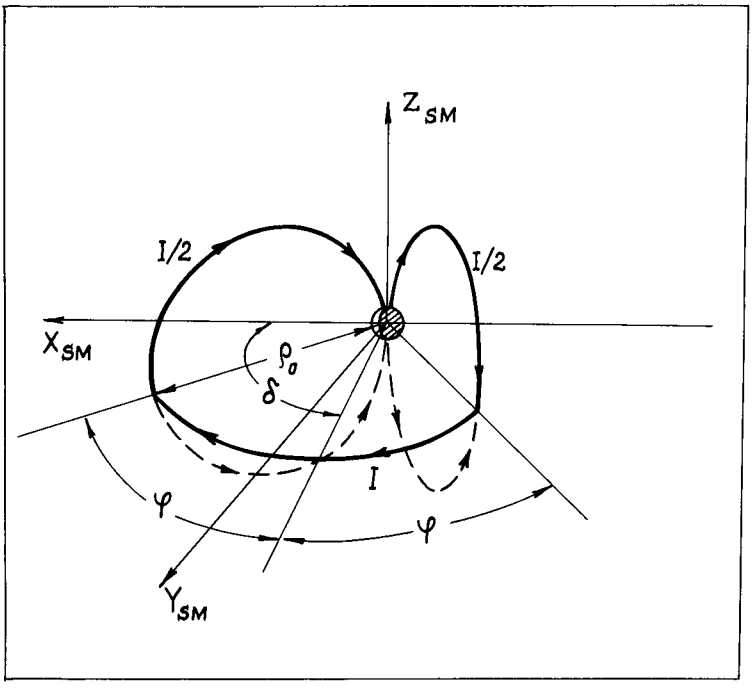

Fig. 32. Schematic view of the partial ring current system used by Usmanov and Tsyganenko (1984) for constructing approximate model expansions, which provide a spread-out distribution of the current density and a smoothly varying magnetic field.

geocentric distances of $R \sim 3$–$7\ R_E$, rather than at a detailed simulation of its structure including Birkeland and ionospheric currents. A schematical 'wire circuit' consisting of five circular segments (Figure 32) was adopted as a starting point for constructing the partial ring current model. Contribution from each segment to the net vector potential was represented by an integral with its subsequent reduction to approximate expansions. Combining them in accordance with the geometry of the current system shown in Figure 32 led to a final numerical model incorporating four parameters, which are the total current in the circuit I, the radius of the equatorial current ρ_0, its angular half-width ϕ, and the angle δ defining the azimuthal position of the whole system, as shown in Figure 32. Due to the assumed approximate representation, the model magnetic field corresponds to a continuously spreadout current distribution, in contrast with the initial thin wire model shown in the figure.

The partial ring current model was incorporated as additional source in the model of Tsyganenko and Usmanov (1982) and then was least squares fitted to datasets sorted out in the K_p and AE intervals. The results are shown in Figure 33, where the obtained dependence of δ and $E_{eq} = 2\varphi I/c\rho_0$ on the disturbance indices is shown. The latter quantity B_{eq} is proportional to the net current I and gives the field produced by the partial ring current at the origin ($B_{eq} > 0$ corresponds to negative B_z, i.e., to a more depressed field near the Earth). Every value of the K_p index (or the AE interval) in the plots corresponds to a dataset comprising about ~ 1000 vector averages. A clear tendency of B_{eq} to increase with the activity indices is seen. However, the angular position δ does not show any ordered dependence on K_p; nevertheless, such a dependence is discernible in the lower plot, so that the system seems to rotate from the postnoon to the premidnight sector with growing AE-index, though in general the effect is not very large.

The outlined study is one of the first attempts to tackle the asymmetry problem. Successful advance in this direction will depend largely on the proper choice of the current system geometry. The circuit shown in Figure 32 corresponds actually to only one of several theoretically possible hypotheses. An alternative variant for explaining the observed asymmetry proposed by Crooker and Siscoe (1981) (see also Harel *et al.*, 1981) is based solely on an integral effect of the field-aligned currents with prevailing inflow in the noon sector and corresponding outflow at night local time hours. Next, it is necessary to significantly extend the existing experimental databases, because the asymmetry effects are manifested most distinctly during disturbed periods whose statistical weight in datasets falls off rapidly with growing K_p or AE. At last, more adequate procedures for sorting out the data should be developed, based on a more accurate account of physical conditions. Thus, the asymmetry effects are the most distinct just after the particle injection events (McIlwain, 1974; see also Williams, 1987, and references therein) and hence compiling the datasets in the K_p-index intervals is scarcely able to yield a good result.

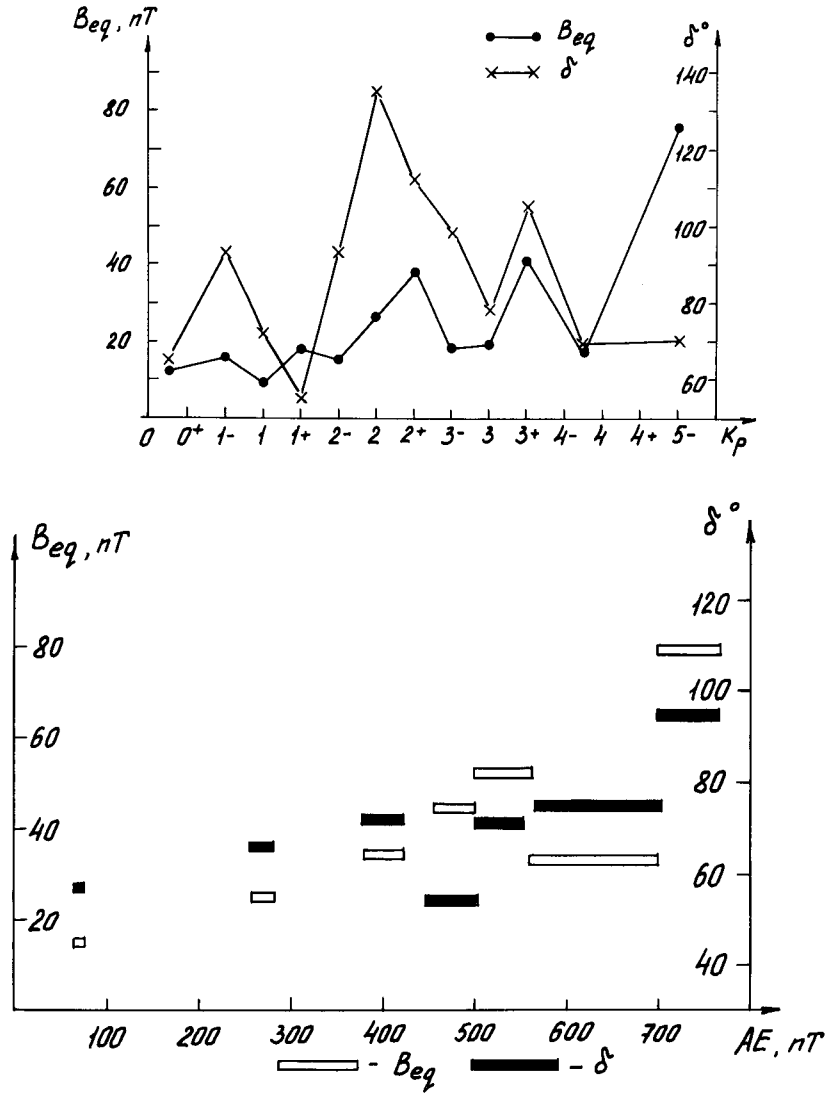

Fig. 33a–b. Parameters B_{eq} and δ of the model partial ring current plotted versus geomagnetic activity indices. The first parameter defines the net current magnitude and the second one defines the angular position of the system shown in the previous figure (Usmanov and Tsyganenko, 1984). (a) Dependence on the K_p-index. (b) Dependence on the AE-index.

3. Magnetospheric Structure as Inferred from Quantitative Models

In contrast with case studies of separate events, the empirical modeling based on large bodies of data is capable of deriving a global structure of the magnetosphere. As already noted, a weak point of this approach consists in mixing the data pertaining to different geophysical situations within a single 'noisy' set; this imposes serious limitations on the

amount of information which could be deduced from them. Nonetheless, some results obtained in a series of recent papers reveal hopeful prospects in view of a continuous accumulation of new data, development of more realistic models, and a rapid progress of computer capabilities. A brief survey of those results is given below.

3.1. Model distributions of the magnetic field and electric current in dependence on the disturbance level

Figures 34–37 show the noon–midnight magnetospheric magnetic field configurations plotted for three intervals of the K_p-index by using the newest version of the empirical model of Tsyganenko (1989a, referred to henceforth a T89). The merged spacecraft dataset used as the experimental base for the model contains 36682 field vector averages, being as yet the largest body of data ever used in such studies. The dataset includes (i) 12616 points used by Mead and Fairfield (1975) and corresponding to measurements on board the IMP-D, F, G, and I spacecraft during 1966–1972 in the distance range 4–17 R_E, (ii) 6248 points generated from data of HEOS-1 and -2 spacecraft taken in

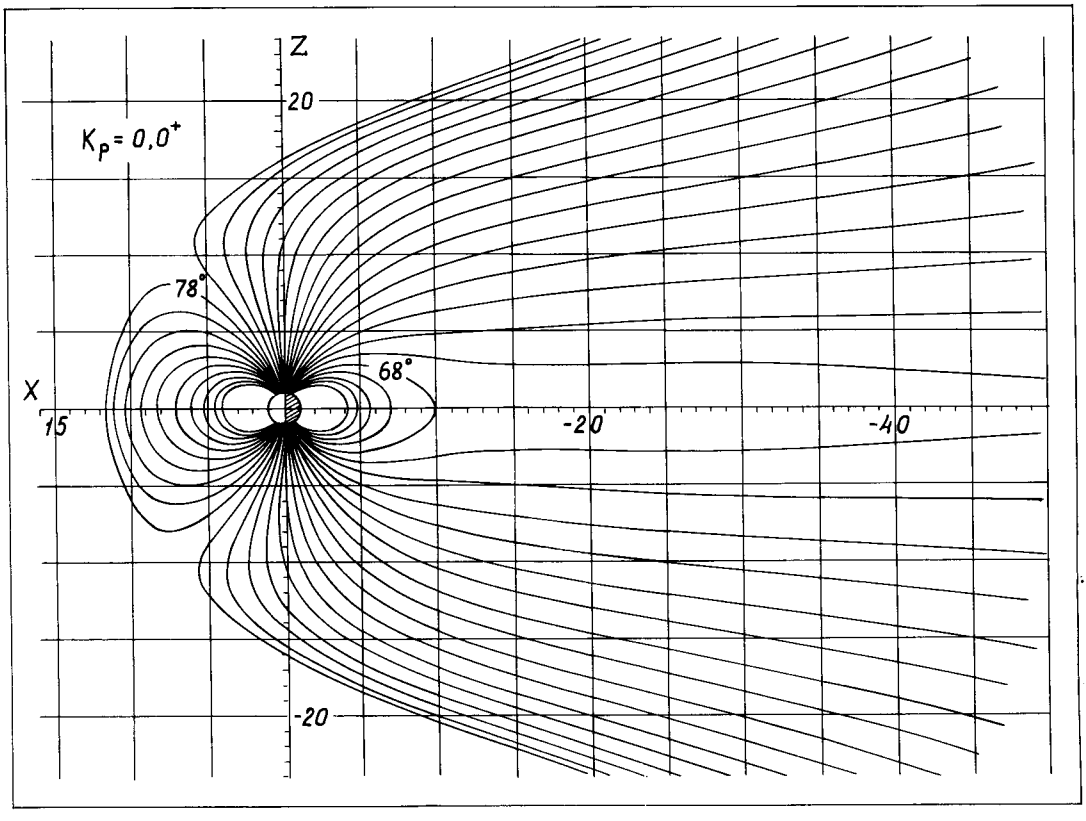

Fig. 34. Magnetic field configuration in the noon–midnight meridian plotted by using the model of Tsyganenko (1989a) for very quiet conditions with $K_p = 0, 0^+$. Field lines start from Earth at latitudes 2° apart, beginning from 60°.

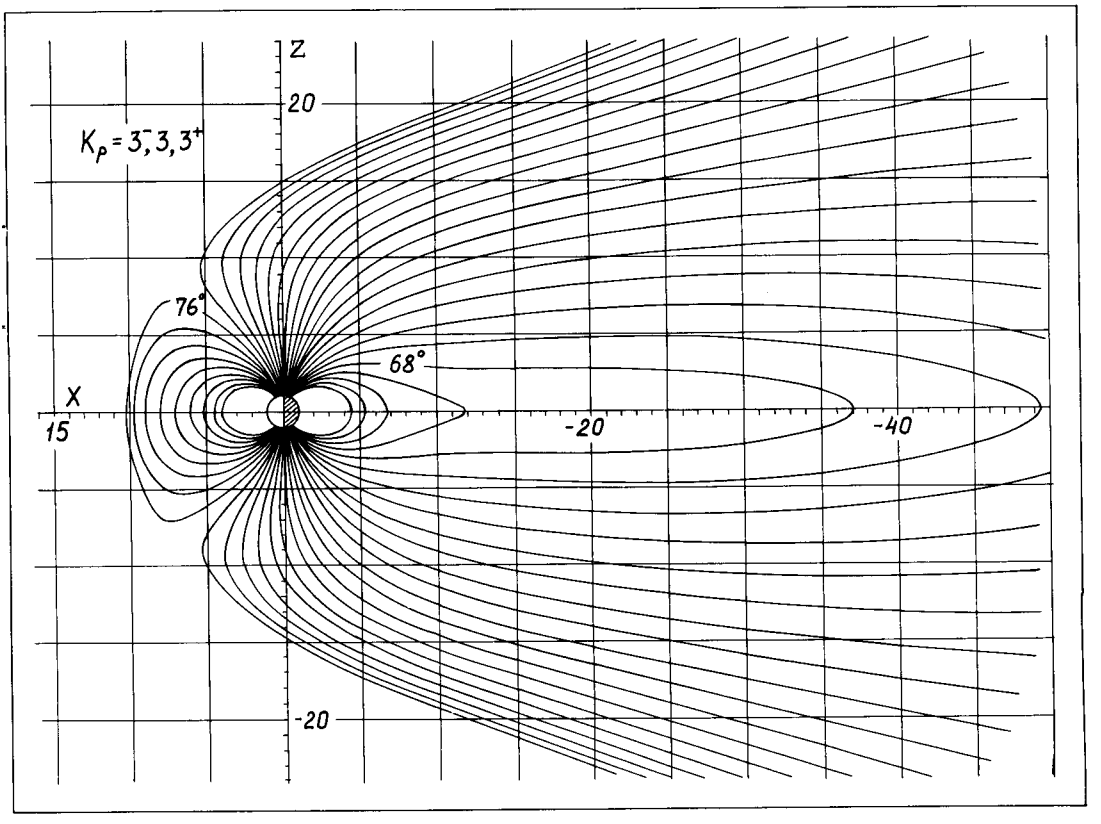

Fig. 35. Same as Figure 34, except for $K_p = 3^-, 3, 3^+$.

the high-latitude magnetosphere at distances 6–35 R_E during 1969–1972 (Hedgecock and Thomas, 1975), (iii) 11 150 points provided by six IMP spacecraft in the cislunar tail, and (iv) 6675 points from IMP-H and -J data in the middle tail region ($R \sim 25$–$45\ R_E$) taken in 1973–1980.

The total field from external sources is represented in this model by a sum of several terms. The first group of terms correspond to the contribution from the tail current system and the ring current. The intramagnetospheric part of this system forms a single spread-out current sheet incorporating a non-uniform distribution of the current density, spatial variation of the characteristic thickness in two dimensions, and the tilt-dependent warping described in more detail in Subsection 2.3.1 (Figures 18–20).

The central current sheet is complemented by two additional ones spaced by $R_T = 30\ R_E$ from the equatorial plane and simulating the effects of the closure currents.

The second group of terms represents the contribution from the rest part of the magnetospheric sources, mainly from the magnetopause shielding current. These terms are defined as formal expansions similar to those suggested earlier by Tsyganenko and

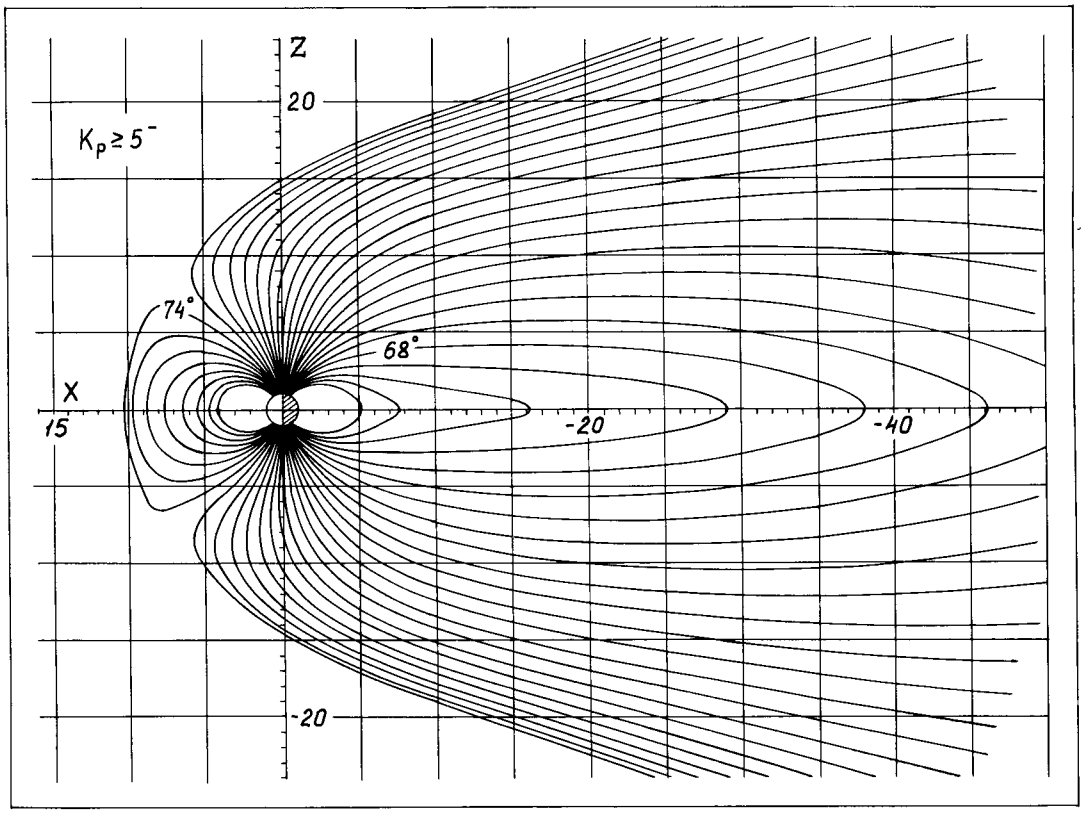

Fig. 36. Same as Figure 34, except for $K_p \geq 5^-$.

Usmanov (1982) and Tsyganenko (1987), (henceforth TU82 and T87, respectively)

$$B_x = e^{x/\Delta x}[a_1 z \cos\psi + (a_2 + a_3 y^2 + a_4 z^2) \sin\psi] ,$$
$$B_y = e^{x/\Delta x}[a_5 yz \cos\psi + (a_6 + a_7 y^2 + a_8 z^2) y \sin\psi] , \qquad (70)$$
$$B_z = e^{x/\Delta x}[(a_9 + a_{10} y^2 + a_{11} z^2) \cos\psi + (a_{12} + a_{13} y^2 + a_{14} z^2) z \sin\psi] ,$$

satisfying proper conditions of symmetry in y, z, and ψ. The equation $\nabla \cdot \mathbf{B} = 0$ yields four additional constraint relations decreasing the number of independent parameters to ten coefficients a_1–a_{10} and one nonlinear parameter Δx. As a matter of fact (see Subsection 2.3.2), the expansions (70) describe not only the Chapman–Ferraro field, but also that from the field-aligned currents, though significantly averaged and smeared out due to unsuitable form of the model functions.

In total the model contains 24 free parameters, whose values were least squares fitted to six datasets corresponding to six intervals of the K_p-index. A procedure for search of the model parameters is based on an iterative Newton–LeCam–Marquardt algorithm which minimizes the r.m.s. difference between the dataset and the model and is capable

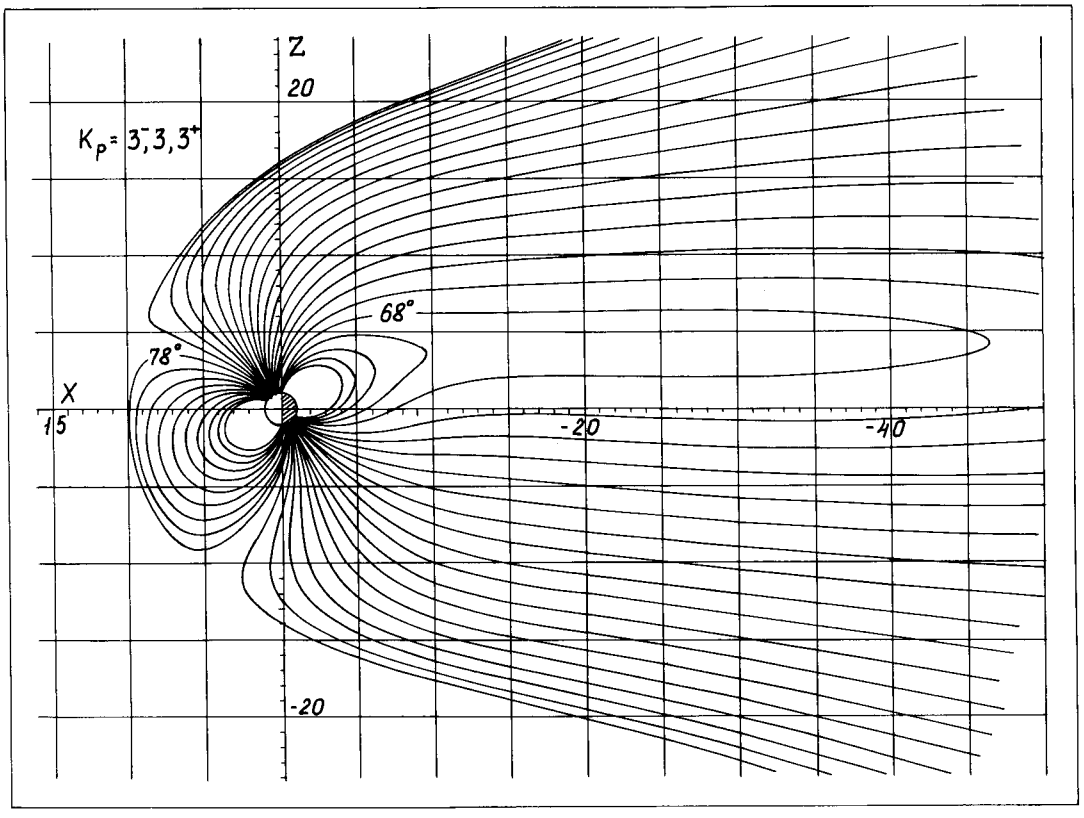

Fig. 37. Same as Figure 35, except for $\psi = 30°$.

of evaluating errors in the determined parameter values. A brief description of this technique is given in Appendix.

The most essential results evident in Figures 34–37 and noted also in earlier modeling studies are as follows. The increase of the disturbance level is accompanied by a decrease of the subsolar point distance, a 'peeling off' the dayside magnetic field lines with a decrease of the polar cusp latitudes, and a deepening of the magnetic field depression in the near nightside region manifested in a larger stretch of the field lines crossing the equatorial plane at $R \lesssim 10$–$15\ R_E$. It should be noted that this model provides the largest deformation of the nightside field lines, in comparison with all earlier versions. This result is quite clear, since the main improvements pertain just to the near nightside magnetotail region, as already discussed in Subsection 2.3.1. Spatial distribution of the net external field in the model can be visualized in Figure 38 showing contours of equal B_z values in the equatorial plane for $K_p = 0, 0^+, K_p = 3^-, 3, 3^+$, and $K_p \geq 5^-$. The main tendency is a significant deepening of the near-Earth depression with growing K_p, the minima of B_z being located near $x_{GSM} \approx -2.5\ R_E$ in all three cases. It should be understood, of course, that actual positions of B_z minima can be somewhat different from those obtained in the model. A relatively low density of the experimental data

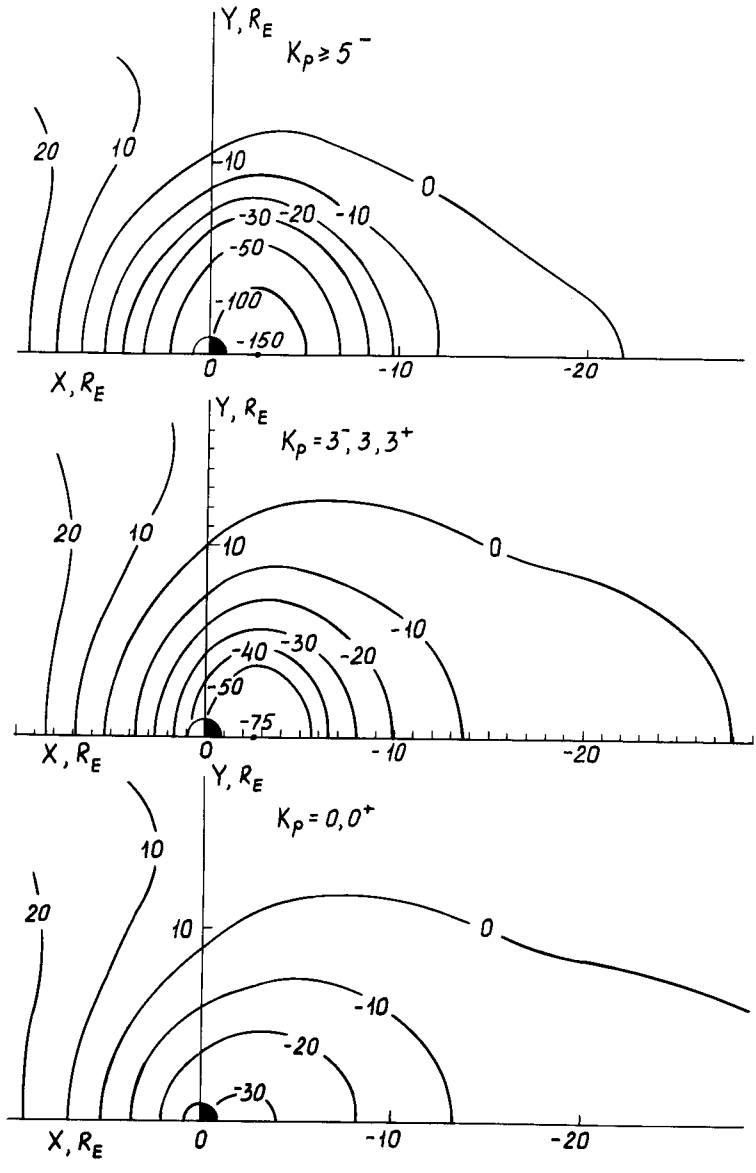

Fig. 38. Three families of the equal intensity contours of the external model field in the GSM equatorial plane for untilted geodipole corresponding to three levels of disturbance (Tsyganenko, 1989a).

points in the near equatorial magnetosphere and a complete absence of data at $R < 4\ R_E$ intrinsic in the datasets does not allow to resolve finer details. Nevertheless, the obtained minimal values of B_z are in a satisfactory agreement with recent measurements made at closer distance. Figure 39 shows the plots of radial distribution of the 'scalar anomaly' $\Delta B = |\mathbf{B}_{\text{measured}}| - |\mathbf{B}_I|$ in the near-equatorial nightside magnetosphere derived from the AMPTE/CCE measurements (Fairfield *et al.*, 1987). As can be seen from the figure,

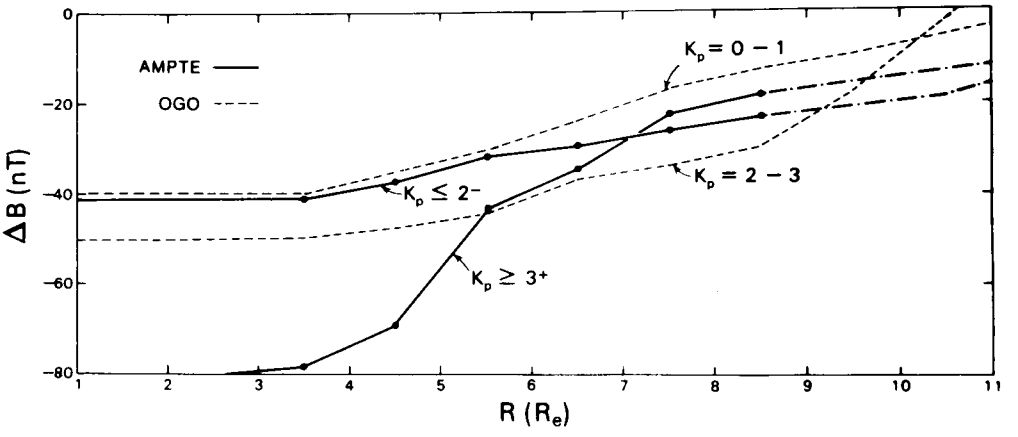

Fig. 39. Average values of $\Delta B = |\mathbf{B}_{measured}| - |\mathbf{B}_I|$, where $\mathbf{B}_{measured}$ is the total observed field and $\mathbf{B}_I$ is the internal field, as a function of radial distance in the midnight nearequatorial region for different K_p intervals. The solid and broken lines correspond to the AMPTE/CCE measurements and the results of Sugiura and Poros (1973), respectively (Fairfield *et al.*, 1987).

the depression increases towards the Earth reaching ≈ -80 nT at $R \lesssim 3\,R_E$ for $K_p > 3^+$, which may be compared with $B_z = -87$ nT at $R = 4\,R_E$, obtained from the model for $K_p = 4^-, 4, 4^+$.

Another tendency also clearly seen both in Figure 38 and in the tail field line configurations in Figures 34–37 is that the decrease in B_z occurs predominantly within the near tail domain with $x_{GSM} \gtrsim -12\,R_E$. At larger distances a slight increase of B_z with K_p is evident, manifested in an earthward shift of the $B_z = 0$ contour. This feature had been also noted in the T87 model as well as in a direct inspection of the averages calculated from the experimental B_z values inside the plasma sheet. A similar effect is clearly seen in the ΔB profiles derived from AMPTE data (Figure 39). Hence, there are good reasons to conclude that this is scarcely a modeling artefact but rather a manifestation of a real average increase of the tail magnetic flux connection through the distant neutral sheet during disturbed periods.

It can also be seen from Figure 38 that minimal equatorial values of B_z at a given tail cross section are attained near the midnight meridian, so that at $-60 \lesssim x_{GSM} \lesssim -20\,R_E$ the total model B_z increases towards tail flanks by 2–5 nT, in agreement with the statistical results by Fairfield (1986). It is worth emphasizing here that a care should be taken in what concerns the B_z values given by empirical models in the low-latitude tail region with $x_{GSM} \lesssim -10\,R_E$. The point is that small values of the net B_z in the near-plasma sheet are given by the difference of relatively large quantities corresponding to the oppositely directed contributions from the geodipole and the external currents, and hence the B_z distribution is extremely sensitive to the details of the electric current pattern in the tail. In the present case it is unlikely to obtain a detailed resolution of the current structure, since the main part of the tail field measurements correspond to the lobe region and the data are also relatively sparse in the range $-20 \leq x_{GSM} \leq -10\,R_E$ (see Figure 1 of Tsyganenko, 1987). For these reasons the

average observed B_z values in the tail may differ from those given by the model by $\sim$ 1–3 nT. It should also be noted that individual values of B_z in the original datasets show a strong scatter, partly related to the above mentioned imperfection of the K_p-index.

Of significant interest is to make an independent test of the model using the data from geosynchronous spacecraft measurements which were not included in the modeling dataset. Figure 40 shows plots of the B_z component of the external field near the

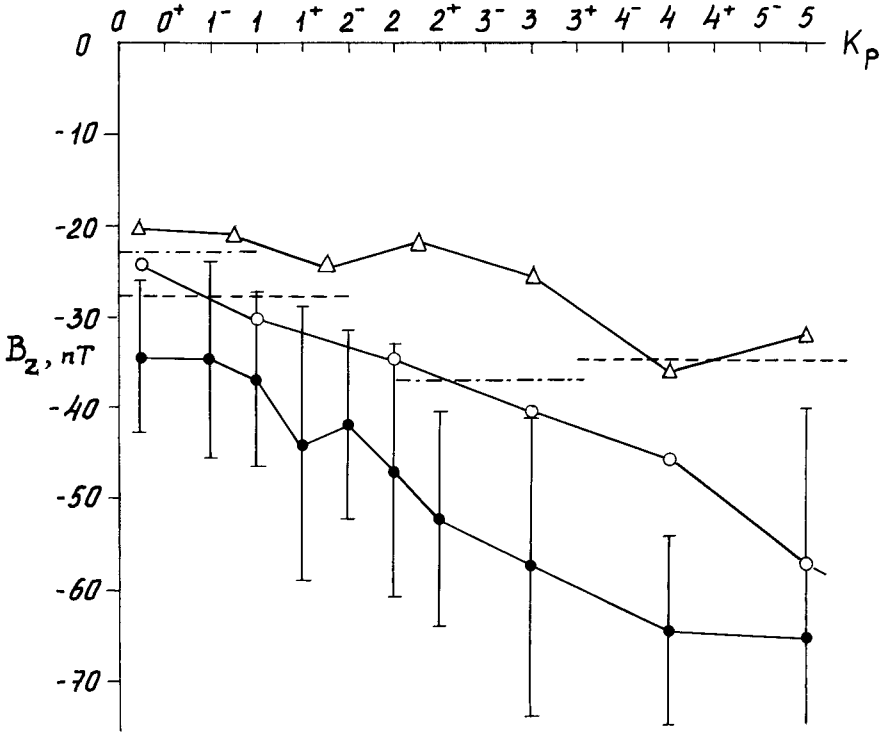

Fig. 40. Plots of the B_z component of the external magnetic field near the midnight point of the geosynchronous orbit ($X_{GSM} \approx -6.6\ R_E$) versus K_p. Open circles and triangles correspond to the models T89 and T87, respectively. Solid circles, dashed line, and dashed-dotted line represent the average values obtained from the ATS-1, AMPTE–CCE, and OGO-3, -5 spacecraft data, respectively (Tsyganenko, 1989a).

midnight point of the synchronous orbit ($R = 6.6\ R_E$) versus K_p-index. The open circles represent the B_z values computed by using the present model and the triangles correspond to the 'truncated' version of the T87 model. The solid circles give the average B_z values measured on board the ATS-1 satellite in 1967 (a total of 232 hourly averages), the vertical bars showing the r.m.s. deviation for each point. As can be visualized in the plots, the present model yields a significantly more depressed field than the T87 one, but the ATS-1 results are still lower by $\sim$ 10 nT. It is yet unclear, whether this discrepancy is due to an imperfection of the model or to a bias in the ATS data, but it should be

born in mind that the ATS H-component values were initially corrected by $\Delta H = -20$ nT, with a purpose to eliminate a positive shift mentioned by principal investigators (Coleman and McPherron, 1976). The adopted value of ΔH was evaluated on the basis of experimental data and model calculations of the location of the isotropic precipitation boundary due to a non-adiabatic scattering of particles in the near magnetotail (Sergeev *et al.*, 1983; see Section 4 below) and may well be in error of ~ 10 nT.

Dashed and dashed-dotted lines in Figure 40 represent the results of the AMPTE/CCE (Fairfield *et al.*, 1987) and OGO-3 and -5 (Sugiura and Poros, 1973) measurements at $x_{GSM} \approx -6.6\ R_E$, respectively. For small K_p values the present model shows a good agreement with the data, while for $K_p > 3^+$ it yields a somewhat more depressed B_z than that observed by the spacecraft.

TABLE I

Some characteristics and parameters of the T89 model for six intervals of the K_p-index. The notation is as follows: N is the number of data points in the set; $\overline{B}$ is the r.m.s. external field; λ is the r.m.s. residual field given by (A4); c_1,c_2, and c_3 are the coefficients defining the contribution from the intramagnetospheric current sheet and corresponding to three terms derived from potentials (50)–(52); a_{RC} is the scale radius of the ring current and γ_{RC} is a quantity defining its noon–midnight asymmetry; D is the nightside current sheet thickness (Tsyganenko, 1989a)

	$K_p = 0, 0^+$	$K_p = 1^-, 1, 1^+$	$K_p = 2^-, 2, 2^+$	$K_p = 3^-, 3, 3^+$	$K_p = 4^-, 4, 4^+$	$K_p \geq 5^-$
N	3975	9977	9848	7309	3723	1850
$\overline{B}$	15.49	19.06	21.71	25.48	28.58	32.88
λ	6.51	8.52	9.75	11.35	12.41	15.12
c_1	−98.72	−35.64	−77.45	−70.12	−162.5	−128.4
c_2	−10014	−12800	−14588	−16125	−15806	−16184
c_5	−10237	−13543	−16299	−19630	−27534	−36435
a_{RC}	8.16	8.12	6.28	6.27	6.20	5.83
γ_{RC}	−0.88	0.93	4.18	5.39	5.07	6.47
D	2.08	1.66	1.54	0.94	0.77	0.33

One of the most surprising results concerns the characteristic half-thickness of the tail current sheet. In the earlier models TU82 and T87 a quasi-two-dimensional representation of the current sheet was used (see formula (45) in Subsection 2.3.1) and the corresponding parameter D did not show any ordered changes with the increase of the K_p-index, being equal to about ~ 2–$3\ R_E$. However, in the latest T89 version using the improved tail-current model an unexpected monotonic decrease of the current sheet half-thickness was revealed. As can be seen from Table I, the corresponding parameter D falls from $D \approx 2.1$ at $K_p = 0, 0^+$ to $D \approx 0.3$ at $K_p \geq 5^-$. Since the density of the experimental points is relatively small in the vicinity of the current sheet and the latter exhibits a disordered flapping motion as well as substorm-related contractions and expansions, it seems very unlikely that the monotonic decrease of D be revealed from a highly ordered pattern of B_x reversals hidden in the 'noisy' datasets. Much more likely, the main contribution to this effect is made by a considerable decrease of the B_z-com-

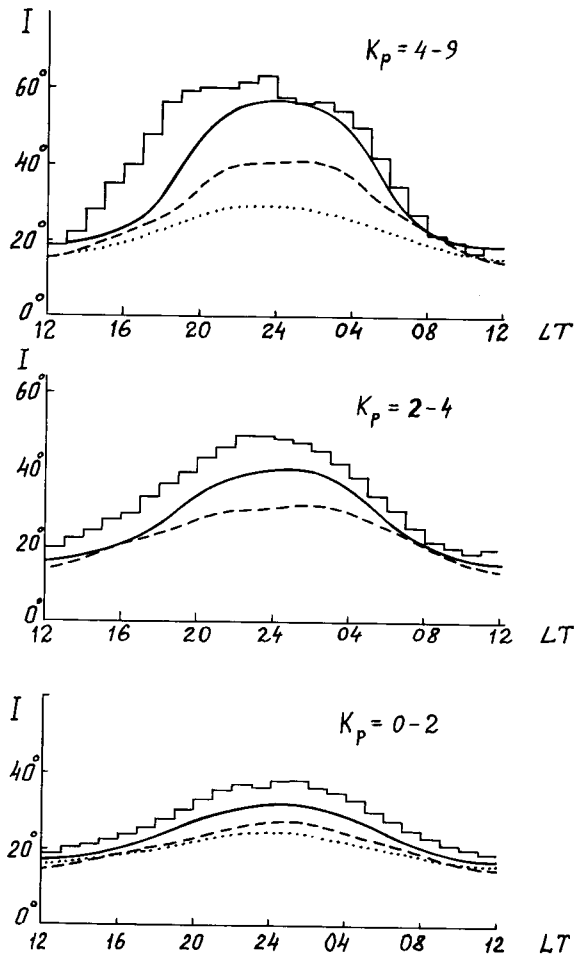

Fig. 41. Comparison of the inclination angles measured by the GOES-2 spacecraft (Lin and Barfield, 1984) with those predicted by three models for different local times. Three panels, from bottom to top, correspond to progressively larger K_p values. The upper histograms in each panel show the average local time distributions of the inclination angle measured by GOES-2. Dotted, broken, and smooth solid lines correspond to Mead and Fairfield (1975), T87, and T89 models, respectively (Tsyganenko, 1989a).

ponent in the inner nightside magnetosphere with growing K_p, since lesser values of D provide a more depressed B_z in the model magnetic field.

It could be concluded from the last statement that the obtained values of D should be considered with care, since they seem to be model-dependent and, hence, may overestimate the effect of the current sheet thinning with growing disturbance level. The most striking thing, however, is that the given values may be, on the contrary, somewhat larger than the real ones. This conclusion is substantiated by Figure 41, which displays the annual mean values of the magnetic field inclination angle measured on board the geosynchronous spacecraft GOES-2 plotted versus the local time for three intervals of the K_p-index. The upper histograms in all three panels show the experimental results

(Lin and Barfield, 1984). Smooth solid lines give the T89 model results, broken lines correspond to the earlier model version T87, and the dotted lines in the upper and lower panels yield the dependence obtained by using the model of Mead and Fairfield (1975). As can be seen in the Figure, the best results are provided by the T89 model. However, there still remain some discrepancies in that all the model plots lie below the experimental histograms. Since the GOES-2 spacecraft location is northward from the dipole equatorial plane, larger inclination angles at the nightside correspond to a more tail-like field structures. Therefore, the discrepancies observed in Figure 41 indicate that in reality the ratio $|B_x/B_z|$ for the total field components is even larger than that given by the models. In other words, actual average values of the current sheet thickness can be even smaller than it follows from Table I, or else we have to admit even larger depression of B_z.

Note that these conclusions refer to the averaged field distributions. In fact, they imply that appearance of the tail-like configurations at $R \sim 6$–$7\ R_E$ in the nightside sector becomes much more probable during disturbed periods. This question has been addressed in detail by Kaufmann (1987) in respect to the problem of physical mechanisms responsible for the re-structuring of the near-tail magnetic configuration observed during a substorm growth phase. Based on a wire-model simulation, he showed that an extremely intense thin current sheet develops at $R \sim 7$–$8\ R_E$ by the end of the growth phase. Tsyganenko (1989b) studied the role of the adiabatic processes in formation of anisotropic plasma distributions necessary for the existence of quasi-static thin current sheets in this region.

We have already raised the question on the account of the dawn-dusk asymmetries in models. Figure 41 provides one more evidence in this connection, which is clearly seen in the upper panel and confirms the earlier observations of a significantly larger inflation of the magnetosphere at the dusk side (Langel and Sweeney, 1971).

The next interesting feature of the electric current distribution revealed from the model calculations is a dramatic increase of the noon–midnight asymmetry of the ring current with growing disturbance level. Table I contains the values of the parameter γ_{RC} defining the difference between the dayside and the nightside estimates of the characteristicds half-thickness of the ring current. This parameter is small and negative for $K_p = 0, 0^+$, but grows rapidly with K_p, attaining $\gamma_{RC} = 6.5$ for $K_p \geq 5^-$. Thus, the effect of concentrating into a thin and intense sheet at the nightside is accompanied by a significant spreading and weakening of the ring current in the daytime sector. This is clearly visible in Figure 19 and agrees with the results by Sugiura (1972) and Roelof (1987) (see Subsection 2.3.3).

A characteristic common feature observed both in T87 and T89 models is a monotonic increase of the magnitude of the current in all the extraterrestrial systems with the K_p-index. As is apparent from Table I, the most pronounced changes occur in the near nightside region; this can be seen from that of the three coefficients c_1, c_2, and c_5, the last one defining the ring current magnitude shows the most dramatic increase yielding a sharp peak of the current density at $x_{GSM} \sim -(6$–$10)\ R_E$.

A degree of the magnetic field line stretching at the nightside can be clearly presented by plotting the Earth intersection latitudes Φ against the corresponding equatorial

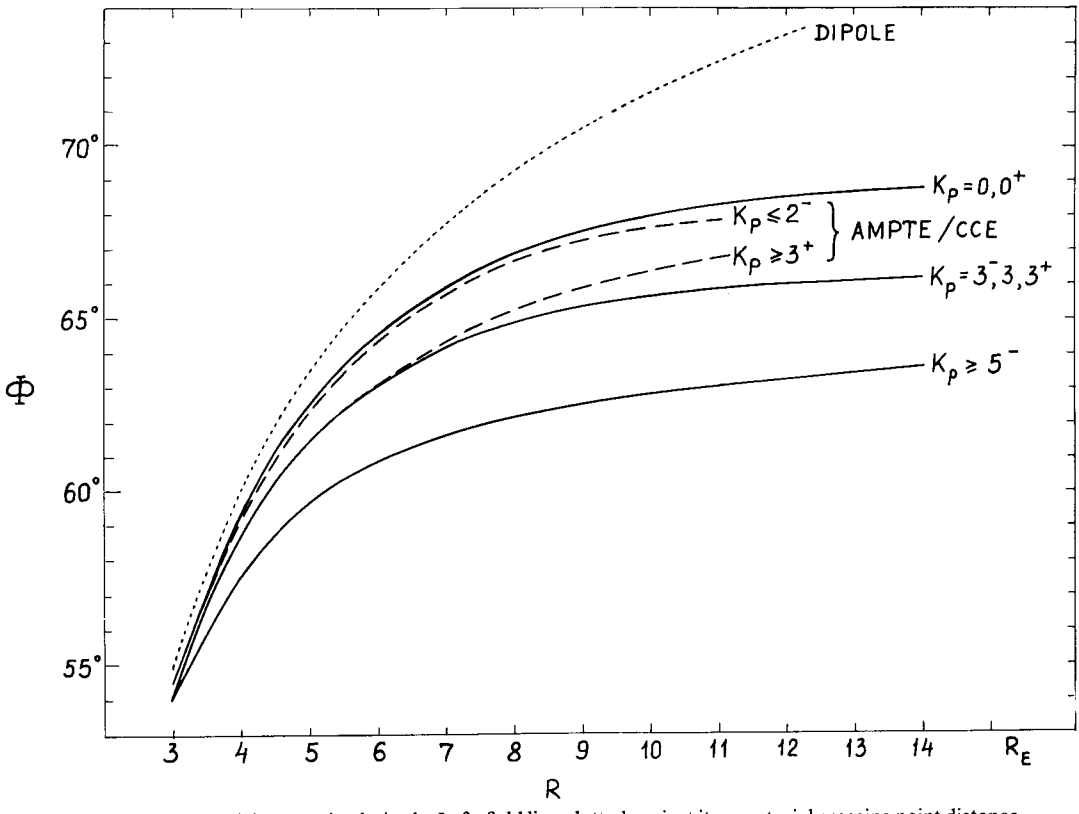

Fig. 42. The Earth intersection latitude Φ of a field line plotted against its equatorial crossing point distance R in the midnight medidian plane, for zero dipole tilt. The plots are given for three variants of the T89 model (solid lines). The broken lines display the result of Fairfield *et al.* (1987) for two K_p intervals. The dotted line corresponds to the purely dipolar field.

crossing distance R. Figure 42 shows three such curves computed by using the T89 model (solid lines) for three K_p levels together with two plots obtained by means of equating the magnetic fluxes calculated from the AMPTE/CCE data (Fairfield *et al.*, 1987). As can be seen from the plots, there is a good agreement between the results obtained by the different methods and from different data, provided the disturbance level is not very high. The model curve for $K_p \geq 5^-$ lies significantly lower, indicating a very strong stretching (see Figure 36). It should be reminded once again that this is an average picture. In individual events of intense substorms an instantaneous deformation of the field structure before the break-up onset can be much stronger (Kaufmann, 1987).

The model magnetic field configuration for different longitudinal sectors is illustrated in Figures 43(a) and 43(b) showing the results of mapping the grid of solar magnetic coordinates from the high-latitude part of the Earth surface into the equatorial plane for two extreme ranges of K_p by using the T89 model. The next two plots (Figures 44(a) and 44(b)) show the results of a similar mapping into the cross-section of the magnetotail located at $x_{GSM} = -20\,R_E$. Figures 34–37 and 43–44 provide a sufficiently detailed

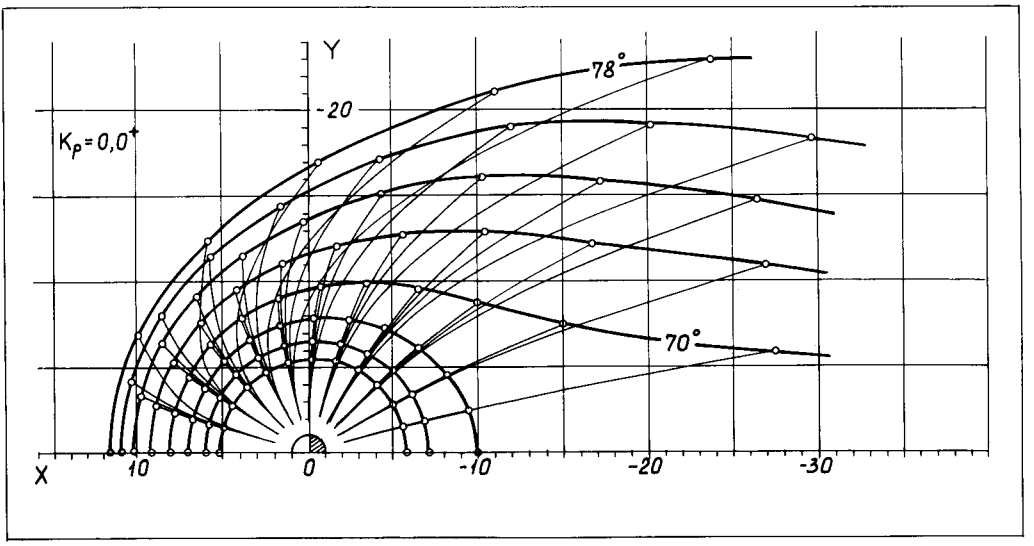

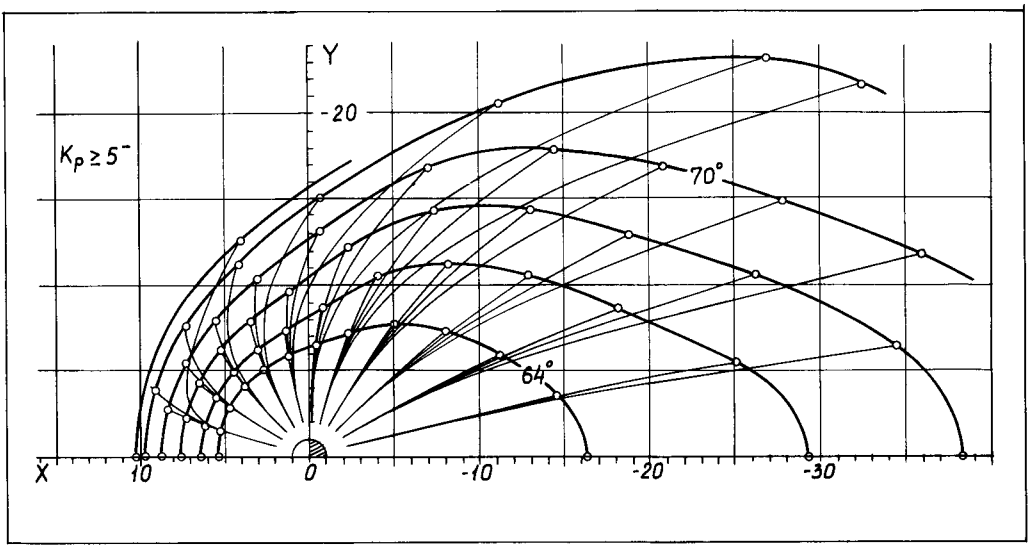

Fig. 43a–b. T89 model magnetic field lines starting from the Earth's surface at circles of constant geomagnetic latitude (beginning from 64°, two degrees apart) at different hours of local time, projected onto the $X - Y$ plane in GSM coordinates. Heavy solid lines in the equatorial plane correspond to constant latitudes of the field line footpoints. (a) The most quiet variant with $K_p = 0, 0^+$; (b) the most disturbed variant with $K_p \geq 5^-$.

description of the model field structure and can be used for mapping various magnetospheric features and boundaries to ionospheric level or *vice versa* (Stern and Alekseev, 1988).

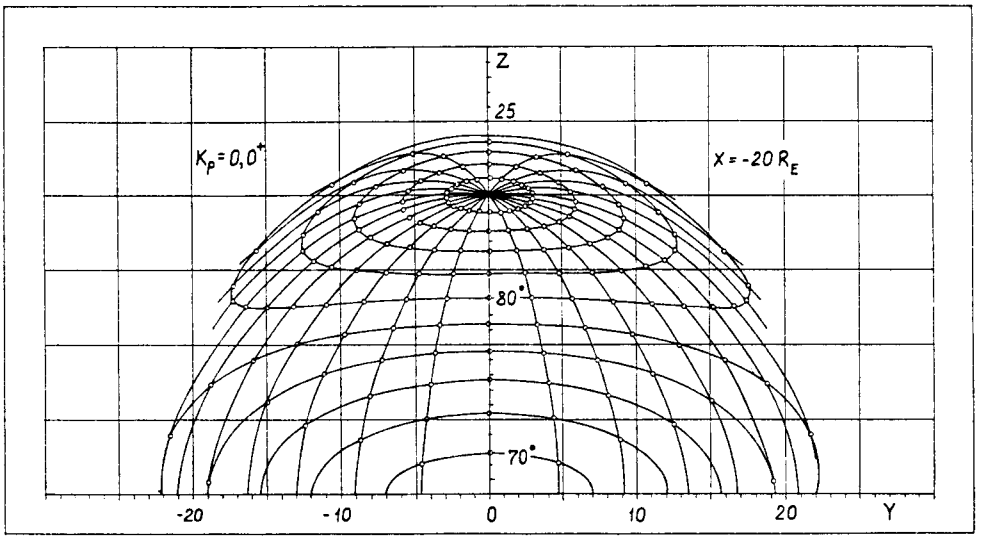

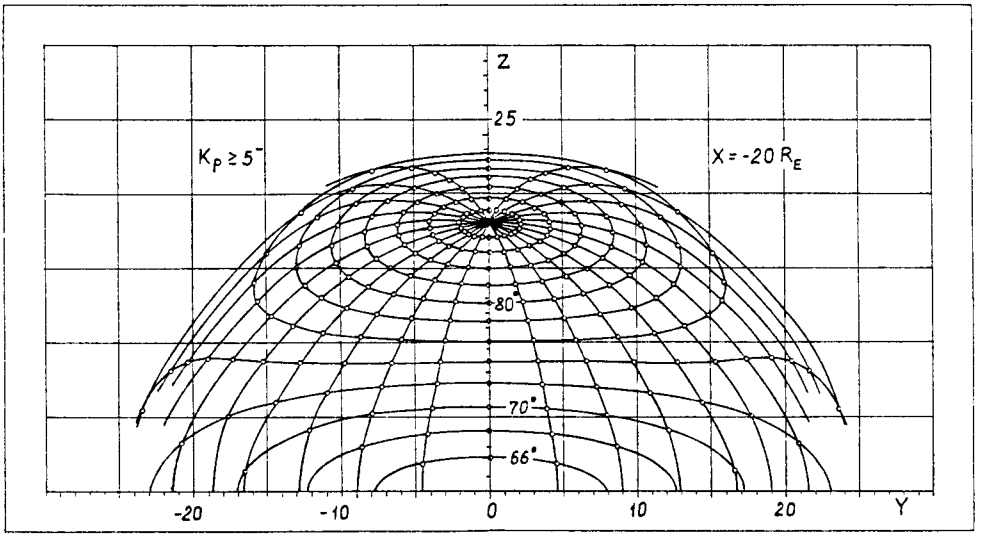

Fig. 44a–b. Geomagnetic latitude–local time grid (two degrees by one hour MLT) mapped from the Earth's surface onto the magnetotail cross-section plane $X_{GSM} = -20\,R_E$ by using the T89 model with $\psi = 0$: (a) $K_p = 0, 0^+$; (b) $K_p \geq 5^-$.

3.2. Modeling the Influence of the Interplanetary Medium State

Having supplied the modeling database by a complementary information on the interplanetary medium parameters it is possible to study the average effects of the solar wind state in the structure of the model magnetospheric field. From a theoretical point of view, a basic difficulty consists in that the physical mechanisms of the magnetospheric reaction to the external influence are very complex. On one hand, there exist significant inertia effects manifested in a temporal delay in the response of the magnetosphere to changes in the solar wind. Moreover, this response is believed to have an integral character related to the processes of a gradual storing and an explosive dissipation of energy, so that the current state of the whole system largely depends on its prehistory. On the other hand, there exist a considerable evidence that the directly-driven mode is also very important. Also there are effects that can be interpreted as an indication of a differential mode of response, in which the rate of change of an external factor plays a dominant role (Rostoker *et al.*, 1988). In this connection, it is no wonder that sorting out the data in the K_p-index intervals, in spite of all its drawbacks, can lead to a significantly better ordering of results. Indeed, the ground-based indices reflect to a certain degree the actual state of the magnetosphere, while the simultaneously measured solar wind parameters in many cases can determine no more than a general tendency of its change.

From a practical point of view, studying the effects of the solar wind in the framework of the statistical modeling is largely hindered at present by comparatively restricted amounts of available magnetospheric data, as well as by numerous gaps in the interplanetary medium databases. Thus, only $\approx 55\%$ and $\approx 46\%$ of the data points used in generating the T87 and the T89 model coefficients are supplied by the corresponding information on the IMF components and the solar wind velocity, respectively. For these reasons, only the most fundamental effects can be resolved as yet in the models based on the existing datasets. Figure 45 shows two magnetospheric configurations computed for two T87 model variants corresponding to the northward (a) and southward (b) orientations of the IMF. In both cases additional restrictions $|B_y^{\mathrm{IMF}}| < 3$ nT and $|B_z^{\mathrm{IMF}}| > 4$ nT were imposed, in order to rule out B_y-related effects and to stress the difference between the two cases considered. Even a cursory inspection of the two plots reveals a conspicuous re-distribution of the magnetic flux between the dayside sector and tail lobes. In the case with $B_z^{\mathrm{IMF}} \geq 4$ nT (a) the last closed line at the dayside has the footpoint latitude $\varphi_c \approx 79.5°$, while in the second case (b) with $B_z^{\mathrm{IMF}} < -4$ nT the 'peeling-off' the dayside magnetic flux results in an equatorward displacement of the polar cusps to $\varphi_c \approx 73.5°$. As noted in Subsection 2.3.2, the most likely source of the field re-structuring is Birkeland current system. Additional contribution to this effect can be provided by the ring current intensification during strong storms. A quantitative study of this question was done by Stern (1985), who showed that the corresponding change in φ_c does not exceed several tenths of degree, provided the magnetic moment M_{RC} of the model ring current is assumed to be constant. Larger equatorward shift of the cusps can be obtained by assuming constancy of the ring current radius and varying its

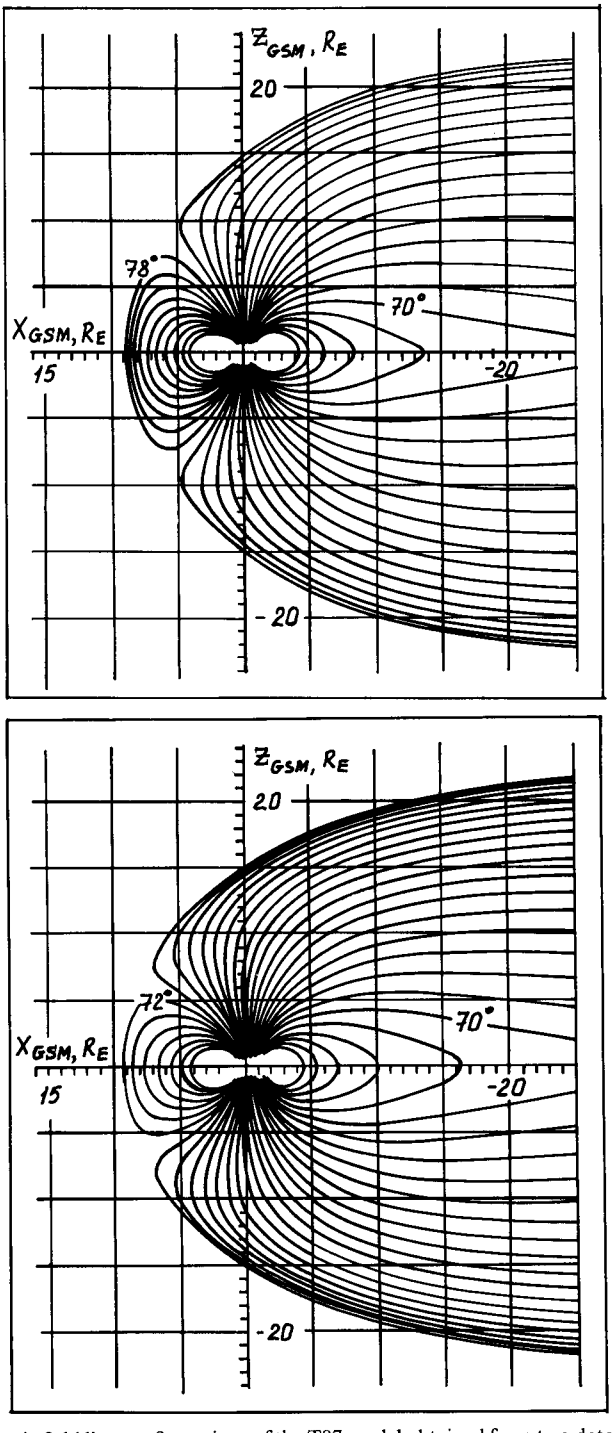

Fig. 45a–b. Magnetic field line configurations of the T87 model obtained from two datasets corresponding to two opposite polarities of the IMF north–south components: (a) $B_z^{IMF} \geq 4$ nT, (b) $B_z^{IMF} < -4$ nT. In both cases $|B_y^{IMF}| < 3$ nT (Tsyganenko, 1987a).

intensity. According to Stern (1985), this yields a 3–4° decrease in φ_c for an order-of-magnitude increase in B_0 (see Equations (68)–(69)) from -20 nT to -200 nT. However, the latter value yields $M_{RC} \sim 2\,M_E$, which is quite an unrealistic value. Here again, the obtained cusp displacements are significantly lower than the observed ones. According to Meng (1982), a typical equatorward jump of the cusps can be as large as ten degrees of latitude at ionospheric heights, while in some individual events record displacements up to geomagnetic latitudes of $\sim 62°$ were also detected. The next strong argument is that the development of an intense ring current is observed, as a rule, significantly later than the equatorward displacement of the cusps, the latter being well correlated with the *AE*-index and B_z^{IMF}, rather than with *Dst*. In this relation, Stern (1985) considered the effect of a partial 'transparency' of the magnetopause with respect to the incident magnetic flux by using a simple modification of the paraboloid model in the spirit of Voigt's (1981) approach described in Subsection 2.2.2.3. According to this study, a 25% transparency yields a 4–5° decrease in φ_c.

Tsyganenko (1988) quantitatively studied the contribution of the field-aligned currents to the observed effects of the polar cusp displacement using the explicit model described in Subsection 2.3.2. That representation was incorporated in the T87 model and the field line tracing was done assuming the net current magnitudes in the systems I and II sheets to be $J_1 = 2 \times 10^6$ A and $J_2 = 10^6$ A, respectively. The 'switching on' Birkeland current circuits resulted in a shift of the model cusps from $\varphi_c \approx 78.5°$ to $\approx 76.0°$. A four-fold increase of the total current in both systems (which is quite realistic for strongly disturbed conditions, see Bythrow *et al.*, 1983) yielded $\varphi_c \approx 70°$. Bearing in mind that in reality the peaks of the system I current density are localized closer to the midday meridian than they are in the model, the real magnitude of this effect is sure to be considerably larger. Therefore, the dramatic equatorward shifts of the polar cusps reported by Meng (1982) may well be attributed to the effects of Birkeland current intensification.

Turning now to effects of the azimuthal IMF component, it should be noted once again that, due to a limited size of the datasets and noise effects, only principal phenomena are discernible. Tsyganenko and Usmanov (1984) studied B_y^{IMF}-related effects in the dayside magnetospheric field modeled by cubic polynomial expansions including terms asymmetric with respect to the Y_{GSM} coordinate. Two sets were created from the original IMP-HEOS data pool by sorting out the points lying in the daytime sector of solar magnemtic longitudes with $|\lambda_{SM}| \leq 60°$ and by dividing them into two parts corresponding to $B_y^{\mathrm{IMF}} \geq 0$ and $B_y^{\mathrm{IMF}} < 0$. Each of the two final datasets gave a set of model coefficients which were then used for tracing the field lines and determination of the dayside neutral point positions. A background tracing to the ionospheric level yielded values of the longitudinal shift $\Delta\lambda_c$ of the model polar cusp footpoints, with the following results: $\Delta\lambda_c = 7.38°$ for $B_y^{\mathrm{IMF}} \geq 0$ and $\Delta\lambda_c = -4.32$ for $B_y < 0$ (the corresponding latitudes φ_c being equal to 78.54° and 78.74°, respectively). The obtained signs of $\Delta\lambda_c$ agree with those expected from a simple qualitative analysis of the reconnection geometry (Cowley, 1973). Similar results were also reported in a recent work by Crooker *et al.* (1987).

As concerns the nightside region, a local modeling of the average tail configurations was carried out by Tsyganenko (1987b) using the same spacecraft database restricted in this case to points lying in the distance range $-70\,R_E \lesssim X_{\mathrm{GSM}} \lesssim -10\,R_E$ and containing 20778 **B** vector averages. Since only the tail region was considered, the magnetic field was represented in a simple separable divergence-free form

$$\begin{aligned} B_x &= \alpha(x)\beta(y)\gamma'(z_r)\,, \\ B_y &= P\alpha'(x)\gamma'(z_r)\,, \\ B_z &= -\alpha'(x)\,[P+\beta(y)]\,\gamma(z_r)\,, \end{aligned} \tag{71}$$

where α, β, and γ are functions of the solar-magnetospheric coordinates having necessary behaviour and symmetry properties. Thus, the function $\gamma(z_r)$ was adopted in the form

$$\gamma(z_r) = (z_r^2 + D^2)^{1/2} - D\,,$$

where D is a characteristic half-thickness scale of the current sheet and $z_r = z - R_H \sin\psi$ is the z-coordinate measured from the neutral sheet plane which moves about the GSM equatorial plane in response to the geodipole tilting. The functions $\alpha(x)$ and $\beta(y)$ were chosen as

$$\beta(y) = 1 - by^2 \quad \text{and} \quad \alpha(x) = a_0 + a_1 x^{-1} + a_2 x^{-2}\,.$$

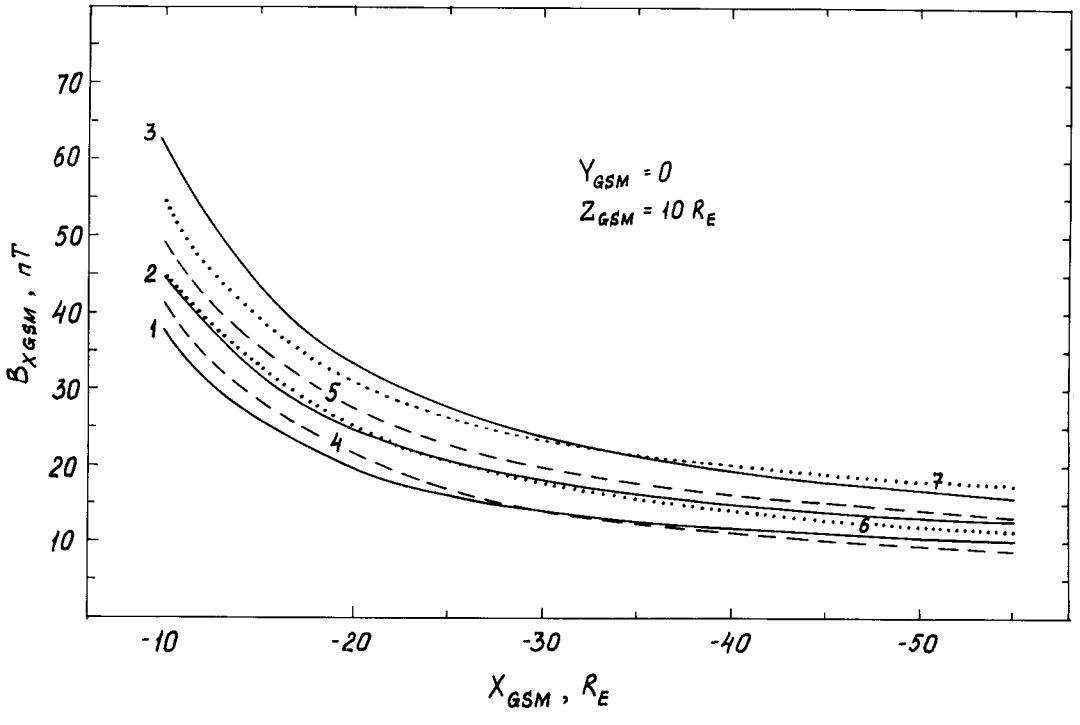

Putting aside all other details, let us turn to results. Figure 46(a) shows distributions of the net B_x-component (including the dipole field) along the line $y = 0$, $z = 10\ R_E$ for $\psi = 0$. Curves 1–3 correspond to three intervals of the K_p-index and show a monotonic increase of the field magnitude with K_p throughout the whole modeling region. Curves 4 and 5 correspond to small ($p_d < 80 \times 10^{-10}$ dynes cm^{-2}) and large ($p_d \geq 250 \times 10^{-10}$ dynes cm^{-2}) ram pressure of the solar wind computed using King's (1977) data on the bulk velocity and density of protons as $p_d = nm_p v^2$ (for $v = 400$ km s^{-1} and $n = 6$ cm^{-3}, $p_d = 160 \times 10^{-10}$ dynes cm^{-2}). To reduce a possible influence of the reconnection effects, an additional constraint $B_z^{IMF} \geq 0$ was imposed in that case. As can be seen, the curve 5 lies by 5–9 nT higher than the curve 4, so that

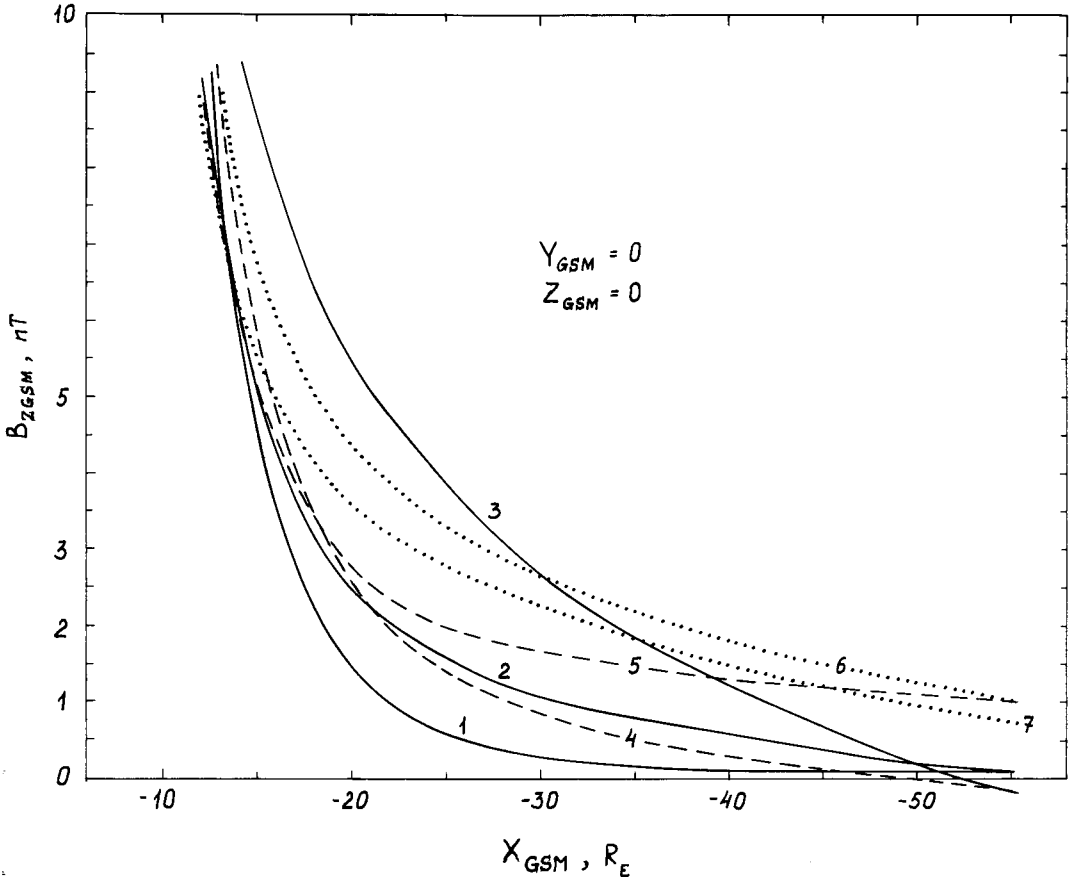

◀▲ Fig. 46a–b. Distribution of two components of the net magnetic field (including geodipole) along the tail as deduced from a local modeling based on the IMP–HEOS dataset. Solid lines 1, 2, and 3 correspond to $K_p = 0, 0^+$, $K_p = 3^-, 3, 3^+$, and $K_p \geq 5^-$, respectively. Broken lines 4 and 5 are for small ($P_d < 80 \times 10^{-10}$ dynes cm^{-2}) and large ($P_d \geq 250 \times 10^{-10}$ dynes cm^{-2}) solar wind ram pressures, respectively. Dotted lines are for two polarities of the azimuthal component of the interplanetary electric field $E_y^{IMF} = v_s B_z^{IMF}/c$, so that the lines 6 and 7 correspond to $E_y^{IMF} < -2$ mV m^{-1} and $E_y^{IMF} \geq +2$ mV m^{-1}, respectively. (a) B_{XGSM} along the line $Z_{GSM} = 10\ R_E$ and $Y_{GSM} = 0$. (b) B_{ZGSM} along the X_{GSM} axis (Tsyganenko, 1987b).

at $x = -10\,R_E$ and at $x = -70\,R_E$ the model tail lobe field changes by factors of 1.2 and 1.5, respectively. Taking into account that the corresponding average values of p_d over the two datasets are 58×10^{-10} and 406×10^{-10} dynes cm^{-2}, i.e., differ by a factor of 7, the obtained response of the tail field seems to be somewhat underestimated. In this relation it is worth mentioning a result by Caan *et al.* (1973) based also on a statistical analysis of the satellite data and having related the tail lobe magnetic pressure with p_d by means of a regression formula

$$B^2/8\pi - B_M^2/8\pi = (-830 \pm 280) + (0.16 \pm 0.03)p_d\,,$$

where both pressures are given in units eV cm^{-3} and the reference field B_M is represented by the model of Olson and Pfitzer (1974). At $x = -15\,R_E$ this relation yields a nearly twofold increase of the lobe magnetic field for the above given values of p_d. What is the reason for the disagreement remains yet unclear, so that a more complete study is necessary.

Figure 46(b) shows in the similar format the distributions of the transversal component of the net model field along the X_{GSM} axis. Almost in the whole range of distances the B_z-component profiles raise upward with growing K_p-index. This is consistent with the above discussed results of the 'global' modeling, in which a decrease of B_z with K_p was found only at rather close distances with $X_{\mathrm{GSM}} \gtrsim -10$–$15\,R_E$.

Using that model, Tsyganenko (1987b) was able to resolve some effects related to the influence of the azimuthal component of the IMF upon the tail structure. Cowley (1981) pointed out a possibility of a twisting of the tail plasma sheet due to asymmetric reconnection geometry for $B_y^{\mathrm{IMF}} \neq 0$ resulting in the violation of the stress balance. The expected rotation of the sheet must be clockwise (as viewed from the tail to the Earth) for $B_y^{\mathrm{IMF}} > 0$ and counterclockwise for $B_y^{\mathrm{IMF}} < 0$ (Figure 47(a)). This hypothesis was verified on the basis of the same dataset for two ranges of X_{GSM}, $-70 \leq X \leq -35\,R_E$ and $-35 \leq X \leq -25\,R_E$. In each region the tail field was modeled by functions similar to (71). However, in this case the coordinates y and z as well as the components B_y and B_z were transformed assuming a rotation of the sheet plane by an unknown angle $\Delta\varphi$ about the X_{GSM} axis combined with a displacement of the sheet by Δy in the dawndusk direction. The quantities $\Delta\varphi$ and Δy were treated as additional nonlinear free parameters to be determined from the spacecraft datasets. Two subsets were created corresponding to $B_y^{\mathrm{IMF}} < -4$ nT and $B_y^{\mathrm{IMF}} \geq 4$ nT, for each of the two intervals of X_{GSM}. The results are displayed in Figure 47(b), where the broken lines mark the position of the current sheet central plane in projection onto the tail cross-section. It is clearly seen that the rotation of the current sheet of expected sign is indeed present in the modeling results. The observed twisting is not strong, so that the rotation angles with respect to the GSM equatorial plane do not exceed $\sim 12°$; nevertheless, they are resolved with a relatively small errors. Also the effect clearly increases with distance, in agreement with the expected qualitative picture sketched in Figure 47(a) and confirmed by observations by Sibeck *et al.* (1985).

One more IMF-related effect is a partial penetration of B_y^{IMF} component inside the magnetosphere (e.g., Nagai, 1987, and references therein). Lui (1983) and Sergeev

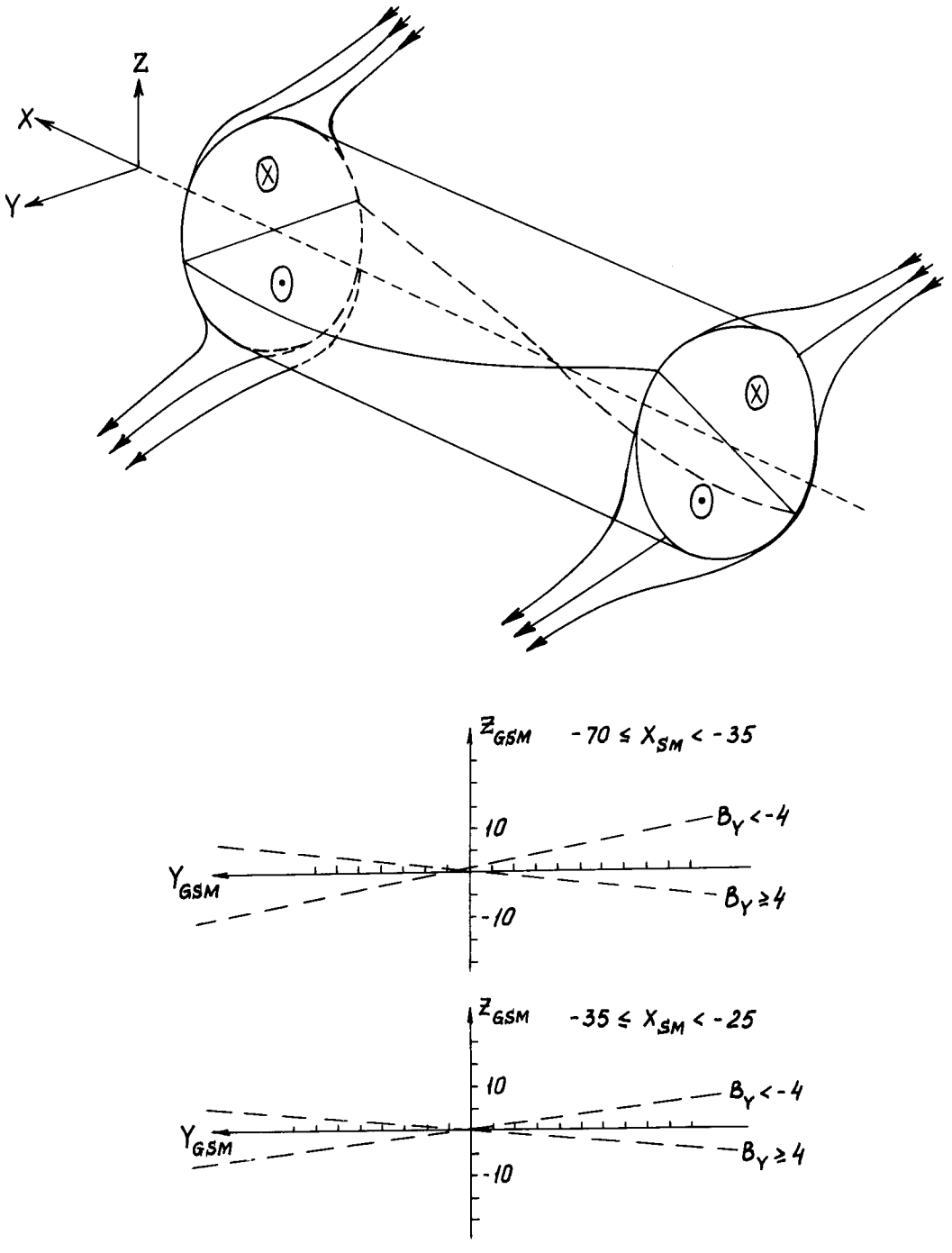

Fig. 47. Effect of the tail plasma sheet twisting indices by the IMF B_y-component: (a) a sketch from Cowley (1981), (b) rotation of the central plane of the tail current sheet obtained in a model study using the IMP–HEOS spacecraft datasets, for two intervals of the tailward distance (Tsyganenko, 1987b).

(1987) based on IMP-6 and ISEE-1 data, respectively, made statistical analyses of this phenomenon for the middle region of the magnetotail within $R \lesssim 30\ R_E$. It was shown that about $\sim 60\%$ of the B_y^{IMF} is observed inside the plasma sheet, while in the lobes the penetration efficiency is much lower. Tsyganenko (1987b) made a modeling study of this effect using the IMP-HEOS database. The model expression for B_y in (71) was complemented by the additional term

$$\Delta B_y = B_1 + B_2 x^{-1} + (B_3 + B_4 x^{-1})\,[(z_r^2 + L^2)^{1/2} - L] \tag{72}$$

containing four coefficients B_1–B_4 and one nonlinear parameter L defining the scale length of the penetrating field distribution in the z-direction. Computations were done for two data subsets corresponding to $B_y^{IMF} \geq 4$ nT and $B_y^{IMF} < -4$ nT. Table II gives the values of ΔB_y induced by the IMF inside the tail at $X = -20 R_E$ and at $X = -40\ R_E$ in the centre of the plasma sheet ($z_r = 0$) and in the lobe region ($z_r = 10\ R_E$). In all cases considered the effect of penetration is clearly seen. Note also that in three cases of the four the values of ΔB_y are significantly higher in the plasma sheet than in the lobe region, in line with the results of Lui (1983) and Sergeev (1987).

TABLE II

Values of the B_y-component pervading in the magnetotail from the solar wind, as deduced from the local modeling study based on spacecraft data. X- and Z-coordinates correspond to the GSM system (Tsyganenko, 1987b)

B_y^{IMF}	$X = -20$		$X = -40$	
	$Z = 0$	$Z = 10$	$Z = 0$	$Z = 10$
< -4 nT	−2.0	−1n4	−1.3	−0.3
$\geq +4$ nT	2.0	0.4	0.3	0.7

Hilmer and Voigt (1987) and Voigt and Hilmer (1987) developed a magnetohydrostatic model of the plasma sheet, in which the observed enhancement of B_y in the central plasma sheet is an intrinsic feature of a two-dimensional self-consistent configuration satisfying the equation of the stress balance

$$\frac{1}{c}\,\mathbf{j} \times \mathbf{B} = \nabla p \tag{73}$$

together with Maxwell equations

$$\nabla \times \mathbf{B} = (4\pi/c)\mathbf{j}\,, \qquad \nabla \cdot \mathbf{B} = 0\,.$$

By introducing the flux function $A(x, z)$, the field components read

$$B_x = -\partial A/\partial z\,, \qquad B_y = I(A)\,, \qquad B_z = \partial A/\partial x\,.$$

Here B_y is chosen as an arbitrary function of A, which ensures the isotropic pressure p to be independent of y. In such a case (73) takes the form of nonlinear Grad–Shafranov

equation

$$\Delta A + \frac{\mathrm{d}}{\mathrm{d}A}\left[4\pi p + \tfrac{1}{2}I(A)^2\right] = 0\,,$$

which under assumptions

$$p(A) = \frac{1}{8\pi}K^2A^2 \quad \text{and} \quad I(A)^2 = \alpha^2A^2 + B_{yc}^2 \tag{74}$$

and with properly defined boundary conditions has simple solutions providing a physically reasonable quantitative representation of the observed structure of the plasma sheet. In particular, for non-zero values of the constant parameters α and B_{yc}, the self-consistent B_y varies with z in such a manner that $|B_y|$ attains its maximal value in the centre of the sheet, while in the lobes it approaches its background value $|B_{yc}|$. The parameter α defines the proportion, in which the background B_y is enhanced within the plasma sheet and thus determines the intensity of the field-aligned currents flowing parallel to the tail axis and changing their direction with the sign of z. From a formal point of view, the field-aligned currents arise in this model as an implication of the pressure balance requirement. However, as stressed by Hilmer and Voigt (1987), this approach *per se* provides no explanation of how these currents are related to the IMF and what is the physical reason for the observed pervading of B_y^{IMF} in the tail. Some hypothetical mechanisms relevant to the problem as well as general limitations of the magnetohydrostatic models are also discussed by Hilmer and Voigt (1987).

In this connection a work by Voigt and Wolf (1985) should also be noted, in which they addressed an interesting aspect of the problem of polar cusp position. In their simple two-dimensional model magnetosphere (Figure 48) a dipolar field is confined within a rectangular semi-infinite cavity and is in the hydrostatic equilibrium with isotropic plasma distributed in the A-space in accordance with the same quadratic law (74) leading to the linear Grad–Shafranov equation. In this case the B_y-component is absent and the right-hand side of the equation contains a singular term defining the two-dimensional dipole source

$$\Delta A + K^2A = -M_D\frac{\partial}{\partial X}\delta(x)\delta(y)\,. \tag{75}$$

The solution of (75) satisfying Chapman–Ferraro boundary condition can be obtained as the expansion in eigenfunctions

$$A(x, z) = -(M_D/2)\sum_{n=1}^{\infty}\cos(\alpha_n z)\left[\mathrm{sign}(x)F_n(x) - F_n(x - 2b)\right],$$

where $\alpha_n = (\pi/2)(2n - 1)$ and

$$F_n(x) = \exp(-|\lambda_n X|)\,, \qquad F_n(x) = \cos(\lambda_n X)\,,$$

$$\text{for} \quad K^2 < \alpha_n^2 \quad \text{and} \quad K^2 > \alpha_n^2$$

with $\lambda_n = (|\alpha_n^2 - K^2|)^{1/2}$.

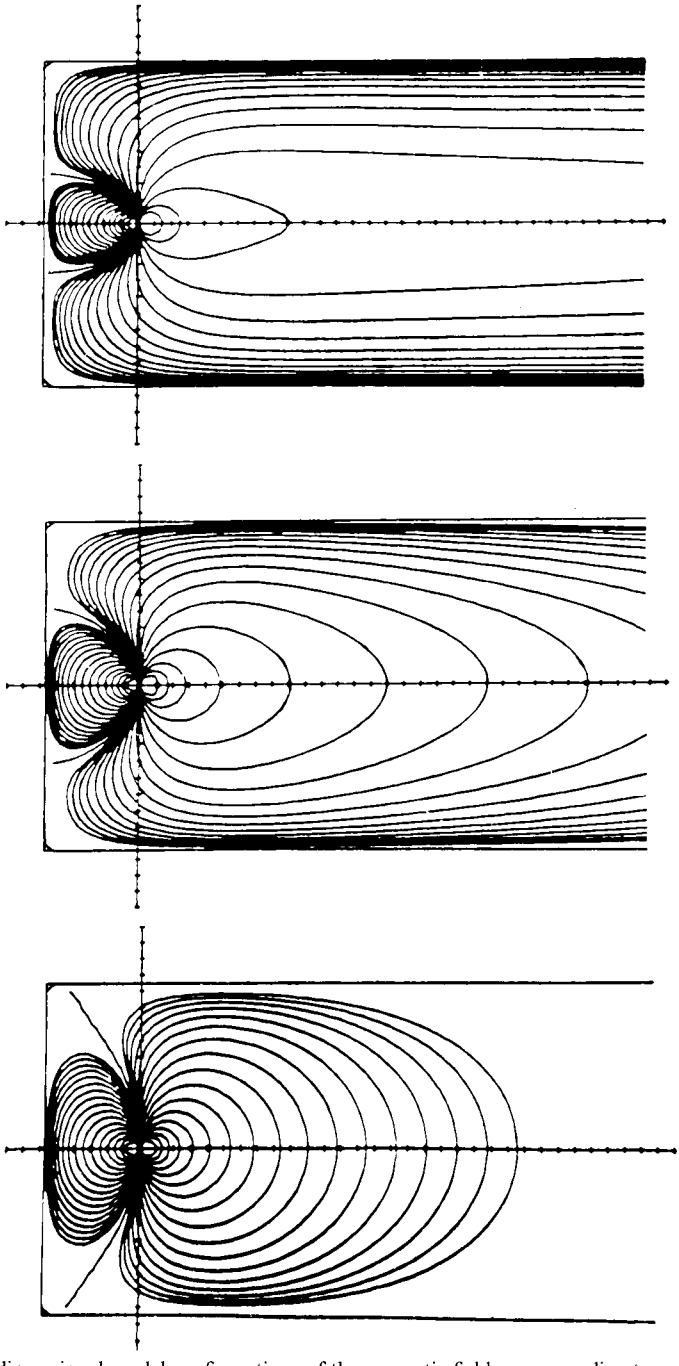

Fig. 48. Two-dimensional model configurations of the magnetic field corresponding to equilibrium solutions of linear Grad–Shafranov equation (75) for three values of the parameter K defining the pressure of the magnetospheric plasma, from vacuum case of $K = 0$ in the top to the critical configuration with $K = \alpha_1$ with the largest stretching of the tail field lines and the lowest dayside cusp latitude in the bottom (Voigt and Wolf, 1985).

For $K = 0$ this yields the vacuum field shown in the top of Figure 48, while the case $K > 0$ corresponds to non-zero currents flowing inside the cavity and inflating the nightside magnetic field. The assumed form (74) of the pressure function implies that the current $j_y = K^2 A$ flows also at the dayside. However, owing to asymmetry in the boundary conditions, the net dayside current is much smaller than that at the nightside, provided $K < \alpha_1$. This results in the increase of the tail lobe magnetic flux and equatorward shift of the polar cusps. For $K = \alpha_1$ the configuration reaches the state with the maximal tail stretching and minimal polar cusp latitude, much resembling the pre-break-up configuration of the real magnetosphere. A further increase of the plasma pressure with $K > \alpha_1$ leads to a tearing of the tail current, which breaks into a filamentary structure corresponding to the oscillatory solutions of (75). The total tail current drops and the cusps retreat poleward.

The work by Voigt and Wolf (1985) sheds some light on the result by Wu (1983), who carried out a resistive MHD simulation of the magnetosphere formation and obtained an unexpected sweeping of the dayside neutral points towards the tail magnetopause region. Based on the above outlined theory, Voigt and Wolf (1985) suggested that Wu's phenomenon is but an artefact of his code implying much too high numerical diffusion and hence too large plasma pressure on the cusp field lines.

3.3. Using the Models in Calculations of the Conjugate Points

Calculation of the conjugate point positions is one of traditional applications of magnetospheric models. For low-latitude points of the Earth's surface the calculations can be done without taking into account the external current systems, since in that case the field lines do not leave the 'sphere of influence' of the internal sources. In practice one can use the conjugate point maps (e.g., Barish and Wiley, 1970) or the tables of the corrected geomagnetic coordinates (Gustafsson, 1970; Tsyganenko, 1979; Allen *et al.*, 1982).

The field lines with the footpoint geomagnetic latitudes larger than $\sim 60°$ are significantly influenced by external sources. Therefore, due to asymmetric position of the sources with respect to the geodipole during periods with sufficiently large tilt angles, a significant variation of the conjugate point location can occur. The amplitude of the shift increases with latitude, which can be seen from the plots in Figure 49 showing the latitudinal (a) and longitudinal (b) displacement of the southern conjugate point caused by the geodipole tilt $\psi = 30°$ (solid lines) and $\psi = -30°$ (broken lines), versus MLT of the northern conjugate point. The families of the plots correspond to several values of the geomagnetic latitude of the northern point and are obtained by using the most quiet ($K_p = 0, 0^+$) variant of the T89 model. The next pair of plots (Figure 50) gives in the same format the results obtained for the most disturbed conditions with $K_p \geq 5^-$. The curves terminating apart of the noon or midnight sides of the panels correspond to high-latitude field lines. In the noon sector these are the tail lobe field lines lying polarward of the cusp, whereas near midgnight these are the lines which close across the current sheet beyond distances $R = 25\,R_E$; the latter lines may be termed as 'quasi-unclosed' ones.

The plots displayed in Figures 49 and 50 exhibit a qualitative resemblance with those obtained in earlier works (e.g., Tsyganenko, 1976). Their most essential features are summarized as follows. (i) For $\psi > 0$ the latitudinal shift is positive at the nightside and negative at the dayside, i.e., southern conjugate points shift poleward during the night MLT hours and equatorward during the daytime. For $\psi < 0$ the sign of this effect is the reverse, which can be seen from that the solid and broken curves are approximately symmetric with respect to horizontal axis. (ii) The absolute values of the latitudinal shifts reach their maxima at noon and midnight. However, the nightside shifts do not exceed $\sim 1°$, while at the dayside they are significantly larger, especially for the lines adjacent to polar cusps. (iii) The longitudinal shifts, as implied by symmetry, are zero at the midday-midnight meridian and reach the maximum during pre-dawn and post-dusk hours, where they can be as high as $\Delta\lambda \sim 10°$ for the auroral zone field lines. (iv) In going from the most quiet to the most disturbed conditions, the shifts $\Delta\varphi$ and $\Delta\lambda$ corresponding to the same pair of conjugate points increase by a factor of 2 to 3.

The shifts of conjugate points for intermediate values of the tilt angle can also be evaluated from the given plots with a good accuracy, taking into account that the quantities $\Delta\varphi$ and $\Delta\lambda$ depend almost linearly on ψ. Note that the internal field in these calculations was considered to be purely dipolar and hence, in accordance with the material of Section 2.1, the variables φ and λ in Figures 49 and 50 should be treated in practical applications as the corrected solar magnetic coordinates. As already noted, this can result in an error of the order of 0.1°–0.3°. If a better accuracy is needed or

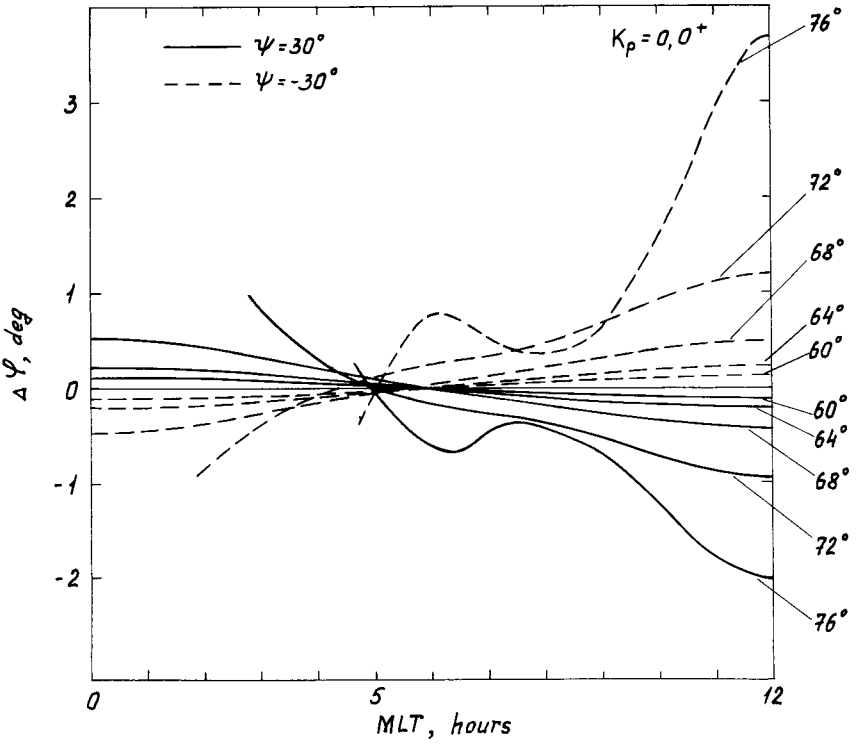

a detailed study of the diurnal and seasonal motion of conjugate points is to be done for a concrete ground-based station, then it can be more convenient to carry out a direct tracing of the field lines by using an appropriate software (e.g., Tsyganenko *et al.*, 1987). An example of such a computation is shown in Figure 51, where two contours represent diurnal traces of the point conjugate to the Antarctic observatory Syowa Base ($\varphi_{GEO} = -69.00$, $\lambda_{GEO} = 39.58$) for the vernal equinox (solid circles) and the summer solstice (open circles). The curves are obtained using the moderately disturbed ($K_p = 3^-, 3, 3^+$) variant of the T89 model. Such calculations were done earlier by Barish and Roederer (1969) and Kosik (1978). Their results are in a qualitative agreement with those shown in Figure 51; quantitative discrepancies are due mainly to limitations inherent to the then available models used by those authors. Ono (1987) used in his study the TU82 model and obtained loop-like traces, which are very close to the above displayed ones.

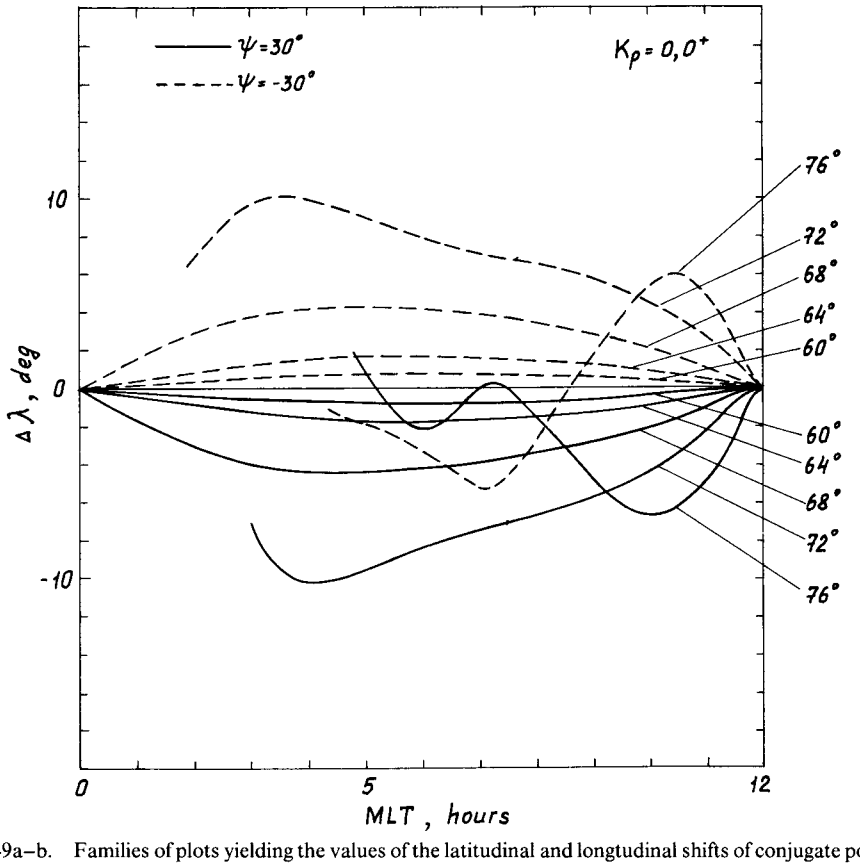

Fig. 49a–b. Families of plots yielding the values of the latitudinal and longtudinal shifts of conjugate points in southern hemisphere for the tilted geodipole ($\psi = \pm 30°$) with respect to their positions in the symmetrical case ($\psi = 0$), versus MLT. The solid and broken lines are for $\psi = 30°$ and $\psi = -30°$, respectively; the curves are labeled by corresponding values of the northern footpoint geomagnetic latitude. The plots are computed by using the T89 external field model for $K_p = 0, 0^+$. (a) Latitudinal shifts $\Delta\varphi$; (b) longitudinal shifts $\Delta\lambda$.

Again, it should be realized that the curves in Figures 49–51 provide but averaged shifts of the conjugate points. Their real positions, together with the whole magnetospheric configuration, depend on the instantaneous state of external current systems which is extremely variable even under quiet conditions.

3.4. Effects of the Geodipole Tilt in Location of Polar Cusps as Deduced from Models and Observations

We have seen from Figures 49(a) and 50(a) that in approaching the noon meridian and in going to higher latitudes the latitudinal shift of conjugate point increases, reaching 1–2 deg by $\varphi \sim 70$–$72°$. Tracing the lines from footpoints located at still higher latitudes makes it possible to investigate the dependence of the latitude φ_c of the last closed dayside field line on the K_p-index and the dipole tilt angle. Figure 52 shows the plots of φ_c versus tilt angle ψ for six variants of the T89 model. Each plot is based on only three values of φ_c corresponding to $\psi = \pm 30°$ and $\psi = 0°$, since in the test computations the dependence was shown to be rather smooth. As can be seen from the figure, the boundary latitude φ_c decreases almost monotonically with K_p for all tilt angles, so that the difference between the extremal variants is about 5–6°. The latitudes φ_c depend almost linearly on ψ and increase by $\sim 4°$ for ψ ranging from $-30°$ to $+30°$. A similar dependence was reported by Burch (1972), who analysed the data on fluxes of the electrons with energies ~ 0.7 keV. A short review of relevant results and a detailed study

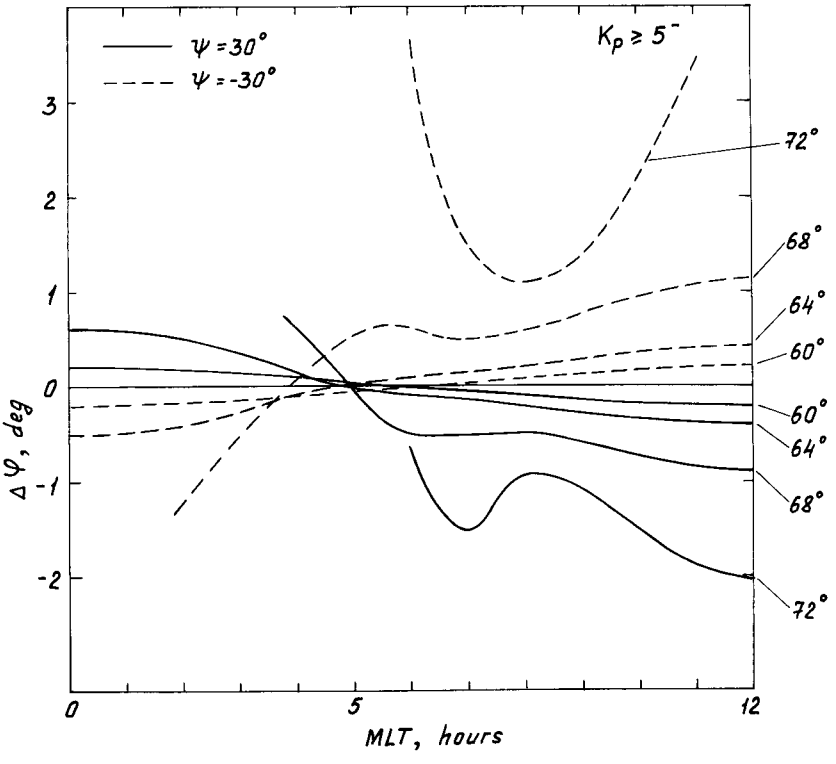

of the polar cusp position based on data from the DMSP F7 spacecraft is done in a recent work by Newell and Meng (1988). In this work, however, no separation of data in accordance with the state of the magnetosphere or the solar wind was made and, therefore, the results should be regarded as average over the whole period. They are shown in Figure 52 by open circles connected by a broken line. The average slope of this dependence is in a satisfactory agreement with that of model plots. However, absolute values of latitudes given by Newell and Meng (1988) yield the best correspondence with the model plots for $3 \leq K_p \leq 4$, whereas the average K_p value over long periods equals 2, so that one should expect the experimental curve to lie by 1–2 deg higher. Apparent reason for that discrepancy is that the open circles in Figure 52, according to Newell and Meng (1988), mark the position of the equatorward boundary of the cusp defined from the characteristic particle fluxes and energies and lying thus at lower latitudes than the separatrix between the dayside and the tail field lines.

Figure 53 displays the corresponding plots of φ_c versus ψ for the Mead–Fairfield (1975) model. On the whole, the same behaviour is revealed in the model plots, as in Figure 52. However, owing to a somewhat different way of defining the K_p-index intervals, the plots are grouped in pairs. Besides that, significantly different slopes for

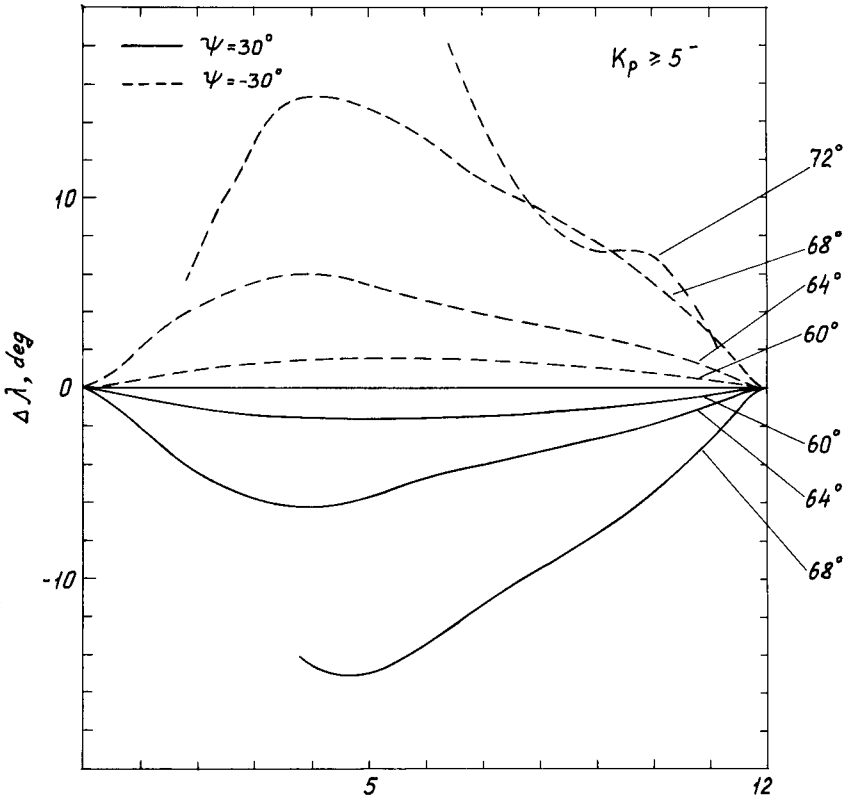

◀ ▲ Fig. 50a–b. Same as Figure 49, except for $K_p \geq 5^-$.

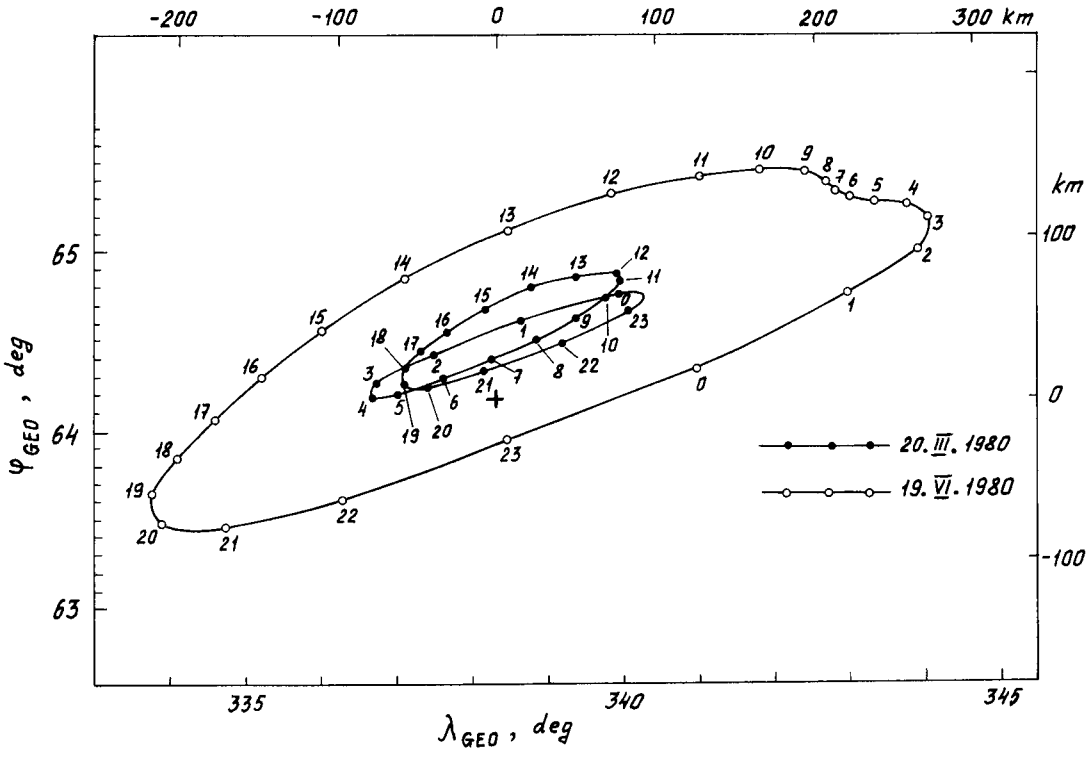

Fig. 51. Diurnal paths of the point conjugate to the Antarctic observatory Syowa Base for vernal equinox (solid circles) and summer solstice (open circles) computed by using the T89 model for $K_p = 3^-, 3, 3^+$. The points are labeled by the values of UT hours and the cross marks the location of the Iceland Observatory Leirvogur.

$\psi < 0$ and $\psi > 0$ are conspicuous in all four plots. A more detailed study showed that this is due to the penetration of a narrow field line bundle from the cusp region outside the magnetosphere for $\psi \neq 0$ which is visible in Figure 16. This drawback is more or less inherent to all the models, in which no special measures are taken to minimize the magnetic flux escaping across the magnetopause. The T89 model does not represent an exception in this sense, which can be seen in Figure 52. Indeed, the plots for $K_p = 1^-, 1, 1^+$ and for $K_p \geq 5^-$ yield a significantly lesser slope for $\psi > 0$ than other ones; as the line tracing has shown, just in the two cases the effect of the magnetic flux 'leakage' appears to be the most pronounced.

4. Indirect Methods for Testing the Field Models Using the Magnetospheric Plasma Measurements

A vast amount of experimental data on spatial, pitch-angle, and energy distribution of the magnetospheric plasma particles is an abundant source of information which can supplement the magnetic measurements in testing and refining the field models. The

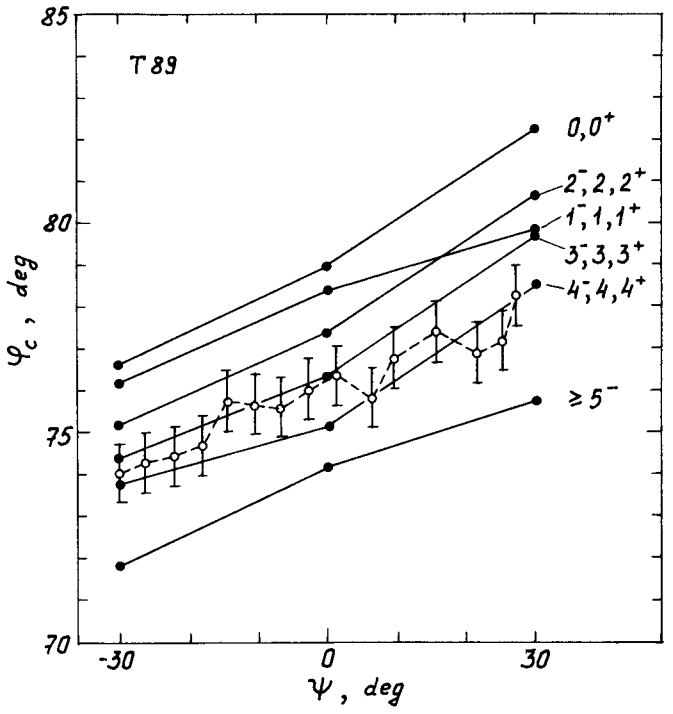

Fig. 52. Latitude of the northern footpoint of the last closed dayside field line φ_c plotted against the geodipole tilt angle ψ, for six variants of the T89 model (solid circles). Open circles display the average positon of the equatorial boundary of the polar cusp as deduced by Newell and Meng (1988) from particle measurements.

magnetosphere is mostly in a state of quasi-static equilibrium which is violated only during periods of the explosive activity. The steady-state configurations imply an approximate balance between the mechanical stresses due to plasma pressure gradients and/or anisotropies and Ampère's force. This provides a possibility for testing empirical models using the information on plasma characteristics partly available from experiments and complemented by some theoretical principles. On the other hand, much knowledge on the magnetic field structure can be provided by the data on the energetic particles which make a negligible contribution to the net plasma pressure and can serve as a remote testing probe due to their low sensitivity to electric fields.

Walker and Southwood (1982) tested four of then available models having assumed the isotropy of the plasma pressure in the modeling region. The latter hypothesis can be substantiated by results of Stiles *et al.* (1978), who evaluated from their measurements the quiet plasma sheet anisotropies and showed the ratios $p_{\parallel}/p_{\perp}$ to be close to unity. In this case the stress balance equation reduces to (73) and, therefore,

$$\nabla \times (\mathbf{J} \times \mathbf{B}) = 0 . \tag{76}$$

Numerical calculations of the left-hand side of (76) by using the models of Olson and Pfitzer (1977), Hedgecock and Thomas (1979), Tsyganenko (1976, 1979), and the tail

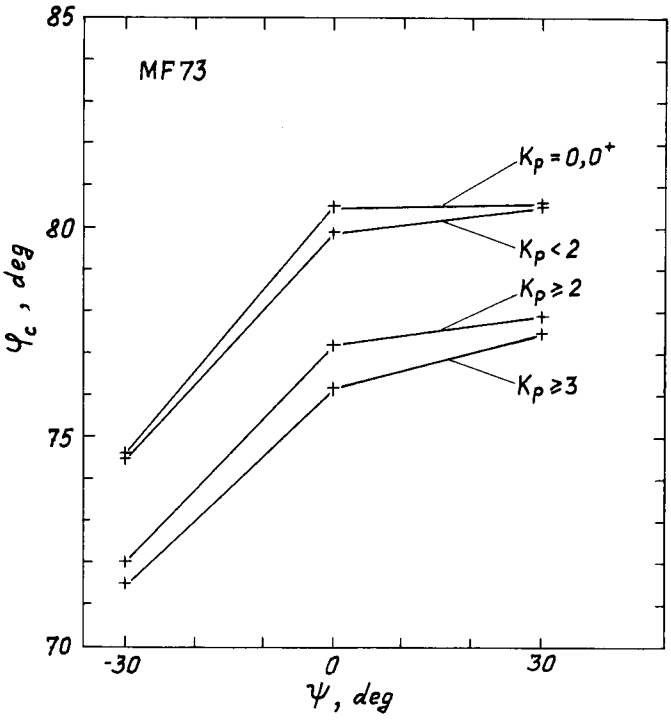

Fig. 53. Plots similar to those in Figure 52 obtained by using the model of Mead and Fairfield (1975).

field model of Beard (1979) showed that none of them satisfy the criterion of stress balance.

Spence *et al.* (1987) considered a more general problem. They suggested a method which enables one to determine a distribution of the anisotropic plasma confined within the given model magnetic field and consistent with the generalized stress balance condition

$$\nabla \cdot \hat{\mathbf{P}} = (1/c)\mathbf{J} \times \mathbf{B} = \left(\frac{1}{4\pi}\right)(\nabla \times \mathbf{B}) \times \mathbf{B}, \tag{77}$$

where

$$\hat{P} = p_\perp \hat{\mathbf{I}} + (p_\parallel - p_\perp)B^{-2}\mathbf{BB} \tag{78}$$

is the pressure tensor. The right-hand side of (77) is fully defined by the field model and the problem is to find an appropriate distribution of $p_\parallel$ and $p_\perp$. In general, there exist an infinite set of solutions so that the task becomes feasible only on specifying a concerete form of the particle distribution function. Spence *et al.* (1987) have chosen bi-Maxwellian distribution which, combined with Liouville's theorem and with the conservation of the particle energy and magnetic moment, leads to a simple dependence of $p_\parallel$ and $p_\perp$ on the magnetic field intensity along a given field line tube. Under these assumptions, the problem has a family of solutions parametrized by values of the perpendicular pressure $p_\perp$ at a given point of the equatorial plane. This 'inversion'

method was applied by Spence *et al.* (1987) for testing the TU82 model. It was shown that with reasonable initial values of $p_\perp$ at $X_{GSM} = -6.5\ R_E$ the reconstructed pressure distributions appeared to be practically isotropic in the whole modeling region ($-12 \leq X_{GSM} \leq -6.5\ R_E$), in accordance with the results of Stiles *et al.* (1978). Thus, the principal contribution to the plasma sheet current comes from the isotropic part of the pressure tensor (78) entering the gradient term in Equation (77). As shown by Spence *et al.* (1987), the magnitude of this pressure gradient consistent with the TU82 model magnetic field agrees well with the AMPTE/CCE particle measurements.

There exist one more aspect of the problem of compatibility of the magnetic field models with the plasma distribution, which concerns the question on the possibility of a stationary plasma convection in the tail. Several authors (Tsyganenko, 1975b; Kropotkin, 1977; Yamamoto and Tamao, 1978; Tsyganenko, 1982b) considered the evolution of particle distributions caused by the Earthward convection of the plasma from the far tail region where its injection from the mantle under the action of the large-scale electric field (Pilipp and Morfill, 1978) was assumed. It was shown that the observed earthward gradient of the plasma temperature and density can be explained by a combined effect of particle energization due to the transverse magnetic drift in the dawn-dusk electric field and the corresponding decrease of the volume of convecting magnetic field line tubes. Assuming the conservation of the first two adiabatic invariants (which imposes both upper and lower limits on the particle energy) one can interpret this process in terms of the betatron and Fermi acceleration. In the opposite case of a nonadiabatic motion the particles can be considered to be effectively pitch-angle scattered; in this situation the isotropic pressure can be evaluated from the model by calculating the changes of the field line tube volume, in accordance with the polytropic law $pV^\kappa = \text{const.}$, where $V = \int ds/B(s)$. Calculations showed (Tsyganenko, 1982b) that the two different approaches yield essentially the same quantitative result in what concerns the electric current distribution consistent with the obtained pressure anisotropies and gradients. However, this current distribution provides somewhat larger Earthward gradient of the lobe magnetic field, in comparison with that in the original background model. This inconsistency can be attributed to the neglect of particle losses through the sides of the plasma sheet in the simplified quasi-two-dimensional analysis. Such a possibility was qualitatively discussed by Tsyganenko (1982b), and Kivelson and Spence (1987) carried out a quantitative study of the effect. However, Erickson and Wolf (1980) and Erickson (1984), based on two-dimensional model calculations, put forward a more pessimistic hypothesis of a fundamental nature of the above-mentioned inconsistency between the convection models and the steady-state balance condition. According to this view, the stationary convection is impossible in principle and dynamical disturbances of the whole configuration represent an intrinsic feature of the nightside magnetosphere (see also Schindler and Birn, 1986).

This point of view seems to be a somewhat extremist one and is open to question. Figure 54 (Kivelson and Spence, 1987) shows the plots of the plasma sheet pressure as function of the tailward distance derived from the adiabatic law, wherein the drift losses were also taken into account. The corresponding volumes of field line tubes were

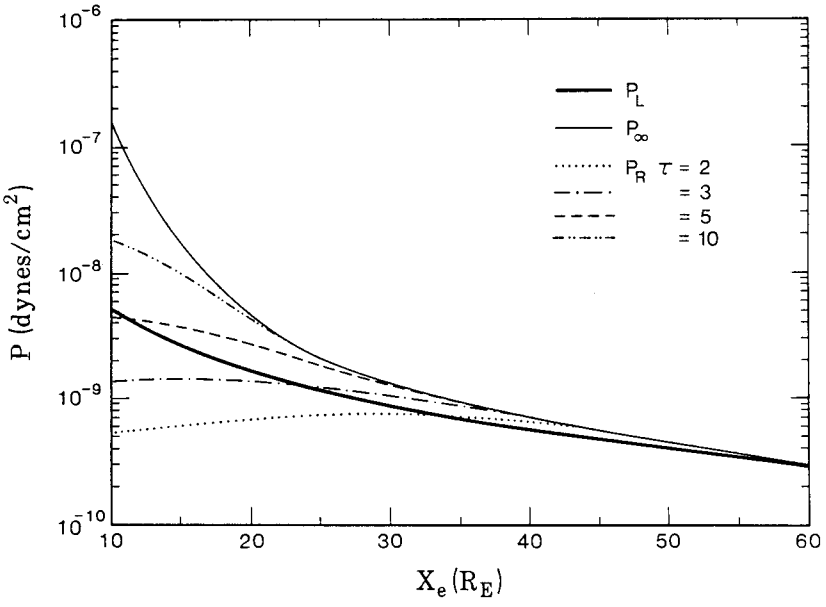

Fig. 54. Plasma sheet pressure versus tailward distance in adiabatic convection models. Thin solid line corresponds to the case of two-dimensional adiabatic compression evaluated by using the T87 model without taking into account particle losses. Introducing the effect of drift losses throughout the plasma sheet flanks leads to a significant decrease of the near-tail pressure gradient (the broken, dasheddotted, and dotted lines). Heavy solid line shows the pressure variation along the tail consistent with the average lobe magnetic field measured by Mihalov *et al.* (1968) (after Kivelson and Spence, 1988).

computed using the T87 model. The solid line having the largest slope at small distances gives the profile for a purely two-dimensional convection, i.e., corresponds to the limiting case of Erickson and Wolf (1980). Broken, dotted, and dashed-dotted lines are plotted for four realistic values of the parameter $\tau = qER/kT_0$ which defines the efficiency of losses by specifying the ratio of the cross-tail potential $2ER$ to the initial thermal energy of particles. It is clear from this result that taking into account the effect of drift losses inserts a significant correction in the pressure profiles and hence is capable of settling the above controversy.

A strong argument in favour of the possibility of the stationary convection in the tail is advanced by its direct observations reported recently by Sergeev and Lennartsson (1988). Having used a set of the ground-based observations, the solar wind data, and measurements on board the ISEE-1 spacecraft, they were able to find four cases of a very prolonged (up to 10 hours) stable convection in the plasma sheet, which took place during a period with a negative B_z^{IMF} component and in the almost complete absence of the ground substorm activity. The observed stationary convection was shown to have several interesting features which shed light on the above mentioned difficulties of the two-dimensional theory. Namely, the convection was shown to be essentially non-uniform across the tail, with the formation of a 'convection jet' in the central tail region where both the B_z-component of the magnetic field and the convection electric field E_y

significantly (by a factor of 2–3) exceed the average values. It was also found that the convection streamlines tend to decline in the dawn-dusk direction on approaching the Earth. This effect can be considered as a manifestation of three-dimensional pattern of the convection, which can remove the inconsistencies inherent to two-dimensional models. It should be noted that an intrinsic feature of this concept is the system of field-aligned currents flowing Earthward in the dawn boundary plasma sheet and tailward at the dusk side. They induce the non-uniformity of B_z and E_y in the tail cross-section and bring the magnetospheric convection pattern in correspondence with that observed at ionospheric heights (Heelis and Hanson, 1980).

In proceeding to the works on energetic particles, it should be noted that still in early studies (e.g., Williams and Mead, 1965; see also a review paper and a book by Roederer, 1969, 1970) many important questions related to this component were addressed which are the quasi-trapping regions, the drift shell splitting, the non-adiabatic pitch-angle scattering (Taylor and Hastie, 1971), etc. Many authors (Sibeck *et al.*, 1987, and references therein) studied the pitch-angle distributions in the near magnetosphere. Their results indicate that at least under quiet conditions the main observed features show a good agreement with the drift theory in conjunction with a realistic magnetic field model. A considerable progress was achieved also in studies of the solar particle access to the Earth's inner magnetosphere and the polar caps by means of a numerical tracing their paths in model magnetospheres (see reviews by Morfill and Scholer, 1973; Morfill, 1975; Scholer, 1975; and Schulz, 1980).

West *et al.* (1978a, b) gave a convincing example of great possibilities of using data on the pitch angle distributions for monitoring the instantaneous magnetic configuration in the near tail. It is assumed in this method that particles with energies larger than a critical value corresponding to the breakdown of adiabaticity exhibit a strong pitch-angle scattering on traversing the tail current sheet (Wagner *et al.*, 1979; Gray and Lee, 1982), leading to a fully isotropic velocity distribution at these energies. The latter hypothesis is intuitively evident; its quantitative substantiation was given in papers by Tsyganenko (1982a), Wright (1985), and Basu and Rowlands (1986). The principal result is that for the values of the dimensionless parameter $K = R_c/\rho_L$ lesser than ~ 8 (Alfvén and Fälthammar, 1963) the amplitude of the pitch-angle scattering of a particle entering the current sheet increases abruptly, so that the pitch angle distribution in the field line tube becomes fully isotropic not later than in a few bounce periods. Assuming the curvature radius R_c of the field line to be minimal in the centre of the sheet and rewriting the particle gyroradius ρ_L in terms of its velocity, mass, electric charge, and the local magnetic field, we obtain the condition of the adiabaticity breakdown (Sergeev *et al.*, 1983)

$$K = G^{-1}[B_z^2/(\partial B_x/\partial z)] \approx 8\,, \tag{79}$$

where $G = mvc/q$ is the rigidity of the particles and the square bracketed factor depends solely on the magnetic field model assumed. Thus, having measured the pitch angle distributions within a sufficiently wide range of rigidities along the spacecraft orbit, one can probe the magnetotail structure over a considerable range of distances. Energetic

particles serve in this case as global tracers providing information which is supplementary to local magnetic measurements.

Figure 55 reproduced from the work by West *et al.* (1978) shows three configurations of the magnetic field in the near tail derived from a simple model, whose coefficients were fitted to the data obtained along the inbound orbit segments onboard the OGO-5 spacecraft on August 2, 4, and 25 in 1968. Simultaneous measurements of the electron

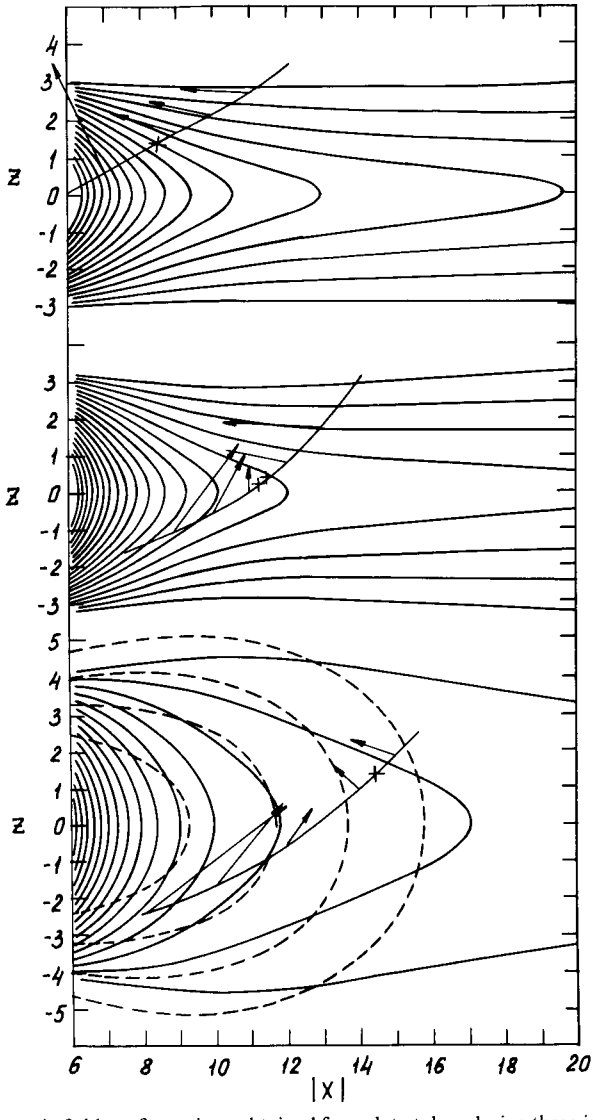

Fig. 55. Model magnetic field configurations obtained from data taken during three inbound passes of the OGO-5 spacecraft. All the three cases correspond to quiet conditions. Broken curves in the bottom panel display the Olson and Pfitzer (1974) model magnetic field lines. The crosses indicate the point of transition from isotropic to butterfly pitch-angle distributions of 79 keV electrons (West *et al.*, 1978b).

pitch angle distributions made from the same spacecraft indicated the position of the non-adiabatic scattering boundaries, which showed a close agreement with the results of trajectory computations made by using the model. An important feature noticed by West *et al.* (1978) is a surprising variability of the quiet nightside magnetosphere. All the three configurations in Figure 55 correspond to the K_p-index in the range between 0^+ and 1, however, a considerable difference in the degree of the field line stretching is obvious from the plots, which gives one more example of that the use of the K_p-index as the input model parameter is but a temporary and a palliative way out. It is also worth noting that even the most dipole-like configuration shown in the lower panel is significantly more stretched than it is predicted by the model of Olson and Pfitzer (1974) (broken lines) or by that of Mead and Fairfield (1975); this brings an additional evidence in favour of the results given by the T89 model (see Section 3.1).

Studies in this direction were developed in later works. Sergeev and Tsyganenko (1982), based on model calculations of the position of the non-adiabatic scattering boundaries of energetic particles in the near tail region, proposed a revised concept of the stable trapping boundaries. Indeed, in the light of the above results it should be admitted that the structure of the geomagnetic field defines not only the drift shell geometry including the boundaries between the open and the closed ones, but also the regions corresponding to a rapid loss of particles due to their non-adiabatic scattering in the ionospheric and drift loss cones. Therefore, the location of the boundary of the stable trapping region depends not only on the magnetic field configuration and the particle pitch angle, as is commonly assumed (Roederer, 1970), but also on the particle mass and energy.

A detailed study of the location of the isotropic precipitation boundary for 150 and 220 keV protons at ionospheric heights was done by Sergeev *et al.* (1983) using the data from the low-altitude polar orbiting spacecraft ESRO-1A corresponding to a prolonged quiet period. The magnetic field data taken by the geosynchronous satellite ATS-1 just near the non-adiabatic scattering region in the midnight sector were also available for the same period. That data in conjunction with the TU82 magnetic field model made it possible to compare the observed values Λ_i of the boundary latitude as well as those calculated from the model by means of (79) with the corresponding values of $B_z \approx H_{\mathrm{ATS}}$ in the scattering region. Figure 56 shows the results of this comparison. It is clearly seen that both groups of points reveal the same slope in dependence of Λ_i on H_{ATS}, but are separated by ≈ 20 nT along the horizontal axis. The most likely reason for this discrepancy is the above mentioned bias in the measured H-component (see Section 3.1). It is interesting to note that almost the same value $\Delta H = -22$ nT of the correction to be added to the measured H_{ATS} was obtained by Usmanov (1984) by means of minimizing the r.m.s. difference between the model fields inferred from the ATS-1 and the IMP-HEOS datasets.

The analysis by Sergeev *et al.* (1983) was based on particle data corresponding, in fact, to a single value of energy and considered the effect of changes in the magnetic field near $X_{\mathrm{GSM}} -6.6\ R_E$ only. Popielawska *et al.* (1985) employed the data by Imhof *et al.* (1977) on the measured latitudes Λ_i for a wide range of the particle rigidities G and

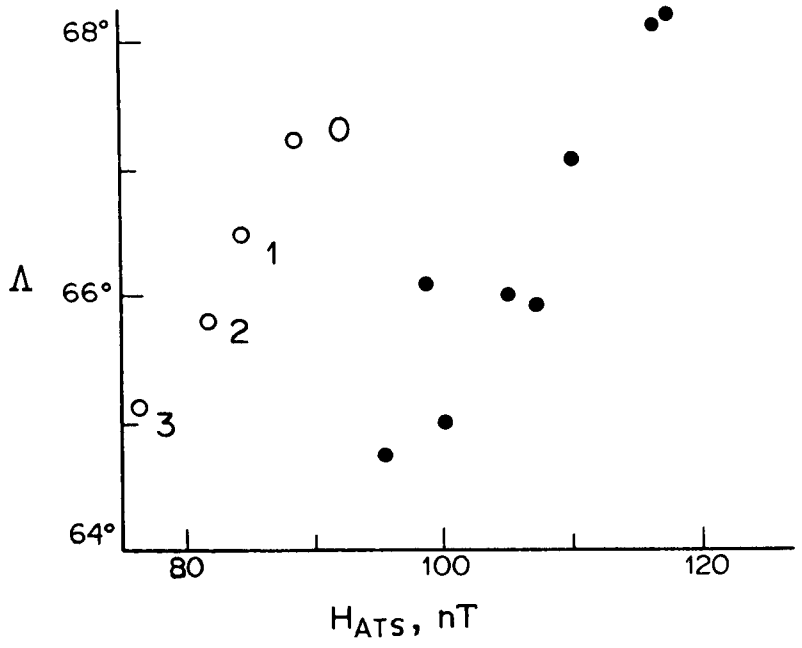

Fig. 56. Geomagnetic latitude of the isotropic precipitation boundary of 140 keV protons at ionospheric level as function of the total equatorial value of $B_z \approx H_{ATS}$ in the midnight sector of the geosynchronous orbit. The solid circles correspond to measurements onboard the ESRO-1A and the ATS-1 spacecraft, while the open circles labeled by the K_p values are obtained from calculations by using the criterion (79) in conjunction with the TU82 model (Sergeev *et al.*, 1983).

compared the observed dependence of their threshold values G_i on the L-parameter of the corresponding shells with those obtained in model calculations. It was found that within the range $4.5 \leq L \leq 6.0$ the model values of G_i fall off with L much more slowly than the measured ones. Therefore, if one assumes the view that the non-adiabatic scattering in the nightside current sheet is a dominant mechanism for the precipitation of energetic particles, then it should be admitted that the model requires a significant modification (but see Imhof, 1988). In particular, introducing a spatial variation of the sheet thickness can eliminate the disagreement. The model T89 described in Subsection 2.3.1 may serve as a good starting point for future works in this direction.

The above results confirm the fact of a high sensitivity of the pitch-angle and spatial distributions of energetic particle fluxes to the details of the magnetic field and electric current structure in the near magnetosphere. Sergeev and Malkov (1988) proposed on that basis a method for refining the model B_z distribution in the nightside equatorial plane, with a perspective to obtain a more reliable procedure of mapping the magnetic field lines. The method is based on using the relation (79) for the threshold rigidity combined with the equation

$$B_r^{(i)} R_E \, d\Lambda \, dy^{(i)} = B_z^{(e)} \, dx \, dy^{(e)}, \tag{80}$$

which indicates the constancy of the magnetic flux in the field line tube of a rectangular

cross-section with dimensions $R_E\,\mathrm{d}\Lambda$ by $\mathrm{d}y^{(i)}$ at ionospheric level and $\mathrm{d}x$ by $\mathrm{d}y^{(e)}$ in the equatorial plane. The relation (80) yields a differential equation for the equatorial distance $x = x(\Lambda)$ which contains implicitly the function $B_z(x)$ to be found. The second equation in the system is given by (79) where the rigidity dependence $G = G(\Lambda)$ is taken from spacecraft measurements and the functions $\partial B_x/\partial z$ and $\mathrm{d}y^{(i)}/\mathrm{d}y^{(e)}$ are specified by a field model. Having applied this method to the data of Imhof *et al.* (1977), Sergeev and Malkov (1988) were able to obtain several profiles of B_z versus X_{GSM}, of which three examples are given in Figure 57. In each of the profiles a local minimum of B_z is clearly visible at $X_{\mathrm{GSM}} \sim -5$–$6\,R_E$, the feature being absent in the initial TU82 model chosen for evaluating the functions $\mathrm{d}y^{(i)}/\mathrm{d}y^{(e)}$ and $\partial B_x/\partial z$.

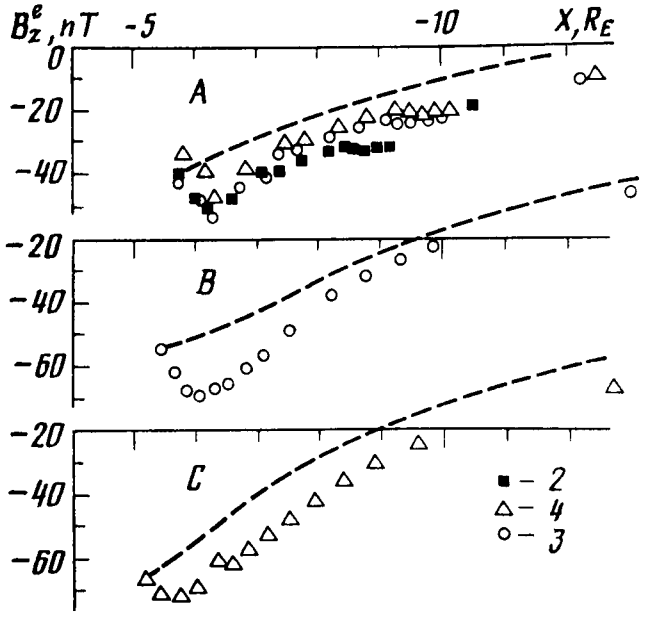

Fig. 57. Nightside equatorial profiles of the external B_z-component obtained from the data of Imhof *et al.* (1977) and TU82 magnetic field model by solving numerically Equations (79)–(80). The profiles correspond to three passes of the spacecraft, the dashed lines showing the initial model distributions. Squares, circles, and triangles represent the refined profiles corresponding to different K_p conditions (K_p = 2, 3, and 4, respectively (Sergeev and Malkov, 1988)).

5. Concluding Remarks

Significant advances have been made in development of magnetospheric magnetic field models in the last decades. Effective approaches to modeling the contributions from all the main magnetospheric current systems were proposed. In particular, powerful methods for simulating the observed structure of the nightside current sheet have been developed taking into account a spread-out nature of the latter, a spatial nonuniformity

of the current density distribution, and the tilt-related flexing effects. Using that model representations in conjunction with large amounts of spacecraft data provided refined and elaborate quantitative description of the average observed field configurations, in spite of serious problems caused by an extremely variable nature of the magnetosphere manifesting itself in 'noisy' datasets. Provided modeling expansions are sufficiently flexible, this approach allows to extract much information from the data including some comparatively fine effects related to the orientation of the interplanetary magnetic field.

On the other hand, a significant progress in understanding of the role of the magnetospheric plasma in the maintenance of the observed magnetic field structure has been achieved owing to recent theoretical works based on a magnetohydrostatic approach. Promising results were also obtained indicating great possibilities of using energetic particle measurements for a real-time diagnosis of the magnetospheric configurations and in refining the average field models.

In proceeding with the future perspectives, one of the most urgent practical problems is the development of algorithms being able to reconstruct instantaneous magnetospheric configurations on the basis of a synoptic ground-based and satellite control of the most important parameters of the 'dynamical' model. One of the first steps in this direction was described by Olson and Pfitzer (1982). Since the contributions from the main sources of the external field are relatively independent of each other, it is necessary to ensure a reliable separate determination of their intensities. Given a limited number of spacecraft, this imposes exacting demands to the choice of their orbit parameters. More specifically, it is clear that the best resolution of the separate source intensities could be expected if each of the spacecraft would be located within the region of a predominant influence of only one current system, so that the contributions from all others be relatively small. In this case the information matrix (see Appendix) is close to a diagonal one and the corresponding parameters are resolved with the best reliability. Thus, to obtain the maximum information on Birkeland current system, measurements taken by a polar orbiting low-altitude spacecraft should be included in the algorithm inputs, since the contribution from other currents is comparatively small in that region. Geosynchronous measurements at two or three points combined with the data from a spacecraft of the AMPTE/CCE type could give the main information on the ring current and the near-Earth tail current sheet. A more global monitoring of the integral tail current magnitude could be done from spacecraft with a highly elliptical orbits crossing the lobe region. Of principal importance is a continuous patrol of the solar wind state. The ground-based data could also provide a significant information. At last, as follows from the results reviewed in Section 4, low-altitude observations of energetic particles could also provide important supplementary data.

Acknowledgements

I thank my colleagues at Magnetospheric Physics Laboratory, Institute of Physics (Leningrad University), particularly Prof. M. I. Pudovkin and Dr V. A. Sergeev for their encouragement and helpful information. I owe special thanks to Dr A. V. Usmanov for

his many contributions to the magnetospheric modeling studies during those years of our collaboration and for his permission to include some material from his Thesis in the Appendix. I am also grateful to the scientists who contributed their reprints and preprints for this review.

Last, but not least, I cordially thank Ms M. V. Holeva and Ms L. L. Nemtseva for their invaluable help in preparing the manuscript and figures.

Appendix. Determination of Empirical Model Parameters from the Spacecraft Datasets*

A1. Initial Processing

Two of the four datasets used comprised the IMP and HEOS near-magnetosphere data and did not require much processing. Two other ones containing measurements in the tail region had to be reduced in order to exclude data taken outside the magnetosphere. After that the field of internal sources was subtracted from all the measured field vectors and the obtained external field components and the corresponding spatial coordinates were transformed to the solar magnetic system. Every average field vector was tagged by the corresponding values of the dipole tilt angle, the ground disturbance indices, and the solar wind parameters (King, 1977). All this information comprised the merged database whose elements will be termed hereinafter as data points.

A2. Formalization of the Experimental Information and Method for Computing the Model Parameters

Mathematical formulation of the method for constructing the quantitative magnetospheric models is based on a general statistical inverse problem approach whose applications to the geophysics were developed in the works by Goltzman (1971, 1981). Following this approach, let us represent the observed field vector $\mathbf{B}_K$ as

$$\mathbf{B}_K = \mathbf{f}_K(\boldsymbol{\rho}) + \mathbf{n}_K, \quad K = 1, \ldots, N, \tag{A1}$$

where K enumerates the dataset points from 1 to N, $\mathbf{f}_K$ is the modeling vector function which depends on the vector $\boldsymbol{\rho}$ of the model parameters, and $\mathbf{n}_K$ is the random residual vector.

The vectors $\mathbf{n}_K$ with $K = 1, \ldots, N$ can be considered as a random set with a corresponding sampling probability function $P(\mathbf{n}_1, \ldots, \mathbf{n}_N)$ which is assumed to be represented by the normal distribution with a dispersion

$$P(\mathbf{n}_1, \ldots, \mathbf{n}_N) = (2\pi\sigma^2)^{-3N/2} \prod_{K=1}^{N} \exp\left[-\frac{1}{2\sigma^2} \mathbf{n}_K^2 \right]. \tag{A2}$$

The next step is to construct the 'response function', i.e., the conditional probability distribution $P_{\mathbf{B}}(\boldsymbol{\rho})$ corresponding to a given experimental dataset $\{\mathbf{B}\}$. Using Bayes'

* This Appendix is based on materials of the thesis by Dr A. V. Usmanov (1984), with his kind permission.

formula (e.g., Korn and Korn, 1961)

$$P_{\mathbf{B}}(\boldsymbol{\rho}) = \frac{1}{P(\mathbf{B})} P(\boldsymbol{\rho}) P_{\boldsymbol{\rho}}(\mathbf{B}),$$

where $P(\boldsymbol{\rho})$ is the *a priori* probability of the random parameter vector $\boldsymbol{\rho}$, $P(\mathbf{B})$ is the absolute probability of the set $\{\mathbf{B}\}$ (in fact, $P(\mathbf{B}) \equiv 1$, since the set is already obtained), and $P_{\boldsymbol{\rho}}(\mathbf{B})$ is the conditional probability of $\{\mathbf{B}\}$ for a given $\boldsymbol{\rho}$. The latter function can be found from (A1) and the postulated normal law (A2) and, hence,

$$P_{\mathbf{B}}(\boldsymbol{\rho}) = (2\pi\sigma^2)^{-3N/2} \exp\left[-\frac{1}{2\sigma^2} \sum_{K=1}^{N} (\mathbf{B}_K - \mathbf{f}_K)^2 \right] P(\boldsymbol{\rho}). \tag{A3}$$

This function defines the statistical weight of possible values of the vector $\boldsymbol{\rho}$ to be found, for a given experimental set $\{\mathbf{B}\}$. According to the maximum likelihood criterion, the solution is given by the vector $\boldsymbol{\rho}^*$ which maximizes (A3), i.e., the most probable one. Under the assumptions (A2) and $P(\boldsymbol{\rho})$ = constant (no *a priori* information on $\boldsymbol{\rho}^*$ values), this criterion coincides with that of the least-squares method, in which a minimum of the function

$$\lambda(\boldsymbol{\rho}) = \sum_{K=1}^{N} [\mathbf{B}_K - \mathbf{f}_K(\boldsymbol{\rho})]^2 \tag{A4}$$

is to be found.

If all the components of $\boldsymbol{\rho}$ enter the model functions linearly (i.e., as coefficients), the task is solved by means of a standard least squares technique. In the more complex case with nonlinear parameters an iterative procedure is employed. The first step is to define the coefficients, while the nonlinear parameters are fixed at initial tentative values. After that the nonlinear parameters are re-evaluated with the coefficients being fixed at previously found values. This completes the first iteration and the whole sequence of calculations is repeated again, until the obtained decrease of λ becomes sufficiently small.

The corrections to the nonlinear parameters at each step are found by means of Newton–LeCam–Marquardt method whose essence consists in the following. Let us expand the function $\lambda(\boldsymbol{\rho})$ in Taylor series retaining three leading terms (Newton's method):

$$\lambda(\boldsymbol{\rho}) = \lambda(\boldsymbol{\rho}^{(i)}) + \sum_{s=1}^{S} \left.\frac{\partial\lambda}{\partial\rho_s}\right|_{\boldsymbol{\rho}=\boldsymbol{\rho}^{(i)}} \Delta\rho_s^{(i)} + \frac{1}{2} \sum_{s=1}^{S} \sum_{s'=1}^{S} \left.\frac{\partial^2\lambda}{\partial\rho_s\,\partial\rho_{s'}}\right|_{\boldsymbol{\rho}=\boldsymbol{\rho}^{(i)}} \Delta\rho_s^{(i)} \Delta\rho_{s'}^{(i)}, \tag{A5}$$

where $\Delta\rho_s^{(i)} = \rho_s - \rho_s^{(i)}$. To find the minimum of the function $\lambda(\boldsymbol{\rho})$ from (A5), we have to solve the system of linear equations

$$\frac{\partial\lambda(\boldsymbol{\rho})}{\partial\rho_s} = 0, \quad s = 1, \ldots, S,$$

which can be rewritten in the matrix form as

$$\hat{\mathbf{D}}^{-1}\Delta\boldsymbol{\rho}^{(i)} = \mathbf{d}\,, \tag{A6}$$

where

$$D_{ss'}^{-1} = -\left.\frac{\partial^2\lambda(\rho)}{\partial\rho_s\,\partial\rho_{s'}}\right|_{\boldsymbol{\rho}=\boldsymbol{\rho}^{(i)}}, \qquad d_s = \left.\frac{\partial\lambda(\boldsymbol{\rho})}{\partial\rho_s}\right|_{\boldsymbol{\rho}=\boldsymbol{\rho}^{(i)}}.$$

Solution of the system yields the corrections to be found. However, evaluating the second derivatives of the function $\lambda(\boldsymbol{\rho})$ is often too much cumbersome. LeCam (1960) proposed to replace the matrix $\hat{\mathbf{D}}^{-1}$ in (A6) by its statistical average over all random experimental samples. In accordance with (A2) and (A4), this leads to the average matrix $\hat{\mathbf{E}}^{-1}$ with elements

$$E_{ss'}^{-1} = \frac{1}{\sigma^2}\sum_{K=1}^{N}\frac{\partial\mathbf{f}_K}{\partial\rho_s}\cdot\left.\frac{\partial\mathbf{f}_K}{\partial\rho_{s'}}\right|_{\boldsymbol{\rho}=\boldsymbol{\rho}^{(i)}}. \tag{A7}$$

The right-hand side vector $\mathbf{d}$ in (A6) has the components

$$d_s = \frac{1}{\sigma^2}\sum_{K=1}^{N}\left[\frac{\partial\mathbf{f}_K}{\partial\rho_s}\,(\mathbf{B}_K - \mathbf{f}_K)\right]\Bigg|_{\boldsymbol{\rho}=\boldsymbol{\rho}^{(i)}}. \tag{A8}$$

Thus, we arrive at Newton–LeCam method which consists in solving the system $\hat{\mathbf{E}}^{-1}\Delta\boldsymbol{\rho}^{(i)} = \mathbf{d}$ instead of (A6).

To obtain more rapid convergence of the iteration process, we apply the following procedure suggested by Marquardt (1963). If the correction $\Delta\boldsymbol{\rho}$ obtained at ith iteration does not lead to further decrease of $\lambda(\boldsymbol{\rho}^{(i)})$, then the diagonal elements of the matrix $\hat{\mathbf{E}}^{-1}$ are increased by an appropriate quantity v. As a rule, the procedure significantly improves the convergence near the minimum point.

A3. Estimation of Errors of Model Parameter Values

Of key importance in this aspect is the information content in the experimental datasets, which defines the reliability and the accuracy of the obtained values of model parameters and depends on the distribution of data points in the space (x, y, z, ψ). Its quantitative measure is the dispersion of the parameter values. Another important quantity characterizing both the dataset and the model is the correlation between parameters. A high correlation means that variations of both parameters cause similar changes in the model field; in such a case it is difficult to effectively resolve the two parameters separately, i.e., their errors are relatively large.

Since the estimate $\boldsymbol{\rho}$ of the model parameters corresponding to a given data sample can also be considered as a random vector, it is possible to introduce its own probability distribution and then to apply the formalism of the maximum likelihood method, which implies in particular that the obtained estimates of the parameters are the optimal ones. The latter means that (i) in the limit of $N \to \infty$ they coincide with real values, (ii) their

distribution obeys the normal law, and (iii) they have minimal dispersions (Cramer, 1975). Therefore, the random vector $\boldsymbol{\rho}$ can be fully defined by its average value $\bar{\boldsymbol{\rho}}$ and the covariance matrix $\hat{\mathbf{K}}$. The corresponding inverse matrix $\hat{\mathbf{K}}^{-1}$ is called the information matrix (Pugachev, 1968) and has the elements

$$K_{ss'}^{-1} = -\overline{\frac{\partial^2 \ln P_{\mathbf{B}}(\boldsymbol{\rho})}{\partial \rho_s \, \partial \rho_{s'}}} ,$$

where the upper horizontal bar denotes averaging over various sample datasets $\{\mathbf{B}\}$. Using (A3),

$$K_{ss'}^{-1} = -\frac{1}{\sigma^2} \sum_{K=1}^{N} \frac{\partial \mathbf{f}_K}{\partial \rho_s} \frac{\partial \mathbf{f}_K}{\partial \rho_{s'}} . \tag{A9}$$

Comparing (A9) with (A7) shows that the information matrix is similar in its structure to $\hat{\mathbf{E}}^{-1}$. Notice, however, that the matrix $\hat{\mathbf{K}}^{-1}$ is of larger size than $\hat{\mathbf{E}}^{-1}$, since the latter is constructed of derivatives with respect to the nonlinear parameters only.

It can be seen from (A9) that the elements of $\hat{\mathbf{K}}$ and $\hat{\mathbf{K}}^{-1}$ matrices do not depend on values $\mathbf{B}_K$ of the measured magnetic field. Rather, they are defined by the number of data points and by their spatial distribution as well as by the 'noise' level σ^2. The diagonal elements of the information matrix K_{ss}^{-1} are the so-called Fisher's informants yielding a quantitative measure of the information contained in the dataset with respect to the sth model parameter ρ_s. The diagonal elements K_{ss} of the covariance matrix define the parameter dispersions sought, while the non-diagonal elements of the correlation matrix

$$k_{ss'} = \frac{K_{ss'}}{(K_{ss} K_{s's'})^{1/2}}$$

quantify the interrelations between the parameters.

References

Akasofu, S.-I.: 1981, *Space Sci. Rev.* **28**, 121.

Akasofu, S.-I. and Chapman, S.: 1961, *J. Geophys. Res.* **66**, 1321.

Akasofu, S.-I. and Chapman, S.: 1972, *Solar-Terrestrial Physics*, Clarendon Press, Oxford.

Alekseev, I. I. and Shabansky, V. P.: 1972, *Planetary Space Sci.* **20**, 117.

Alekseev, I. I., Kirillov, A. A., and Chuikova, T. A.: 1975, *Geomagnetizm i Aeronomiya* **15**, 508 (in Russian).

Alekseev, I. I.: 1978, *Geomagnetizm i Aeronomiya* **18**, 656 (in Russian).

Alfvén, H. and Fälthammar, C.-G.: 1963, *Cosmical Electrodynamics, Fundamental Principles*, 2nd ed., Clarendon Press, Oxford.

Allen, J. H., Abston, C. C., Papitashvili, V. O., Kharin, E. P., and Papitashvili, N. E.: 1982, *International Catalog of Geomagnetic Data*, Rept. UAG-86, NOAA, Boulder.

Antonova, A. E. and Shabansky, V. P.: 1968, *Geomagnetizm i Aeronomiya* **8**, 891.

Backus, G.: 1986, *Rev. Geophys.* **24**, 75.

Baker, D. N., Fritz, T. A., McPherron, R. L., Fairfield, D. H., Kamide, Y., and Baumjohann, W.: 1985, *J. Geophys. Res.* **90**, 1205.

Barish, F. D. and Roederer, J. G.: 1969, Preprint, University of Denver.
Barish, F. D. and Wiley, R. E.: 1970, *J. Geophys. Res.* **75**, 6342.
Barraclough, D. R.: 1987, *Phys. Earth Planet. Interiors* **48**, 279.
Barraclough, D. R., Harwood, G. M., Leaton, B. R., and Malin, S. R. C.: 1975, *Geophys. J. Roy. Astron. Soc.* **43**, 645.
Basu, S. and Rowlands, G.: 1986, *Planetary Space Sci.* **34**, 631.
Beard, D. B.: 1979, *J. Geophys. Res.* **84**, 2118.
Beard, D. B. and Jenkins, E. B.: 1962, *J. Geophys. Res.* **67**, 3361.
Beard, D. B., Hirschi, D., and Propp, K.: 1982, *J. Geophys. Res.* **87**, 2533.
Behannon, K. W.: 1968, *J. Geophys. Res.* **73**, 907.
Behannon, K. W.: 1970, *J. Geophys. Res.* **75**, 743.
Birn, J.: 1987, *J. Geophys. Res.* **92**, 11101.
Birn, J., Sommer, K., and Schindler, K.: 1977, *J. Geophys. Res.* **82**, 147.
Burch, J. L.: 1972, *J. Geophys. Res.* **77**, 6696.
Bythrow, P. F. and Potemra, T. A.: 1983, *Geophys. Res. Letters* **32**, 573.
Caan, M. N., McPherron, R. L., and Russell, C. T.: 1973, *J. Geophys. Res.* **78**, 8087.
Cahill, L. J.: 1966, *J. Geophys. Res.* **71**, 4505.
Cain, J. C., Hendricks, S. J., Langel, R. A., and Hudson, W. V.: 1967, *J. Geomagn. Geoelectr.* **19**, 335.
Chapman, S. and Ferraro, V. C. A.: 1931, *J. Geophys. Res.* **36**, 77.
Choe, J. Y. and Beard, D. B.: 1974, *Planetary Space Sci.* **22**, 609.
Choe, J. Y., Beard, D. B., and Sullivan, E. C.: 1973, *Planetary Space Sci.* **21**, 485.
Coleman, P. J. and McPherron, R. L.: 1976, in K. Knott and B. Battrick (eds.), *The Scientific Satellite Program during the International Magnetospheric Study*, D. Reidel Publ. Co., Dordrecht, Holland, pp. 345–365.
Cowley, S. W. H.: 1973, *Radio Sci.* **8**, 903.
Cowley, S. W. H.: 1981, *Planetary Space Sci.* **29**, 79.
Cramer, H.: 1957, *Mathematical Methods of Statistics*, Princeton Univ. Press, Princeton.
Crooker, N. U. and Siscoe, G. L.: 1981, *J. Geophys. Res.* **86**, 11201.
Crooker, N. U., Berchem, J., and Russell, C. T.: 1987, *J. Geophys. Res.* **92**, 13467.
Dandouras, J.: 1988, *J. Geophys. Res.* **93**, 7345.
Erickson, G. M.: 1984, in E. W. Hones (ed.), *Magnetic Reconnection*, Geophys. Monograph Ser., Vol. 30, AGU, Washington, D.C., pp. 296–302.
Erickson, G. M. and Wolf, R. A.: 1980, *Geophys. Res. Letters* **7**, 897.
Fairfield, D. H.: 1971, *J. Geophys. Res.* **76**, 6700.
Fairfield, D. H. and Mead, G. D.: 1975, *J. Geophys. Res.* **80**, 535.
Fairfield, D. H.: 1980, *J. Geophys. Res.* **85**, 775.
Fairfield, D. H.: 1986, *J. Geophys. Res.* **91**, 4238.
Fairfield, D. H., Acuña, M. H., Zanetti, L. J., and Potemra, T. A.: 1987, *J. Geophys. Res.* **92**, 7432.
Frank, L. A.: 1967, *J. Geophys. Res.* **72**, 3753.
Fuchs, K. and Voigt, G.-H.: 1979, in W. P. Olson (ed.), *Quantitative Modeling of Magnetospheric Processes*, Geophys. Monograph Ser., Vol. 21, AGU, Washington, D.C., pp. 86–95.
Gauss, C. F.: 1839, *Allgemeine Theorie des Erdmagnetismus. Resultate, 1839*, Werke, V.B., pp. 119–175, Nachtrag, pp. 175–180.
Goltzman, F. M.: 1971, *Statistical Interpretation Models*, Nauka, Moscow (in Russian).
Goltzman, F. M.: 1982, *Physical Experiment and Statistical Inferences*, Leningrad Univ. Press, Leningrad (in Russian).
Gosling, J. T., McComas, D. J., Thomsen, M. F., Bame, S. J., and Russell, C. T.: 1986, *J. Geophys. Res.* **91**, 7093.
Gray, P. C. and Lee, L. C.: 1982, *J. Geophys. Res.* **87**, 7445.
Gustafsson, G.: 1970, Arkiv *Geofysik* **5**, 595.
Hakura, Y.: 1965, *Rep. Ionosphere Space Res. Japan* **19**, 121.
Halderson, D. W., Beard, D. B., and Choe, J. Y.: 1975, *Planetary Space Sci.* **23**, 887.
Harel, M., Wolf, R. A., Spiro, R. W., Reiff, P. H., and Chen, C.-K.: 1981, *J. Geophys. Res.* **86**, 2242.
Hedgecock, P. C. and Thomas, B. T.: 1975, *Geophys. J. Roy. Astron. Soc.* **41**, 391.
Hedgecock, P. C. and Thomas, B. T.: 1979, Imperial College preprint, London.
Heelis, R. A. and Hanson, W. B.: 1980, *J. Geophys. Res.* **85**, 1995.

Hilmer, R. V. and Voigt, G.-H.: 1987, *J. Geophys. Res.* **92**, 8660.
Hoffman, R. A. and Bracken, P. A.: 1965, *J. Geophys. Res.* **70**, 3541.
Hoffman, R. A. and Bracken, P. A.: 1967, *J. Geophys. Res.* **72**, 6039.
Hoffman, R. A. and Cahill, L. J.: 1968, *J. Geophys. Res.* **73**, 6711.
Iijima, T. and Potemra, T. A.: 1976, *J. Geophys. Res.* **81**, 2165.
Iijima, T. and Potemra, T. A., and Zanetti, L. J.: 1989, *J. Geophys. Res.* (in press).
Imhof, W. L.: 1988, *J. Geophys. Res.* **93**, 9743.
Imhof, W. L., Reagan, J. B., and Gaines, E. E.: 1977, *J. Geophys. Res.* **82**, 5215.
Isaev, S. I. and Pudovkin, M. I.: 1972, *Polar Aurora and Processes in the Earth's Magnetosphere*, Nauka Leningrad (in Russian).
Izhovkina, N. I.: 1979, Geomagnetizm i Aeronomiya **19**, 1125 (in Russian).
Kamide, Y. and Fukushima, N.: 1971, *Rept. Ionosphere Space Res. Japan* **25**, 125.
Kaufmann, R. L.: 1987, *J. Geophys. Res.* **92**, 7471.
Kendall, P. C., Chapman, S., Akasofu, S.-I., and Swartztrauber, P. N.: 1966, *Geophys. J. Roy. Astron. Soc.* **11**, 349.
King, J. H.: 1977, *Interplanetary Medium Data Book*, NSSDS, Greenbelt.
Kivelson, M. G. and Spence, H. E.: 1989, *Geophys. Res. Letters* (in press).
Korn, G. A. and Korn, T. M.: 1961, *Mathematical Handbook for Scientists and Engineers*, Ch. 6, McGraw-Hill Book Co. Inc., New York.
Kosik, J.-C.: 1978, *Space Sci. Rev.* **22**, 481.
Kosik, J.-C.: 1984, *Planetary Space Sci.* **32**, 965.
Kropotkin, A. P.: 1977, *Geomagnetizm i Aeronomiya* **17**, 259 (in Russian).
Langel, R. A.: 1974, Goddard Space Flight Center Report, X-645–73–225.
Langel, R. A. and Sweeney, R. E.: 1971, *J. Geophys. Res.* **76**, 4420.
Lin, R. P. and Barfield, J. N.: 1984, *Planetary Space Sci.* **32**, 1283.
Lui, A. T. Y.: 1983, in *Magnetospheric Currents*, Geophys. Monograph, Vol. 28, AGU, Washington, D.C., pp. 158–170.
Lui, A. T. Y., McEntire, R. W., and Krimigis, S. M.: 1987, *J. Geophys. Res.* **92**, 7459.
Lyons, L. R. and Williams, D. J.: 1984, in *Quantitative Aspects of Magnetospheric Physics*, D. Reidel Publ. Co., Dordrecht, Holland.
Marquardt, D. W.: 1963, *J. Soc. Ind. Appl. Math.* **11**, 431.
McComas, D. J., Russell, C. T., Elphic, R. C., and Bame, S. J.: 1986, *J. Geophys. Res.* **91**, 4287.
McIlwain, C. E.: 1974, in B. M. McCormac (ed.), *Magnetospheric Physics*, D. Reidel Publ. Co., Dordrecht, Holland, p. 143.
Mead, G. D.: 1964, *J. Geophys. Res.* **69**, 1181.
Mead, G. D. and Beard, D. B.: 1964, *J. Geophys. Res.* **69**, 1169.
Mead, G. D. and Fairfield, D. H.: 1975, *J. Geophys. Res.* **80**, 523.
Meng, C.-I.: 1982, *Geophys. Res. Letters* **9**, 60.
Midgley, J. E.: 1964, *J. Geophys. Res.* **69**, 1197.
Midgley, J. E. and Davis, L., Jr.: 1962, *J. Geophys. Res.* **67**, 499.
Midgley, J. E. and Davis, L., Jr.: 1963, *J. Geophys. Res.* **68**, 5111
Mihalov, J. D., Colburn, D. S., Currie, R. G., and Sonett, C. P.: 1968, *J. Geophys. Res.* **73**, 943.
Morfill, G.: 1975, *Space Sci. Rev.* **17**, 391.
Morfill, G. and Scholer, M.: 1973, *Space Sci. Rev.* **15**, 267.
Nagai, T.: 1987, *J. Geophys. Res.* **92**, 11215.
Newell, P. T. and Meng, C.-I.: 1989, *J. Geophys. Res.* **94**, 6949.
Ogino, T., Walker, R. J., Ashour-Abdalla, M., and Dawson, M.: 1986, *J. Geophys. Res.* **91**, 10029.
Ohtani, S., Kokubun, S., Elphic, R. C., and C. T. Russell: 1988, *J. Geophys. Res.* **93**, 9709.
Olson, W. P.: 1969, *J. Geophys. Res.* **74**, 5642.
Olson, W. P. and Pfitzer, K. A.: 1974, *J. Geophys. Res.* **79**, 3739.
Olson, W. P. and Pfitzer, K. A.: 1977, McDonnell Douglas Astronautics Co. preprint.
Olson, W. P. and Pfitzer, K. A.: 1982, *J. Geophys. Res.* **87**, 5943.
Ono, T.: 1987, *Mem. Nat. Inst. Polar Res. Japan, Spec. Issue* **48**, 46.
Parker, E. N.: 1957, *Phys. Rev.* **107**, 924.
Peddie, N. W.: 1982, *J. Geomagn. Geoelectr.* **34**, 309.

Pellinen, R. J. and Heikkila, W. J.: 1984, *Space Sci. Rev.* **37**, 1.
Pilipp, W. G. and Morfill, G.: 1978, *J. Geophys. Res.* **83**, 5670.
Popielawska, B., Szalinska-Piechota, E., and Tsyganenko, N. A.: 1985, *Planetary Space Sci.* **33**, 1433.
Pudovkin, M. I. and Semenov, V. S.: 1985, *Space Sci. Rev.* **41**, 1.
Pudovkin, M. I., Barsukov, V. M., and Tsyganenko, N. A.: 1971, Physical Institute, Leningrad University preprint.
Pudovkin, M. I., Tsyganenko, N. A., and Usmanov, A. V.: 1986, *Geomagnetizm i Aeronomiya* **26**, 946 (in Russian).
Pugachev, V. S.: 1962, *Theory of Random Functions and Its Applications to Problems of Automatic Operation*, Nauka, Moscow (in Russian).
Roederer, J. G.: 1969, *Rev. Geophys.* **1**, 77.
Roederer, J. G.: 1970, *Dynamics of Geomagnetically Trapped Radiation*, Springer-Verlag, Heidelberg.
Roederer, J. G.: 1977, *Space Sci. Rev.* **21**, 23.
Roelof, E. C.: 1987, *Geophys. Res. Letters* **14**, 652.
Rostoker, G., Savoie, D., and Phan, T. D.: 1988, *J. Geophys. Res.* **93**, 8633.
Russell, C. T. and Brody, K. I.: 1967, *J. Geophys. Res.* **72**, 6104.
Sato, T. and Iijima, T.: 1979, *Space Sci. Rev.* **24**, 347.
Schield, M. A.: 1969, *J. Geophys. Res.* **74**, 1275.
Schindler, K.: 1974, *Space Sci. Rev.* **17**, 589.
Schindler, K.: 1979, *Space Sci. Rev.* **23**, 365.
Schindler, K. and Birn, J.: 1986, *Space Sci. Rev.* **44**, 307.
Scholer, M.: 1975, *Space Sci. Rev.* **17**, 3.
Schulz, M.: 1980, *J. Geomag. Geoelectr.* **32**, 507.
Schulz, M. and McNab, M. C.: 1987, *Geophys. Res. Letters* **14**, 182.
Sckopke, N.: 1972, *Cosmic Electrodyn.* **3**, 330.
Sergeev, V. A.: 1987, *Geomagnetizm i Aeronomiya* **27**, 612 (in Russian).
Sergeev, V. A. and Malkov, M. V.: 1988, *Geomagnetizm i Aeronomiya* **28**, 649 (in Russian).
Sergeev, V. A. and Lennartsson, W.: 1988, *Planetary Space Sci.* **36**, 353.
Sergeev, V. A. and Tsyganenko, N. A.: 1980, *The Earth's Magnetosphere*, Nauka, Moscow (in Russian).
Sergeev, V. A. and Tsyganenko, N. A.: 1982, *Planetary Space Sci.* **30**, 999.
Sergeev, V. A., Sazhina, E. M., Tsyganenko, N. A., Lundblad, J. Å., and Søraas, F.: 1983, *Planetary Space Sci.* **31**, 1147.
Sibeck, D. G., Siscoe, G. L., Slavin, J. A., Smith, E. J., Tsurutani, B. T., and Lepping, R. P.: 1985, *J. Geophys. Res.* **90**, 4011.
Sibeck, D. G., McEntire, R. W., Lui, A. T. Y., Lopez, R. E., and Krimigis, S. M.: 1987, *J. Geophys. Res.* **92**, 13485.
Siscoe, G. L.: 1966, *Planetary Space Sci.* **14**, 947.
Sozou, C. and Windle, D. W.: 1969a, *Planetary Space Sci.* **17**, 375.
Sozou, C. and Windle, D. W.: 1969b, *Planetary Space Sci.* **17**, 999.
Sozou, C. and Windle, D. W.: 1970, *Planetary Space Sci.* **18**, 699.
Speiser, T. W. and Ness, N. F.: 1967, *J. Geophys. Res.* **72**, 131.
Spence, H. E., Kivelson, M. G., and Walker, R. J.: 1987, *Geophys. Res. Letters* **14**, 872.
Stern, D. P.: 1976, *Rev. Geophys. Space Phys.* **14**, 199.
Stern, D. P.: 1983, *Rev. Geophys. Space Phys.* **21**, 125.
Stern, D. P.: 1985, *J. Geophys. Res.* **90**, 10851.
Stern, D. P.: 1987a, *J. Geophys. Res.* **92**, 4437.
Stern, D. P.: 1987b, *Rev. Geophys.* **25**, 523.
Stern, D. P. and Alexeev, I. I.: 1988, *Rev. Geophys.* **26**, 782.
Stiles, G. S., Hones, E. W., Jr., Bame, S. J., and Asbridge, J. R.: 1978, *J. Geophys. Res.* **83**, 3166.
Sugiura, M.: 1972, *J. Geophys. Res.* **77**, 6093.
Sugiura, M. and Poros, D. J.: 1973, *Planetary Space Sci.* **21**, 1763.
Taylor, H. E. and Hastie, R. J.: 1971, *Cosmic Electrodyn.* **2**, 211.
Taylor, H. E. and Hones, E. W.: 1965, *J. Geophys. Res.* **70**, 3605.
Troschichev, O. A.: 1982, *Space Sci. Rev.* **32**, 275.
Tsyganenko, N. A.: 1975a, *Kosm. Issled.* **13**, 215 (in Russian).

Tsyganenko, N. A.: 1975b, *Geomagnetizm i Aeronomiya* **15**, 487 (in Russian).
Tsyganenko, N. A.: 1976, *Ann. Geophys.* **32**, 1.
Tsyganenko, N. A.: 1979, *Subroutines and Tables for the Geomagnetic Field Computations*, WDC-B2, Moscow.
Tsyganenko, N. A.: 1981, *Ann. Geophys.* **37**, 381.
Tsyganenko, N. A.: 1982a, *Planetary Space Sci.* **30**, 1007.
Tsyganenko, N. A.: 1982b, *Planetary Space Sci.* **30**, 433.
Tsyganenko, N. A.: 1987a, *Planetary Space Sci.* **35**, 1347.
Tsyganenko, N. A.: 1987b, *Geomagnetizm i Aeronomiya* **27**, 987 (in Russian).
Tsyganenko, N. A.: 1988, *Geomagnetizm i Aeronomiya* **28**, 389 (in Russian).
Tsyganenko, N. A.: 1989a, *Planetary Space Sci.* **37**, 5.
Tsyganenko, N. A.: 1989b, *Planetary Space Sci.* **37**, 183.
Tsyganenko, N. A.: 1989c, *Planetary Space Sci.* **37**, 1037.
Tsyganenko, N. A. and Usmanov, A. V.: 1982, *Planetary Space Sci.* **30**, 985.
Tsyganenko, N. A. and Usmanov, A. V.: 1984, *Planetary Space Sci.* **32**, 97.
Tsyganenko, N. A., Usmanov, A. V., Papitashvili, V. O., Papitashvili, N. E., and Popov, V. A.: 1987, in V. A. Nechitailenko (ed.), *Software for Computations of the Geomagnetic Field and Related Coordinate Systems*, Soviet Geophysical Committee, Acad. of Sci. USSR, Moscow.
Usmanov, A. V.: 1984, 'Quantitative Modeling of the Magnetosphere Based on Spacecraft Data', Cand. Sci. Dissertation, Leningrad State University.
Usmanov, A. V. and Tsyganenko, N. A.: 1984, *Geomagnetizm i Aeronomiya* **24**, 968 (in Russian).
Voigt, G.-H.: 1972, *Z. Geophys.* **38**, 319.
Voigt, G.-H.: 1981, *Planetary Space Sci.* **29**, 1.
Voigt, G.-H.: 1984, *J. Geophys. Res.* **89**, 2169.
Voigt, G.-H.: 1986, in Y. Kamide and J. A. Slavin (eds.), *Solar Wind – Magnetosphere Coupling*, Terra Scientific Publ. Co., Tokyo, pp. 233–273.
Voigt, G.-H. and Hilmer, R. V.: 1987, in A. T. Y. Lui (ed.), *Magnetotail Physics*, The Johns Hopkins University Press, Baltimore, pp. 91–97.
Voigt, G.-H. and Wolf, R. A.: 1985, *J. Geophys. Res.* **90**, 4046.
Wagner, J. S., Kan, J. R., and Akasofu, S.-I.: 1979, *J. Geophys. Res.* **84**, 891.
Walker, R. J.: 1976, *Rev. Geophys. Space Phys.* **14**, 411.
Walker, R. J.: 1979, in W. P. Olson (ed.), *Quantitative Modeling of Magnetospheric Processes*, Geophys. Monogr. Ser., Vol. 21, AGU, Washington, D.C., pp. 9–34.
Walker, R. J.: 1983, *Rev. Geophys.* **21**, 495.
Walker, R. J. and Southwood, D. J.: 1982, *J. Geophys. Res.* **87**, 7460.
West, H. I., Buck, R. M., and Kivelson, M. G.: 1978a, *J. Geophys. Res.* **83**, 3805.
West, H. I., Buck, R. M., and Kivelson, M. G.: 1978b, *J. Geophys. Res.* **83**, 3819.
Williams, D. J.: 1987, *Rev. Geophys.* **25**, 570.
Williams, D. J. and Mead, G. D.: 1965, *J. Geophys. Res.* **70**, 3017.
Willis, D. M. and Pratt, R. J.: 1972, *J. Atmospheric Terrest. Phys.* **34**, 1955.
Wright, A. N.: 1985, *Planetary Space Sci.* **33**, 847.
Yamamoto, T. and Tamao, T.: 1978, *Planetary Space Sci.* **26**, 1185.
Zaitseva, S. A. and Pudovkin, M. I.: 1976, *Planetary Space Sci.* **24**, 518.
Zanetti, L. J., Baumjohann, W., and Potemra, T. A.: 1983, *J. Geophys. Res.* **88**, 4875.
Zmuda, A. J. and Armstrong, J. C.: 1974, *J. Geophys. Res.* **79**, 4611.
Zmuda, A. J., Martin, J. H., and Heuring, F. T.: 1966, *J. Geophys. Res.* **71**, 5033.